Developments of scanning gel electrochemical microscopy

Ning Dang

To cite this version:

Ning Dang. Developments of scanning gel electrochemical microscopy. Analytical chemistry. Université de Lorraine, 2020. English. NNT : 2020LORR0243 . tel-03272273

HAL Id: tel-03272273

https://hal.univ-lorraine.fr/tel-03272273

Submitted on 28 Jun 2021

Sujet de thèse

Développements de la
Microscopie Electrochimique à Balayage à Sonde à Gel

Par

Ning DANG

Pour l'obtention de titre de **Docteur en Chimie**

L'École Doctoral: Chimie - Mécanique - Matériaux - Physique (C2MP)

Rapporteurs :

Prof. Maria de Fátima Grilo da Costa Montemor – Professeur (Technical University of Lisbon, Lisbon, Portugal)

Dr. Frédéric Kanoufi – Directeur de Recherche (ITODYS, Université Paris Diderot, Paris, France)

Examinateurs :

Prof. Kristina Tschulik – Professeur (Ruhr University Bochum, Bochum, Germany)
Prof. Alain Durand – Professeur (LCPM, Nancy, France)

Directeurs :

Dr. Alain Walcarius – Directeur de Recherche (LCPME, Villers-lès-Nancy, France)

Dr. Liang Liu – Chargé de Recherche (LCPME, Villers-lès-Nancy, France)

Laboratoire de Chimie Physique et Microbiologie pour les Matériaux et l'Environnement (LCPME)
UMR 7564, CNRS / Université de Lorraine
405 Rue de Vandoeuvre, 54600, Villers-lès-Nancy, France

Title of Thesis

Developments of Scanning Gel Electrochemical Microscopy

By

Ning DANG

For obtaining the title of **Doctor of Chemistry**

Doctoral School : Chimie - Mécanique - Matériaux- Physique (C2MP)

Reviewers:

Prof. Maria de Fátima Grilo da Costa Montemor – Professor (Technical University of Lisbon, Lisbon, Portugal)

Dr. Frédéric Kanoufi – Research Director (ITODYS, Université Paris Diderot, Paris, France)

Examiners:

Prof. Kristina Tschulik – Professor (Ruhr University Bochum, Bochum, Germany)

Prof. Alain Durand – Professor (LCPM, Nancy, France)

Supervisors:

Dr. Alain Walcarius – Research Director (LCPME, Villers-lès-Nancy, France)

Dr. Liang Liu – Research Associate (LCPME, Villers-lès-Nancy, France)

Laboratoire de Chimie Physique et Microbiologie pour les Matériaux et l'Environnement (LCPME)
UMR 7564, CNRS / Université de Lorraine
405 Rue de Vandoeuvre, 54600, Villers-lès-Nancy, France

Acknowledgements

Foremost, I would like to express my sincere gratitude to my supervisors. **Alain Walcarius,** since the first discussion with you about my experiments, my impression on you expands from a humor, charming director to a detail-oriented, patient and extremely knowledgeable researcher. Each time, the chemical structures and reaction mechanisms you draw on the paper really helped and inspired me a lot. What I admire most is that you always bring papers back home for reading even you are just off from full-day work. **Liang Liu**, I feel so lucky for being your student. I deeply thank you for helping me overcome all the difficulties of living in a foreign country. I call you "my godfather", because you teach me so many basic but significant scientific skills, like experiments design, paper writing, and work presentation, *etc*. All these things are extremely meaningful for my early academic career. During these three years, stupid mistakes I made are countless. But you always encourage me and push me back to the correct direction. The science appreciation you show to me, as well the international conferences you supported for me really help me open my eyes and built my scientific feeling. Of course, I should also thanks for all your criticism, which might be direct but indeed make me stronger and more capable.

Secondly, I would like to acknowledge **Mathieu Etienne**. You are a lovely researcher and full of interesting ideas. It is always a pleasure talking with you. Thanks a lot for helping me optimize the parameters of shear-force and fabricate the integrated probe. More importantly, thank you for reminding me to think about a critical question, "What do I like?" Besides, I must thank my thesis committees, **Rachel Yerushalmi** and **Grégory Francius**. You gave me so much insightful advice about experiments and kind encouragement to my research life. In addition, I would like to express my gratitude to all the nice and friendly permanent members in our group. **Grégoire Herzog, Christelle Despas, Neus Vilà, Marc Hebrant, and Michel Perdicakis**, thank you so much for the discussion and helpful ideas about my works and all help for my doctoral life. Thanks to **Claire Genois** for purchasing and looking for the chemical compounds**,** **Jean-Paul Moulin** and **Gérard Paquot** for the holders and electrochemical cells fabrication. Thanks to **Marie Tercier, Christelle Charbaut** and **Jacqueline Druon** for their help with administration issues.

Furthermore, I would like to appreciate my labmates. **Mariela Brites Helú**, thank you for being my neighbor in our office room. Staying with you is so comfortable. I must also say thanks to you for all your help on my experiments, etching probe fabrication, 3-D printing, instrumentation, and so on. **Vincent Feynerol**, for helping my French. **Jianren Wang** and **Guofeng Lu,** for every lunch we had together in Resto'U, and all the encouragements and comforts you gave in my difficult time. **Qiao Liu**, for all girl's topics and experimental results sharing. **Wahid Ullah**, for sharing the experience of raising a baby, **Taisiia Sikolenko**, **Himanshu Maheshwari, Deomila Basmin, Joanna Rogińska**, **Magdalena Kaliszczak**, for sharing your culture and all the interesting things, that really fill my life in lab with much happiness.

And finally, I would like to express my gratitude to my family. My grandmother and my parents, thanks for giving me endless love and long-term support. You inspire me to complete my thesis and move forward. My younger brother, it's my luck to have you as my brother. Thank you for always standing with me and sharing my happiness and sadness. My parents in law, I am so grateful for your caring and understanding. You always remind me to relax and pay much attention to my health. My husband, you are my sunshine. When I want to fly, you help me fix my wings. When I feel exhausted, you built a nest and welcome me back. Thanks for being there for 11 years no matter we have laugher or tears.

And of course, last but not least, I am grateful to the Chinese Scholarship Council for my PhD funding.

Table of Contents

Abstract

In the past 30 years, scanning electrochemical probe microscopy (SEPM) techniques have been developed as powerful tools for studying electrochemistry at micro/nano scale. The most developed and commercialized techniques are Scanning Electrochemical Microscopy (SECM) and Scanning Ion Conductance Microscopy (SICM). However, the entire sample is immersed in the electrolyte solution during the measurements, which may yield uncontrolled change of the surface due to the long scanning time. Instead of localizing electrode, the electrolyte can also be localized, which is known as Scanning Droplet Cell (SDC) or Scanning Electrochemical Cell Microscopy (SECCM). The experiments are carried out under ambient conditions. However, the spreading of droplet over sample surface may be affected by the hydrophilicity and roughness of sample, which brings challenges in quantitative analysis.

Recently, Scanning Gel Electrochemical Microscopy (SGECM) was reported by our group as a novel SEPM technique. It is mainly based on a gel probe that immobilizes the electrolyte on a micro-disk electrode. Thus, the analysis can be achieved in ambient environment with controllable electrolyte spreading. This thesis is devoted to the further developments of SGECM. Foremost, the background of developments of SGECM is introduced in Chapter I. Different SEPM techniques, gel polymer electrolytes, achievements of SGECM are systematically presented, respectively. In Chapter II, the lateral physical resolution of SGECM is thoroughly and quantitatively studied by both marking single pixels and scanning over periodic samples. In chapter III, the potentiometric mode of SGECM is developed based on a novel Ag/AgCl-gel micro-reference electrode. As the gel probe undergoes thousands of pressing-stretching cycles in a mapping measurement, it is highly important to improve its mechanical strength. Chapter IV describes the preliminary effort of chemically cross-linking chitosan gel by glutaraldehyde. Chapter V further pushes forward the development of integrated gel probes with both working and reference electrode.

Key words: Scanning Gel Electrochemical Microscopy (SGECM), local electrochemical analysis, hydrogel.

Résumé

Au cours des 30 dernières années, les techniques de microscopie à sonde électrochimique à balayage (SEPM) ont été développée comme outils puissants pour des études électrochimiques à l'échelle micro/nano. Les techniques les plus développées et commercialisées sont la microscopie électrochimique à balayage (SECM) et la microscopie de conductance ionique à balayage (SICM). Cependant, les mesures impliquent l'immersion totale de l'échantillon au sein de la solution d'électrolyte, qui peut produire des modifications incontrôlées de la surface en raison du long temps de balayage. A défaut de localiser l'électrode elle-même, l'électrolyte peut également être localisé, ce qui est connu sous le nom de microscopie de cellules à balayage de gouttelettes (SDC) ou de microscopie à balayage de cellule électrochimique (SECCM). Ceci permet de réaliser les expériences dans des conditions ambiantes. Toutefois, l'étalement des gouttelettes sur la surface de l'échantillon peut être affecté par l'hydrophilie et la rugosité de l'échantillon, ce qui pose des problèmes pour l'analyse quantitative. Récemment, la microscopie électrochimique à balayage à sonde à gel (SGECM) a été proposée comme nouvelle technique de SEPM. Elle est principalement basée sur une sonde à gel qui immobilise l'électrolyte sur une électrode de type micro-disque. Par conséquent, l'analyse peut être réalisée dans un environnement ambiant avec un étalement d'électrolyte contrôlable. Cette thèse est consacrée aux développements ultérieurs de la SGECM. Avant tout, le contexte des développements de SGECM est présenté dans le chapitre I. Différentes techniques SEPM, électrolytes polymères gel, réalisations de SGECM sont systématiquement présentées, respectivement. Au chapitre II, la résolution physique latérale de la SGECM est étudiée de manière approfondie et quantitativement en marquant des pixels uniques et en balayant périodiquement les échantillons. Dans le chapitre III, le mode potentiométrique de la SGECM est développé à partir d'une nouvelle électrode de micro-référence Ag/AgCl-gel. Comme la sonde à gel subit des milliers de cycles d'étirement et de compression au cours d'une mesure de cartographie, il est très important d’améliorer sa résistance mécanique. Le chapitre IV décrit une approche préliminaire basée sur la réticulation chimique du gel de chitosane par le glutaraldéhyde. Le chapitre V pousse plus loin le développement des sondes à gel ainsi que l’intégration des électrodes de travail et de référence.

Mots-clés: microscopie électrochimique à balayage à sonde à gel (SGECM), analyse électrochimique locale, hydrogel.

Résumé long de la thèse en français

Au cours des 30 dernières années, les techniques de microscopie à sonde électrochimique à balayage (SEPM) ont été développées comme de puissants outils pour l'analyse électrochimique localisée. SEPM utilise des sondes micro- ou nano-métriques à base d'électrode ou d'électrolyte pour mesurer des signaux électrochimiques localisés spatialement. En comparaison des techniques conventionnelles de microscopie, l'avantage majeur du SEPM est que diverses sondes microscopiques peuvent être mises en œuvre pour détecter *in situ* à la fois la topographie et la réactivité électrochimique des surfaces dans des conditions humides (en solution) ou même à l'air ambiant. Plus récemment, SEPM a permis de relever de nombreux défis d'applications dans différents domaines tels que l'électrocatalyse, la conversion d'énergie, la corrosion, la bioélectrochimie, ou encore l'exploitation des protéines redox dans les biofilms, entre autres.

Les techniques les plus développées et commercialisées de SEPM sont la microscopie électrochimique à balayage (SECM) et la microscopie de conductance ionique à balayage (SICM). La SECM est basée sur une microélectrode à disque, qui est balayée sur la surface de l'échantillon à analyser tout en enregistrant en continu la réponse de la sonde. La microélectrode est approchée du substrat de manière contrôlée, soit en suivant le courant de pointe correspondant aux réactions de transfert de charge de médiateurs électroactifs intentionnellement ajoutés dans la solution (que l'on appellera rétroaction actuelle), soit par un contrôle des forces de cisaillement. De par sa souplesse de fonctionnement, la SECM est a pu être commercialisée et est maintenant largement utilisée dans différents domaines. Conceptuellement différente de la SECM, la SICM est basée sur une pointe de type micropipette dont l'ouverture sert de voie aux ions. La valeur de la conductance ionique est enregistrée en appliquant un potentiel entre deux électrodes de référence dont l'une se situe au sein de la pipette et l'autre est placée dans la solution externe. En SICM, la distance « pointe – échantillon » peut être contrôlée avec précision en raison de l'alternance de la résistance du système. Ce signal électrophysiologique aide à séparer les signaux topographique et électrochimique dans les tests de cartographie. Avec le grand avantage de moins stimuler/modifier les surfaces analysées, la SICM offre de nombreux attraits pour des applications impliquant des substances fragiles, par exemple, comme c'est souvent le cas en analyse biologique. Même si SECM et SICM sont de puissants outils pour cartographier localement les activités électrochimiques et la topographie des échantillons, ces techniques impliquent l'immersion complète de l'échantillon dans la solution d'électrolyte pendant les mesures, ce qui peut induire des changements incontrôlés de leur surface, surtout pour des analyses impliquant des temps de balayage longs. Maintenant, au lieu de localiser l'électrode elle-même, on peut également penser à localiser l'électrolyte, ce qui est connu sous le nom de microscopie de cellules à balayage de gouttelettes (SDC) ou de microscopie à balayage de cellule électrochimique (SECCM). Le concept est de localiser l'électrolyte sous forme d'une gouttelette à l'extrémité de la pointe d'un capillaire étiré, qui est approché de l'échantillon pour ainsi former une cellule électrochimique miniaturisée. Ainsi, les expériences sont menées dans des conditions ambiantes (sans avoir recours à une solution électrolytique externe). Comme les techniques de traction capillaire sont devenues très performantes, la SDC et la SECCM atteignent une résolution latérale suffisamment élevée, pouvant aller jusqu'à l'échelle nanométrique. Toutefois, les gouttelettes peuvent s'épandre de manière aléatoires sur la surface de l'échantillon, notamment en fonction de leur état d'hydrophilie ou d'hydrophobie, ainsi que de la rugosité de l'échantillon, ce qui entraîne des difficultés pour les analyses quantitatives.

Récemment, la microscopie électrochimique à balayage à sonde à gel (SGECM) a été proposée comme nouvelle technique de SEPM. Elle est principalement basée sur une sonde à gel fabriquée par électro-dépôt d'un hydrogel de chitosane avec électrolyte immobilisé sur une microélectrode à disque. La sonde a gel peut être approchée de la surface de l'échantillon de manière précise en contrôlant les forces du cisaillement via une boucle de rétroaction. Les résultats préliminaires ont montré qu'en balayant la sonde à gel à la surface de l'échantillon, sa topographie peut être révélée et la cartographie actuelle peut être générée en appliquant un potentiel approprié entre la sonde et l'échantillon. En comparaison avec d'autres techniques SEPM, la SGECM offre les avantages suivants: 1) possibilité d'opérer à l'air en raison de l'électrolyte préalablement encapsulé/imprégné au sein de l'hydrogel; 2) absence de fuite en raison de la liaison hydrogène entre l'hydrogel et l'électrolyte; 3) détection dans des conditions non perturbatrices en raison de la nature molle du gel.

Cette thèse est consacrée aux développements ultérieurs de la SGECM. Dans le premier chapitre, le contexte des développements de la SGECM est d'abord introduit. Différentes techniques SEPM, notamment les SECM, SICM et SECCM sont systématiquement considérées. Les sondes, les modes de fonctionnement et les applications principales sont présentés, respectivement. En particulier, la SECM est comparée à la technique de l'électrode vibrante à balayage et à la spectroscopie d'impédance électrochimique localisée en se basant sur le cas particulier de la caractérisation de la corrosion localisée. Après cela, la préparation par voie électrochimique des électrolytes à base de gel polymérique est décrite, et la caractérisation des propriétés mécaniques et électrochimiques de l'hydrogel est présentée. De plus, l'instrumentation, la fabrication des sondes à gel, les méthodes d'approche « pointe – échantillon » et les apports de la SGECM sont systématiquement passés en revue.

Comme les autres techniques SPM, la SGECM présente également un problème important de résolution, en particulier en ce qui concerne la résolution latérale, car elle détermine la quantification et les applications. La résolution latérale a deux aspects, la résolution de numérisation et la résolution physique. Le premier est déterminé par le mouvement des unités de contrôle (moteur ou piezo), tandis que le second se réfère à la zone d'échantillonnage d'un seul pixel de mesure. Avec l'instrumentation moderne, la résolution du balayage peut facilement atteindre 0.1 nm, mais la résolution physique est généralement beaucoup plus faible. En conséquence, la résolution latérale de la SGECM est limitée par la résolution physique. Étant donné que la SGECM est une méthode de contact, la résolution physique est essentiellement déterminée par la zone de contact. De plus, en raison de la mollesse du gel, on peut s'attendre à ce que la zone de contact dépende de la force du contact. C'est-à-dire que la résolution latérale pourrait être réglée en poussant ou en étirant le gel après avoir touché l'échantillon. Par conséquent, il est fortement souhaitable de pouvoir déterminer quantitativement la résolution physique latérale en SGECM. C'est ce qui fait l'objet du chapitre II dans lequel la résolution physique latérale de la SGECM est d'abord étudiée en profondeur et quantitativement en marquant les pixels simples et en balayant périodiquement des échantillons modèles. Le premier est réalisé en oxydant localement une surface d'argent, Ag, en chlorure d'argent, AgCl, au moyen de la sonde à gel, induisant un changement permanent de couleur à la surface de l'échantillon. Le second est constitué d'une grille de cuivre (provenant d'un porte-échantillon de microscopie électronique à transmission) déposée sur une plaque de fer. Pour la sonde fabriquée par électro-dépôt de chitosane sur une électrode à disque de platine de 25 μm de diamètre (avec $Rg \approx 2$), la résolution physique latérale à la position du toucher ($z = 0$) est d'environ 50 μm pour la rétroaction actuelle et d'environ 63 μm pour le contrôle des forces de cisaillement. Ainsi, la rétroaction actuelle est plus sensible que le contrôle des forces de cisaillement. En général, la rétroaction actuelle ne peut être envisagée que pour les échantillons conducteurs électroniques, alors que le contrôle des forces de cisaillement est plus polyvalent, en particulier lorsque la conductivité des échantillons à analyser est inconnue. Plus important encore, en raison de la nature molle du gel, la résolution physique peut être réglée avec souplesse en retirant ou en appuyant sur la sonde à gel sur une certaine distance après avoir touché l'échantillon.

Outre les mesures ampérométriques décrites aux chapitres I et II, la SGECM peut également être utilisée pour des mesures potentiométriques. Cela nécessite une adaptation de l'instrumentation et de la sonde. Pour l'instrumentation, nous avons configuré un voltmètre à haute résistance aux entrées (Keithley 6430) en mode SGECM pour cartographier simultanément le potentiel et la topographie. En ce qui concerne la sonde, le chitosane est déposé sur une électrode micro-disque constituée d'un fil d'argent scellé dont la surface a été polie. La surface d'argent est oxydée en AgCl après le dépôt d'hydrogel afin d'assurer une bonne précision du potentiel mesuré. Ainsi, dans le chapitre III, le mode potentiométrique de la SGECM est développé. La fiabilité et la stabilité de la sonde sont prouvées par des expériences sur une électrode d'oxyde mixte indium-étain (à l'aide d'une sonde imbibée de $Fe(CN)_6^{3-}/Fe(CN)_6^{4-}$ comme couple redox). La cartographie simultanée de la topographie et du potentiel électrochimique a été démontrée sur un échantillon modèle composé de bandes de cuivre sur plaque d'aluminium. Les deux métaux sont identifiés par la topographie et la cartographie du potentiel à circuit ouvert (potentiel de corrosion) sans appliquer de différence de potentiel entre la sonde à gel et l'échantillon. Les principaux avantages des mesures potentiométriques en SGECM sont les suivants : 1) le potentiel réel de contact entre la sonde à gel et l'échantillon peut être analysé, ce qui reflète ses propriétés électrochimiques de surface ; 2) l'opération peut être réalisée dans l'air, et la perte d'électrolyte peut être évitée par son immobilisation au sein de l'hydrogel.

Pour les mesures ampérométriques et potentiométriques, la sonde à gel est approchée pour être en contact avec la surface de l'échantillon. La résolution de l'analyse en SGECM est donc basée sur la zone de contact entre la sonde de type hydrogel et la surface de l'échantillon. En raison de la nature molle du gel, celui-ci est déformé pendant les opérations d'approche et de rétractation. Par exemple, le gel peut être pressé lorsque la sonde touche la surface de l'échantillon, et ce de manière contrôlée par rétroaction des forces de cisaillement. Le gel est également étiré lorsque la sonde est retirée en raison de la force d'adhérence entre l'hydrogel et la surface de l'échantillon. Étant donné que la sonde à gel subit au moins un cycle de pressage-étirement-restauration à chaque point d'échantillonnage, elle subit des milliers de fois la déformation mécanique au cours d'un balayage carré. Ainsi, il est essentiel de pouvoir améliorer la stabilité mécanique de la sonde à gel pour assurer la reproductibilité des mesures. Le chapitre IV décrit les efforts préliminaires réalisés dans ce sens par modification chimique du gel de chitosane (réticulation par le glutaraldéhyde). Les propriétés mécaniques et le comportement électrochimique de la sonde à gel ont été analysés. Les mesures de micro-indentation montrent que le module élastique a été amélioré après une réticulation de 2 heures dans une solution de glutaraldéhyde à 0.2%. La voltampérométrie cyclique suggère que le coefficient de diffusion du couple redox est 7 fois plus faible en présence de glycérol dans le solvant. En immergeant la sonde à gel dans des solutions de ferrocène diméthanol, nous avons constaté que le gel déposé et réticulé pendant de courtes périodes (2-4 heures) n'affecte pas de manière significative le coefficient de diffusion de cette sonde redox. Toutefois, le coefficient de diffusion a évidemment diminué après une réticulation de plus longue durée (16 heures).

Une fois que la sonde à gel est approchée pour toucher une surface d'échantillon par rétroaction de force de courant ou de cisaillement, des analyses électrochimiques localisées peuvent être effectuées. En mode ampérométrique, un potentiel (constant ou alternatif) est appliqué entre la sonde à gel et l'échantillon et on enregistre les réponses en courant correspondantes. En mode potentiométrique, le potentiel entre la sonde à gel de référence Ag/AgCl et l'échantillon est enregistré par un voltmètre à résistance élevée aux entrées. Cependant, toutes ces mesures sont effectuées avec un système à deux électrodes. Par conséquent, il serait prometteur de pourvoir construire un système à trois électrodes, dans lequel la signature électrochimique de l'échantillon pourrait être étudiée indépendamment. Sur cette base, le chapitre V pousse encore plus loin le développement d'une sonde à gel intégrée pour la construction d'un système à trois électrodes. La sonde intégrée se compose d'une microélectrode de platine, d'un fil d'Ag/AgCl fixé sur le bouclier de la microélectrode, et d'un capillaire externe imbibé d'électrolyte. Avec le support conçu, la sonde est préparée et régénérée facilement. La chute ohmique, la capacité et la reproductibilité des mesures potentiométriques et voltampérométriques sont systématiquement caractérisées. Les résultats démontrent une chute ohmique négligeable de la sonde intégrée. Pour cette raison, la sonde fonctionne bien pour des détections en mode potentiométrique et voltampérométrique. En outre, l'analyse électrochimique en gouttelettes de faible volume est possible en ayant recours à une telle sonde intégrée. Nous avons ainsi suivi la réaction Fe^{3+}/Fe par la méthode potentiométrique, et le système H_2SO_4/Cu par la méthode de décapage anodique. L' électro-dépôt du chitosane est effectué sur une électrode à micro-disque (électrode interne) qui est ensuite insérée dans une sonde de gel intégrée formée dans un capillaire externe. Une analyse par voltampérométrie cyclique sur une plaque de platine a pu être réalisée avec ce système. De toute évidence, la fabrication d'une sonde à gel intégrée doit être explorée plus avant, mais les résultats préliminaires sont prometteurs pour l'utilisation de telles sondes intégrées pour l'analyse électrochimique localisée au moyen de la technique SGECM.

Cette thèse met l'accent sur des développements méthodologiques en SGECM, ayant permis des analyses plus fiables et quantitatives, ainsi que la mise en œuvre de nouveaux modes de mesure. Bien que la plupart des travaux soient orientés vers la caractérisation de systèmes modèles (surfaces métalliques mimant la corrosion), ils peuvent ouvrir la porte à de nouvelles applications de la SGECM à l'avenir, comme l'analyse électrochimique localisée et la modification de surface d'échantillons de morphologie complexe, l'analyse localisée de la corrosion atmosphérique et la protection des échantillons métalliques issus du patrimoine, ou encore un diagnostic local et des traitements de surface de la peau ou des plantes.

Chapter I General introduction

Electrochemical reactions constitute the basis for various phenomena in chemical and biological processes, such as electrocatalysis[1], energy conversion[2,3], corrosion[4], bioelectricity[5,6], redox proteins in biofilm[7,8]. Conventional electroanalytical methods such as chronoamperometry and cyclic voltammetry have been well developed for studying the electrochemical reaction kinetics and mass transport of reactants/products at electrochemical interfaces[9–14]. However, they could only provide the global behavior of the entire electrode interface, which cannot fulfill the growing demand for understanding the materials and interfacial electrochemistry at micro- and nano-scale[15,16]. As a consequence, researchers have been constantly developing methodologies to improve the spatial resolution of electrochemical measurements. A powerful method is based on scanning probe microscopy (SPM), where the probe localizes the electrode or the electrolyte for electrochemical measurements. This category of SPM is denoted as scanning electrochemical probe microscopy (SEPM).

Recently, a new SEPM technique has been proposed named as Scanning Gel Electrochemical Microcopy (SGECM)[17]. It is based on a gel probe fabricated by deposition of hydrogel on a micro-disk electrode with electrolyte immobilized. SGECM combines the highlights of SEPM and gel polymer electrolytes. Thus, it can be operated in air with the controllable spreading and leakage of solution on the sample surface. In this thesis, new measurements of SGECM have been further developed and the gel probe is improved for quantitative analysis. Herein, for having a whole view of development of SGECM, the related background is introduced in this chapter. The SEPM and gel polymer electrolytes are reviewed in **Section 1.1** and **Section 1.2**. And the SGECM is systematically introduced in **Section 1.3**.

1.1 Scanning electrochemical probe microscopy

SEPM is a category of SPM that employs micro- or nano-scale probes of electrode or electrolyte for measuring spatially localized electrochemical signals. This technique now enables high spatial resolution through precise position controlling. The major advantage of SEPM over conventional microscopy is that various microprobes can be equipped to sense the topography and electrochemical activities of a variety of surfaces in situ under wet or air conditions. With around three decades of development, SEPM techniques now encompass a diversity family. Scanning electrochemical microscopy (SECM), scanning ion conductance microscopy (SICM) and scanning electrochemical cell microscopy (SECCM) are more typical and well-known. Consequently, in this section, probes, measurement modes and specific applications of these three SEPM techniques are introduced, merits and drawbacks of techniques are also summarized and compared.

1.1.1 Scanning electrochemical microscopy (SECM)

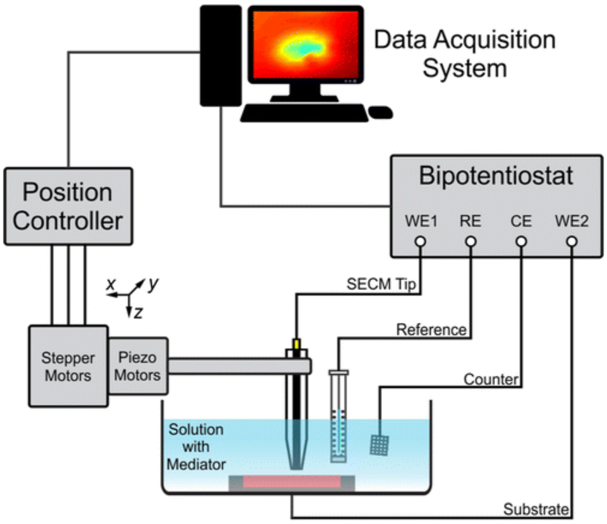

Figure 1.1 Scheme of a SECM instrument[18].

SECM was first introduced concurrently by the Bard[19] and Engstrom[20] research groups in 1989. It was initially developed for imaging topography of surface, but later has become the most widely used method for measuring local electrochemical reactivity of surfaces. After 30 years of development, it is now a well-established and commercialized technique for measuring localized electrochemistry. During SECM measurements, an ultramicroelectrode (UME) is positioned close and scanned over the sample surface that is immersed in bulk solution, as shown in **Figure 1.1**. The movement of UME in three dimensions is precisely controlled by step motors and piezo positioners. The electrode is scanned over the samples with the current response recorded through bipotentiostats. The UME and precise instruments enable high temporal and spatial resolution of SECM. Based on this, SECM has been used in a variety of fields (*i.e.* energy, biology, corrosion, surface modification, *etc.*).

1.1.1.1 Probes for amperometric and potentiometric analysis

Probe is the heart of SECM experiments as it enables the local electrochemical reactions and determines the spatial resolution in the same time. According to different functions, SECM probes are generally divided into two types: amperometric and potentiometric probes. UMEs are usually applied as amperometric probes. UMEs present several significant advantages over macroelectrodes, including a reduced ohmic (iR) drop and a faster steady-state response. Several different geometries have been reported including disk, hemispherical, conical and ring probes (introduced in the following chapters), *etc*. The most common one is the disk microelectrode. Normally, it's fabricated by sealing a metal wire or carbon in a well-pulled capillary, and the tip of the electrode is polished for exposing the active part. The ratio between the insulating shield and the electroactive core is defined as R_g, which is a characteristic parameter for SECM probes. Well-established theory about the disk microelectrode potentiates quantitative analysis of SECM. The images of several disk microelectrodes are given in **Figure 1.2**. Till now, mass produces of this microelectrode is still changing because of the limitation of microfabrication. Most of probes are home-made leading to the relative high price from US$140 to 400 per one. The potentiometric probes are mainly ion selective probes (including pH detections). Now, the main drawback of the potentiometric probe is the large RC time constant, and therefore long response time of the cell. In order to avoid the image distortion, a relatively long equilibration interval has to be allowed between each sampling point. Limited by this, this type of probes has more requirements in corrosion and biological measurements.

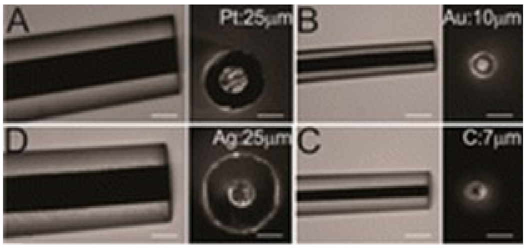

Figure 1.2 Side and top view optical images of several disk microelectrodes[21]. Pt – 25 μm, $R_g \approx 2.7$ (A), Au – 10 μm, $R_g \approx 3.2$ (B), C – 7 μm, $R_g \approx 3.2$ (C), Ag – 25 μm, $R_g \approx 2.7$ (D).

1.1.1.2 Measurement modes

In order to accommodate different applications, a wide variety of operation modes of SECM have been developed. Feedback mode is a most common mode in SECM. It is carried out by detecting the current of the redox mediator at the tip of UME. **Figure 1.3** shows the different electrochemical behaviors as the electrode is approached upon the substrate with different conductivity. When the probe is positioned into a bulk solution and far away from the sample surface, that is to say, the tip-to-sample distance is greater than 10 times of radius of electroactive core in the electrode, only the steady-state current ($i_{T,\infty}$) is measured in **Figure 1.3 A**. For a disk-shaped electrode with hemispherical diffusion, $i_{T,\infty}$ is defined as:

$i_{T,\infty} = 4nFDCa\beta$ (**Equation 1.1**)

Where, n is the exchanged electron number in redox reaction, F is the Faraday constant (96485 A s mol^{-1}), D is diffusion coefficient of redox species in solution (cm^2 s^{-1}), C is the concentration of redox species in solution (mol cm^{-3}), a is radius of electroactive surface of electrode (cm), β is the geometry coefficient of the electrode. If the UME is close approximately an inert surface, diffusion of redox species is hindered by the physical barrel of substrate. This results in the depletion of active species between electrode tip and substrate, so the measured current is hindered. This phenomenon is named as "negative feedback", as shown in **Figure 1.3 B**. In the case of the electrode positioned close to a conductive substrate, the diffusion of redox species is again blocked by the surface. However, the consumed redox species could regenerate again on its surface. By this reason, the local flux of redox species is accumulated, thereby an increasing current is measured. This is known as “positive feedback”, as shown in **Figure 1.3 C**.

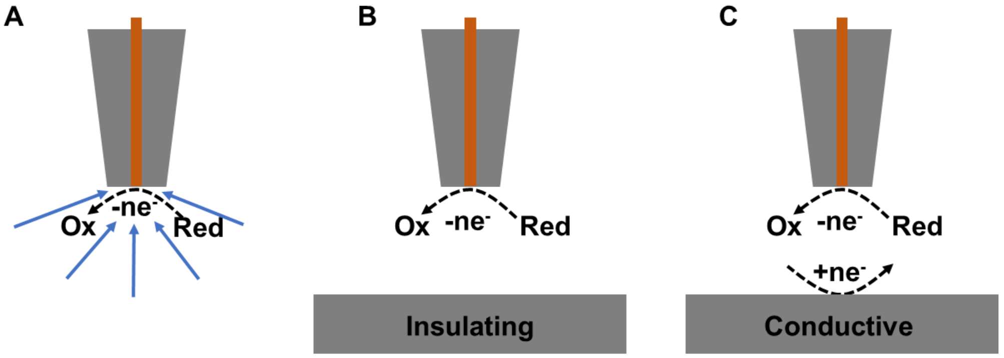

Figure 1.3 Feedback mode of SECM. In bulk solution (A), negative feedback (B), positive feedback (C).

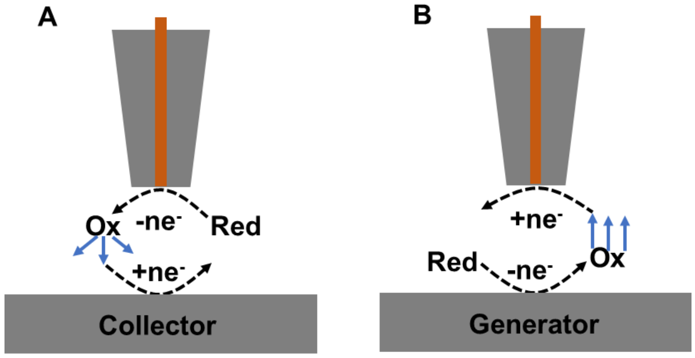

Figure 1.4 Scheme of generation/collection (GC) mode of SECM. Tip generation – substrate collection (TG/SC) mode (A), substrate generation – tip collection (SG-TC) mode (B).

Generation/collection (GC) mode consists of two types of operation methods: tip generation – substrate collection (TG/SC) and substrate generation – tip collection (SG-TC). In TG-SC mode, the electrode tip is held at a potential for generating electrochemical reaction and the substrate is for collecting the products by having other reaction (**Figure 1.4 A)**. Current response is measured at both tip and substrate. When the tip to substrate distance is very small (normalized distance $L = d/ a \leq 2$, d is the tip to sample distance), tip generated species will mainly diffuse to the substrate. Consequently, TG-SC mode is particularly used in scanning electrocatalysts[22,23] or surface modification. Alternatively, in SG-TC mode, the new species is generated by the substrate and collected by the tip (**Figure 1.4 B)**. Usually, the surface area of the substrate is huge compared with the electrode, in this way, the diffusion layer of the probe is much larger than electrode active area. Thus, the collect efficiency is low and the substrate surface is lack of steady state.

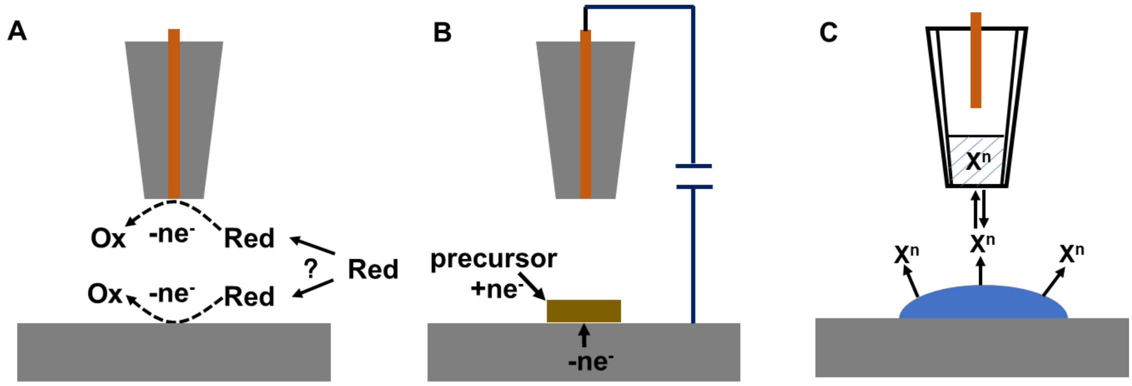

Figure 1.5 Scheme of redox competition mode (A), direct mode (B) and potentiometric mode with an ion selective electrode (C).

For overcoming the sensitivity problems of SECM in catalysts analysis, redox competition mode was proposed. As illustrated in **Figure 1.5 A,** In this mode, the substrate and the probe compete for the same redox species in solution such that the decrease of the tip current is an indication of surface electroactivity[26]. The competition mode is not so prominent as feedback and GC modes, but it's taken in the measurement of surface catalytic activity[26] and corrosion[27].

Direct mode has been proposed by Bard and co-workers in the very beginning of the SECM[28]. In this mode, a bias is applied between UME and substrate with the former as auxiliary electrode and the latter as working electrode, as shown in **Figure 1.5 B**. In this mode, the substrate is oxidized immediately by applying a positive bias or a precursor is electrodeposited on the substrate. The reaction is highly affected by the electric field between UME and substrate. Thus, smaller tip to sample distance allows for higher physical resolution. In past few decades, the direct mode is mainly used patterning or surface modification[29-31].

Apart from applying potential on the microelectrode (and the sample) and measuring the current response, SECM can also be conducted in potentiometric mode. It allows local potential is measured at the probe to evaluate the local solution composition and therefore surface activity[32,33]. As shown in **Figure 1.5 C**, the potential between an inner electrode (normally is an ion-selective electrode in probe) and outer reference electrode is measured. Since the signal is potential not current, potentiometric mode has several advantages including high selectivity, measurement of non-electroactive species and negligible disturbance to the concentration and oxidation state of the analyte species.

1.1.1.3 SECM with distance regulation

For the measurements of diffusion-controlled reactions, tip current i_T on a UME with fixed active diameter is mainly influenced by the tip to sample distance. When electrode is far away from the sample surface, responded current is $i_{T,\infty}$. Approaching the electrode close to the sample surface, the current is changed gradually depending on the conductivity of sample (as discussed in feedback mode). The alternation i_T versus tip to sample distance provide a method to position of UME over samples. However, when the sample is rough and partially conductive, like a conducting spot recessed in an insulator, it is challenging to approach the electrode by feedback mode and "crash-tip" is caused frequently. So, it is important to regulate the distance based on non-electrochemical signals, such as shear force and atomic force microscopy (AFM).

Shear force base position is derived from scanning near field optical microscopy (SNOM) was firstly introduced for SECM positioning in 1995[34]. The probe tip is stimulated to have oscillation vibration during the approaching. When the probe is closed to the sample surface in solutions or air, the damping of the tip is altered by the hydromechanics of the mediator, capillary phenomenon, and the Van der Waals force. This allows shear force controls a constant distance between tip and substrates. The non-electrochemical position approaching in shear force SECM allows discriminating the topographical information and the electrochemical signal. Instead of a laser/split photodiode and tuning fork configurations, the new generation of shear force SECM applies a piezo detector in sensing the damping of the tip[13,14]. As illustrated in **Figure 1.6**, two piezoelectric plates connected with lock-in amplifier are mechanically mounted to the glass shield of the electrode. One serves as actuator for stimulating the vibration of the electrode, and the other is the sensor for amplitude and phase of the tip oscillation. The signals are frequency dependent in the hundreds of kHz range, and usually the frequency that offers the highest signal-to-noise ratio is selected for approaching the probe. In shear force SECM, a probe with long flexible needle shape is required for optimizing the sensitivity of shear force signal. So far, platinum disk electrode inlaid in glass capillary[34], nanotip arrays fabricated by wet chemical etching of ordered optical fiber bundles[38], and carbon fibers sealed in capillary[39] have been used as probes in shear force SECM. Owing to the range of electrode probes that can be employed, the applications of shear force SECM are broad in corrosion[37,39] and electrocatalysis[40,41].

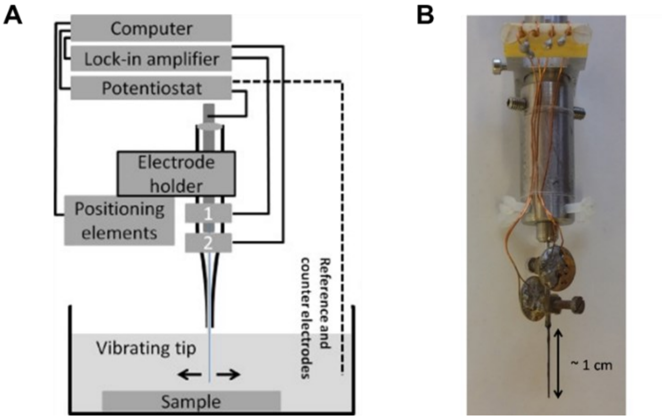

Figure 1.6 Shear force SECM setup[36] (A), holder in shear force SECM (B)[38].

Although the shear force feedback allows keeping the probe-sample distance constant, the exact value of the distance is difficult to be calibrated as the signal is highly system dependent. A better alternative for controlling the distance is AFM-SECM[42–44]. The main idea is to implement SECM electrodes into AFM cantilevers. The topography and electrochemical activities of samples could be characterized simultaneously at an excellent lateral resolution. This is the major advantage of AFM-SECM. As the probe is the key issue of AFM-SECM, the fabrication becomes highly important. Normally, as shown in **Figure 1.7**, the following methods are used for preparing the probe of AFM-SECM[42,45]: (1) Fast and easy fabrication of probes by etching and insulating a conductive wire. This is the first reported approach combining scanning electrochemistry with AFM[46]. The probe, consisting of etched metal insulated at all but the apex of the tip, offers dual electrochemical and force sensing by direct contacting with the sample surfaces (**Figure 1.7 B**). Later, the lift mode was also achieved, in which, the topography is recorded in the first line scan and the electrochemical measurements are performed in the second pass by lifting the probe a pre-defined height[47] (**Figure 1.7 C**). (2) microfabricated bifunctional probes, which consists of a sharp non-conductive AFM tip and a conductive electrode recessed in the apex of the tip (**Figure 1.7 D**). Using this method, the topographical and electrochemical imaging positions on the probe are separated by a fixed length. This allows both measurements to be made simultaneously within a single pass.

Corrosion processes could be accessed in situ by AFM-SECM to prove deeper insight. Both topographical change on the substrate and oxidation products of the corrosion process and/or substrate passivation were detected synchronously[48]. Additionally, AFM-SECM has been used as a high-throughput serial read-out technique for imaging dense molecular nanoarrays. Owning to the high resolution, as little as a few tens of copies of redox-labelled macromolecules immobilized on individual nanodots can be detected[49]. More importantly, AFM-SECM shows many applications in bioanalytical sensing because of the flexible chemical detection capabilities of SECM[50, 51]. Recently, immunocomplexes anchored to single viral particles[52] and protein pores inserted into supported lipid membranes[53] were screened. AFM-SECM (and its diverse modes of operation) will undoubtedly find further use on biologically relevant samples, especially considering further efforts toward the development of AFM-SECM capability[54].

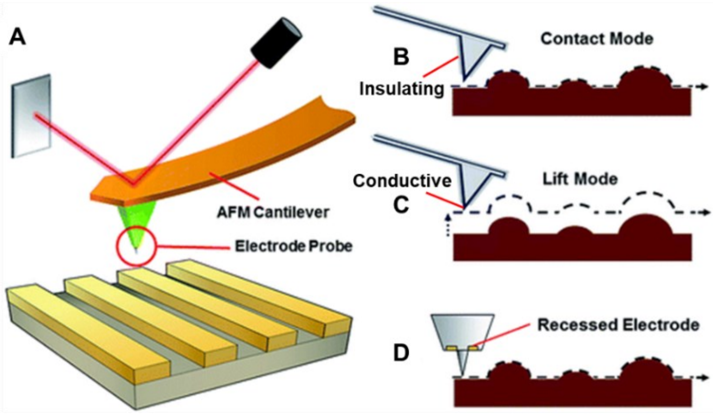

Figure 1.7 Scheme of the AFM-SECM (A), probes by etching and insulating a

conductive wire (B) and (C), probe with a recessed electrode (D)[55].

1.1.1.4 Characterization in corrosion, energy and biology

Corrosion: Corrosion involves multiple heterogeneous electron transfer reactions between a material with its surrounding environment, resulting in the deterioration of material and its properties. As localized corrosion, also known as pitting, is one of the major interests in corrosion studies, it is among the earliest applications of SECM for studying the corrosion phenomena and mechanisms at high spatial resolution[56,57]. Feedback and GC modes are usually taken in the amperometric analysis of corrosion. Operation of SECM in feedback mode is sensitive to the topography changes of the coating on metal in aqueous or corrosive environment[58–60]. An indirect redox mediator is used to probe the difference in intrinsic reactivity of the various phases of composing alloy. In SECM GC modes, a direct mediator could be probed then mainly used to investigate corrosion properties. In most cases, the dissolved and produced ions/molecules upon immersed metal surfaces can be collected at a nearby microelectrode[24,61–63]. Potentiometric analysis using ion-selective electrodes is also applied in corrosion characterization. Normally, the ion-selective electrode and pH-sensitive electrode are miniaturized in a double-barrels electrode. In this way, simultaneous recording of dissolved metal ions and pH concentration distributions were obtained in one scanning[64–69]. Although with the development of solid contact ion-selective microelectrodes of smaller internal resistance, the slower constants associated to the potentiometric response is the main limitation for widespread use.

Besides SECM, other related SEPM techniques, like Scanning Vibrating Electrode Technique (SVET) and Localized Electrochemical Impedance Spectroscopy (LEIS) are also widely applied in local analysis of corrosion. Both techniques detect the local potential distribution near the sample as a result of AC excitation, which reflects the current distribution that originates from the electrochemical reactions on it. In SVET[70], the microelectrode is vibrating perpendicular to the sample (in *z* axis) at a set frequency while the potential versus a reference electrode is recorded. The measured potential gradient signal should have the same frequency as the vibration, thus can be filtered by a lock-in amplifier and is further converted to the local current using Ohm's law. This could eliminate the noise in the scanning process, thereby effectively improve the sensitivity of analysis. SVET is easy to set up for providing real time mechanistic information of corrosion, and it can be extended by using ion-selective microelectrodes. Like in SECM, the lateral resolution of SVET also depends on the sample-probe distance. Generally, SVET can discriminate two adjacent points of interest when the probe is at a height that equals to half of the distance between them. For example, in order to identify two points separated by 10 μm, the probe must be at the most 5 μm above the surface, which is impractical for common SVET probes of 10 μm size and 5 μm vibration amplitude (20 μm peak-to-peak)[70]. This limits the lateral resolution of the measurement. In addition, the lower current detection limit depends on the resistivity of the electrolyte. As the electrolyte is usually quite conductive in electrochemical systems, this limits the sensitivity of current analysis. In the case of an anodic active sample, the cathodic activity is spread through the rest of the surface and the current density is too low to be detected. Moreover, the vibration will perturb the local mass transport near the sample and complicate the quantitative analysis. LEIS was then developed based on the SVET[16,71]. The AC excitation signal is applied not on the probe in the form of vibration, but instead on the sample in the form of potential or current like the global electrochemical impedance spectroscopy (EIS) method. This induces a local current distribution depending on the local reactivity of the sample, which is analyzed by the potential difference on a dual-microelectrode probe configuration. Like in global EIS, the local impedance is derived from the potential excitation and current response. The most attractive character of LEIS is providing local impedance in frequency domain, which is difficult to be measured by other methods. However, like the global EIS, it naturally takes long time for low-frequency measurements. Thus, for generating a map by laterally scanning the probe, it is only practical to measure high-frequency signals which limits the information that can be obtained[16].

SECM and the related techniques SVET and LEIS are well-developed and commercialized for corrosion analysis, especially for the localized corrosion. They can recognize corrosive regions of a passive film or a coating, and allows mapping with a resolution in micrometer range or even below[24]. This fits the size of pitting or pinholes in coatings, and therefore may provide the information on the evolution of corrosion processes. Besides, corrosion is usually a relatively slow process (except for very active metals like magnesium), thus it does not require high sampling frequency. Typically, for following a corrosion process of hours or even days, the sample can be considered "unchanged" while generating a map that takes tens of minutes. However, the quantification is still a challenge due to the complexity of corrosion processes, especially for SVET and LEIS.

Energy: SECM has been proven to be a powerful technique to investigate the process of energy production, like the evolution of hydrogen (HER) or reduction of oxygen (ORR) in electrocatalysis[72–77], batteries[78–81], solar cells[82–84], fuel cells[85] and so on. HER and ORR are the focus of applications and have been mainly developed [53–56]. The SG/TC mode has been demonstrated to be a very effective method to study the HER and HOR processes as well as to screen local inhomogeneities at catalytic substrates. The debate that the decreasing size of metal nanoparticles brings the enhancement of the electrocatalytic activity has been clarified by SG-TC SECM[90]. Comparison with conventional electrochemical approaches, the methodology described allows intrinsic nanoparticle reactivity to be investigated free from electronic and structural effects induced by the electrode substrate. TG/SC mode in SECM is also reported in revealing the ORR in acidic solutions[86]. The UME tip was placed in proximity of the substrate and biased at a potential at which the oxidation of water to oxygen occurs, while the substrate potential was held at a value at which the oxygen is reduced to water. By changing the substrate potential, it is possible to obtain a polarization (current-potential) curve, which depends on the electrocatalytic activity of the substrate material. In contrast to SG/TC mode, TG/SC mode has a drawback of less sensitivity. Because the substrate works as a collector, the efficiency of detection is inhibited by the large area. RC mode in SECM also allows the characterization of energy associated materials[77]. In a bipotentiostatic experiment, both the UME tip and the substrate compete for the same analyte. The kinetics of the ORR on multiwalled carbon nanotubes (MWCNTs) and cobalt protoporphyrin (CoP) were studied by RC-SECM[74,91]. The amount of hydrogen peroxide (H_2O_2) produced, the number of electrons exchanged during oxygen reduction, and the heterogeneous rate constant were derived. In RC-SECM, the signal is affected by the background current of the sample, this causes the limitation of the resolution. Perhaps it can be further promoted by decreasing the size of the UME tip.

Biology: SECM also plays a key role in identifying the different locations of biological entities by the topographical and electrochemical information. A wide variety of biomolecules and substrates have been investigated including enzymes, proteins, DNA, and single cells[92,93]. Among them, enzymatic sensing is a major application of SECM in the biological field. The first case using SECM to analyze enzymatic reactions was reported in 1992[94]. In following two decades, different active enzymes, like diaphorase[95,96], HRP[97,98], glucose dehydrogenase[99], ceruloplasmin[25], and cytochrome c peroxidase[100] have been investigated by SECM using different operating modes. Proteins have been tested as well by SECM-based platforms for more than 15 years. The amino acids[100,101], cytochrome[102,103], antibody and antigen[104], leukocidin[105], peptides[106,107], and bacterial flagellin[108] are included. Recently, SECM has been applied on the detection of multiple proteins[109,110]. Regarding the DNA tracking and measuring, the attractive points of SECM are sensitivity and low cost. Till now, DNA microarrays[111], single-stranded DNA (ssDNA)[111], double-stranded DNA (dsDNA)[112], and DNA hybridization[112] *etc.* have been successfully investigated by the kinds of modes of SECM. Application of SECM to in-situ image the living cells in vivo conditions has the possibility of avoiding the artefacts. Consequently, SECM has been used extensively to study cells including human cells[113,114] and animal cells from rats[115], dogs[116], and cows[117]. The approach curve allows preciously positioning the probe over cells and obtaining the kinetics parameters of the redox reaction in cells.

1.1.2 Scanning ion conductance microscopy (SICM)

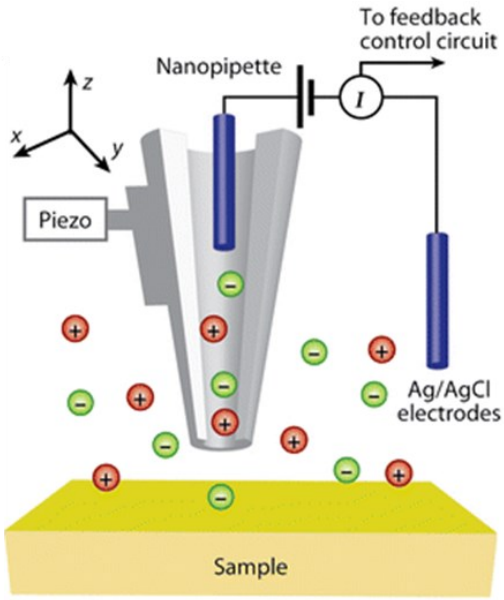

Figure 1.8 Scheme of the scanning ion conductance microscopy (SICM)[118].

Besides electron transfer on a solid microelectrode, the ion transfer can also be spatially confined. This is achieved through a pulled capillary, where the opening of the tip serves as the pathway of ions. The technique has a long history in electrophysiology, known as patch clamp, and was introduced for measuring electrochemistry by Hansma and co-workers at the same time with SECM[119]. Like SECM, SICM was also initially developed as a noncontact topographical imaging tool. The scheme is illustrated in **Figure 1.8**. Instead of micro-disk electrode, a micro- or nanopipette scans over samples that are immersed in the electrolyte. The ion conductance current is measured between an electrode in the pipette and another electrode in the bulk solution. Like in SECM, the current also depends on the probe to sample distance, which provides a feedback signal for accurately mapping the sample topography without physical contact. Based on the advanced capillary fabrication techniques, the opening of capillaries at sub-micrometer and nanometer scale could be fabricated reproducibly. This offers a high resolution of SICM.

1.1.2.1 Measurement modes

Varied methods for determining the topography of samples with SICM have been proposed, including of the non-modulated (DC) mode, distance-modulated (AC) mode and hopping feedback mode. The Scheme of these three modes of SICM is given in **Figure 1.9**. In non-modulated mode, a voltage is applied between two QRCEs in SECM and the responding direct current (DC, I_d) is very sensitive to the tip to substrate distance (d) (**Figure 1.9 A**). The relationship is expressed as follow[118]:

$$I_d = \frac{U}{R_T} = \frac{U}{R_p+R_{ct}} \approx I_{MAX}(1+\frac{\frac{3}{2}\ln(\frac{r_0}{r_i})}{h\,d})^{-1};\ I_{MAX} = \frac{U}{R_p} \quad \textbf{(Equation 1.2)}$$

Where, R_T is the total resistance of pipette, R_p is a combination of the pipette resistance, R_{ct} is the access resistance between the pipette tip and the sample surface r_i is the inner radius of the tip opening, r_0 is the inner radius of the tip base, h is the tip length.

Since the R_p, R_{ct}, r_i, r_0 and h are constants for one pipette, the current I_d is just depend on the tip to substrate distance d. When the pipette is far away from the sample surface, the current is I_{MAX}. When the d gradually decreases, the current is slowly inhibited. However, this method hardly to detect roughness samples, which prone to electrode drifts and likely destroy the pipette or sample surface.

Improvements have been made is to use alternating current (AC) detection instead of DC signal, named as distance-modulated mode (**Figure 1.9 B**). The AC signal is applied to z-piezoelectric positioner leading to the vertical vibration of the probe tip. Oscillation at an frequency (typically in 100 Hz - 1000Hz scale) results in an ionic current response at the same frequency that can be measured with a lock-in amplifier, which works as a feedback signal to modulate the z-position of the probe[120]. When the probe is far away from the surface (normally more than one tip diameter), the AC signal is small because there is little difference in the resistive state at the furthest and closest points of the probe–surface distance during the oscillation. While, as the probe close to the surface, there is a noticeable AC signal change because of the resistance alteration during the oscillation period. Comparing with DC component, AC component has a major advantage of much steeper response and a larger detected distance, which allows characterize more complex samples. Moreover, the AC component is less prone to DC drifts comparing with the DC component.

In hopping mode, the probe repeatedly approaches the sample surface and withdraws before touching at each sampling point. A pre-scanning is performed in a small area to estimate surface roughness, as shown in **Figure 1.9 C**. The scanning with adjustable resolution could be achieved for different areas as required. Nevertheless, the imaging with hopping mode SICM is very time-consuming. For solving this limitation, alternation the step size during measurement and pre-scanning of the target area could be used.

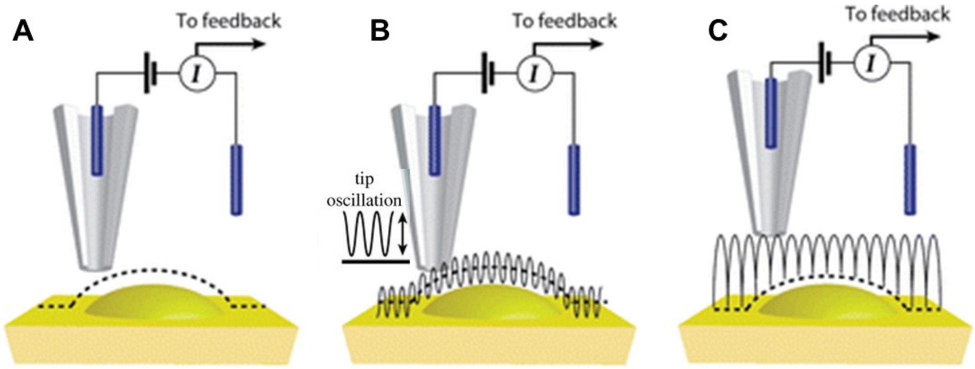

Figure 1.9 Scheme of the different modes of SICM. Non-modulated (DC) mode (A), distance-modulated (AC) mode (B), hopping feedback mode (C).

1.1.2.2 SICM coupled systems and applications

Since the non-contact modes of SICM bring less external stimulation for biological systems, SICM is mainly used in bioanalysis. Considerable works were reported about the combination SICM and other techniques to obtain additional information of samples. Before the development of distance-modulated feedback, AFM was combined with SICM to control the position of the probe with a more stable way[121]. In SICM/AFM, the pipette is utilized as both a probe for electrochemical analysis and a cantilever as a force sensor. In this setup, the topography could be imaged by the contact and tapping modes of AFM, and the current could be detected with the SICM simultaneously. It's reported that a synthetic polycarbonate membrane with pore size of 200nm was characterized. Coupling with scanning near-field optical microscopy (SNOM), new SICM system allows simultaneous recording of photonic information with SICM images[122]. The tip to sample distance is controlled by the feedback of SICM. More topographic details of samples are recorded by the optical microscopy. As important cells constituting heart muscle chambers, cardiac myocyte cells were analyzed. Light and dark bands of material/striations in cells are imaged clearly. Combination of SICM and confocal fluorescence microscopy has been developed to a new technique named as scanning surface confocal microscopy (SSCM)[122]. The tip to sample distance is also modulated by SICM probe. Light from the confocal microscope is focused immediately in the volume below the probe tip. Consequently, topography and fluorescence images are obtained from once detection. The interaction of single virus-like particles with the cell surface was recorded by this technique.

More recently, a new system SICM coupling with SECM was reported by Takahashi and co-works to obtain the chemical information of samples in physiological conditions with a high spatial resolution[123,124]. The most attract of this configuration is using SICM for approaching the probe and SECM for studying charge transfer kinetics of reactions. As shown in **Figure 1.10**, two types of SECM-SICM probe including ring and double barrel shapes were fabricated for simultaneous topography and electrochemical imaging. The ring probe is fabricated by sputtering Ti/Pt or Ti/Au coating on the shield of a pulled capillary followed by insulation with an anodic electrophoretic paint. Afterwards, the apex of the capillary is milled by a focused ion beam to expose the electroactive area and form an ion transport aperture[123] (**Figure 1.10 A**). The position of the probe is controlled by the ion current flowing between Ag/AgCl electrodes located inside the nanopipette and the outside solution. With this probe, the localized activity of the enzyme spot in the protein microarray was detected with submicrometer resolution. The distribution of ion channels on superior cervical ganglion (SCG) cells and A6 cells were also mapped with precise distance control. The double barrels probe is fabricated by pulling of a theta capillary (**Figure 1.10 C**)[124]. One barrel filled with carbon works as the SECM nanoelectrode and the other barrel filled with electrolyte for SICM analysis. Comparing with the ring probe, the size of double-barrels probe is smaller and the insulation is considerably better because there are no pinholes or recessing of the electrode. The topography of different rat adrenal pheochromocytoma cells (PC12) and the release mechanism of neurotransmitter from PC12 cells were obtained with a high resolution. The advantage of this type probe is that the barrel filled with electrolyte can be used to apply different reagents for local stimulation of the cell: the voltage-driven local chemical change produced by the nanopipette is effective for controlling the function of the biological sample[125].

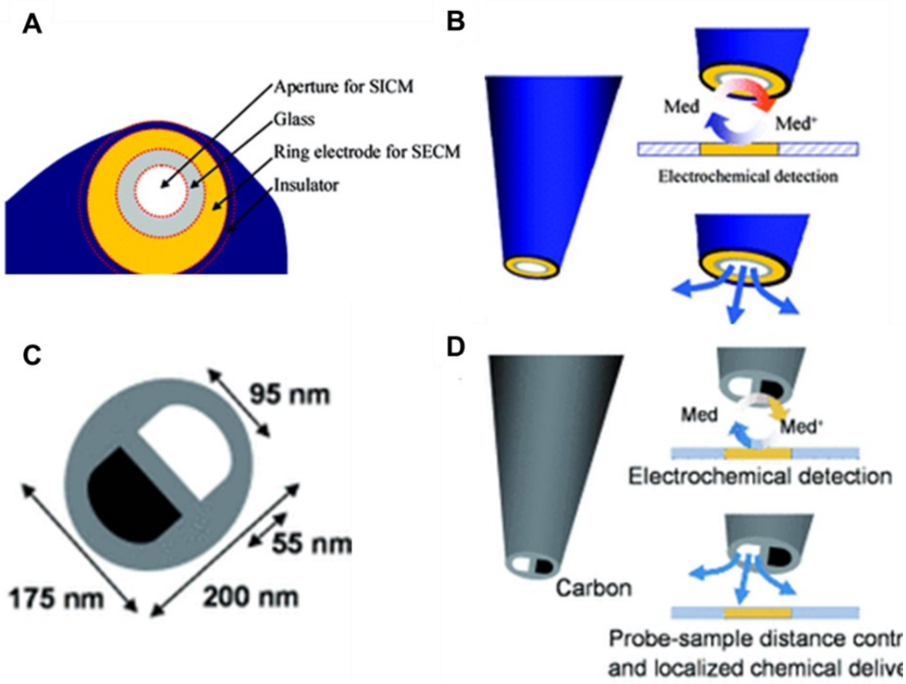

Figure 1.10 Schemes of two types SECM-SICM probes., Ring probe (A) and (B), double barrel probe (C) and (D).

1.1.3 Scanning electrochemical cell microscopy (SECCM)

SECM and SICM are powerful techniques for local electrochemical analysis. Nevertheless, both of techniques are carried out with the entire sample is immersed in the electrolyte during the measurements. On the one hand, this provides access to *in-situ* electrochemical behavior at the interface. On the other hand, the sample surface might change during the long-term immersion. To overcome this issue, scanning droplet cell (SDC)[126,127] or scanning micropipet contact method (SMCM)[128] was proposed by filling the electrolyte into capillaries then a droplet comes out and touches on the sample surface. Thus, the measurements could be achieved in air and *in-situ* activities of sample are tested. Same with the SICM, this kind of technique also enables high spatial resolution owing to the matured pipette pulling methods. Moreover, different with

SECM and SICM, this kind of technique provide the direct contact between droplet and sample surface, this enables probe to be approached on targeting point of the sample immediately. Comparing with SECM, in which, the electrode approaching is influenced by the conductivity and roughness of samples, the direct approaching is only related to the conductivity/activity.

Based on SDC/SMCM, local electrochemical analysis with capillary techniques have been further developed to a upgraded generation: SECCM[129]. Rather than a two-electrode configuration in SDC/SMCM, the main idea of SECCM is to construct a nanosized three-electrode system in a droplet that is in contact with the sample surface. This is achieved with a pulled theta pipet, which accommodates a counter electrode and a reference electrode. When the probe is in contact with a sample, a meniscus of electrolyte comes out from the end of the pipet and spreads on the sample surface, bridging the circuit with the sample as working electrode. The probe scans over the sample with three-dimensional motion control, allowing topographical and electrochemical mapping to be measured[54,130–133]. The scheme of SECCM is shown in **Figure 1.11 A**.

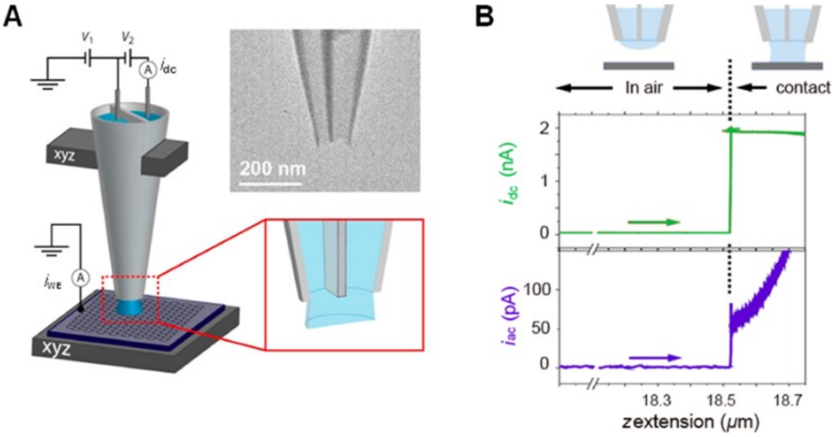

Figure 1.11 Scheme of the scanning cell electrochemical microscopy (SECCM) (A). Approach curves of SECCM probes with DC and AC ion conductance current as a function of z extension toward the substrate (B)[132].

1.1.3.1 Working principles and operation modes

The probe in SECCM is approached to the surface of interest either with DC or AC signal according to the conductivity of the sample (**Figure 1.11 B**). In DC approach, a potential bias (V_2) is applied between two QRECs, the change of ion conductance current (i_{dc}) is a feedback signal of probe position. In AC approach, the probe is modulated sinusoidally by the oscillation through a lock-in amplifier. Once the contact between meniscus and surface is established, the ion current across the meniscus (i_{ac}) shows a periodic modulation at the same frequency of oscillation due to the deformation of the meniscus. The DC map is relatively featureless although it is sensitive to identify variations in the size of the meniscus. Well, the AC map usually appears remarkable resolution, especially employing a droplet with several hundreds of nanometer in diameter. Since the AC signal comes from the ion conductance current in meniscus and it is very sensitive to the deformation of the meniscus, AC component is more versatile in the analysis of insulator or semiconductor. Herein, AC conductance magnitude is usually used as the feedback parameter to keep a set distance between probe and sample surface in SECCM. For substrate (working electrode), the potential is controlled through applying a potential (V_1) with respect to the ground while maintaining the constant V_2. Due to the barrels of the pipette are typically symmetrical thus with same size, and the QRCEs are identical, the effective potential of substrate versus QRCEs is approximately $-(V_1 + V_2/2)$. The current of substrate (i_{we}) is measured as well to reflect the activity of substrate. For avoiding the crush of probe and unknown deformation of meniscus, the probe should keep vertical to the sample surface.

Owing to the direct contact feedback of SECCM, electrochemical properties of a surface could be probed locally with integrated probe position feedback. This brings the advantage of application of the well-known electrochemical method, such as cyclic voltammetry (CV). Adoption the hopping mode approach of SICM, voltametric analysis on a series of targeted surface features was performed spatially in SECCM hopping mode[134]. The scheme is shown in **Figure 1.12**. The probe is approached over a sample surface with a low speed. Once in meniscus contact, the pipet is held for 1s to allow the stabilization of the droplet. Potential sweep then is applied to achieve the CV scan. After finishing one sampling point test, the probe is retracted quickly to break the meniscus and remove laterally to the next point. The dynamic electrochemical flux movies over a wide potential range could be detected, thus, this mode enables a quantitative analysis across a surface of interest. However, time-consuming is a drawback of this measurement. This is caused by two issues: one is the low approaching speed and applied hopping mode. The other one is the long-term CV analysis.

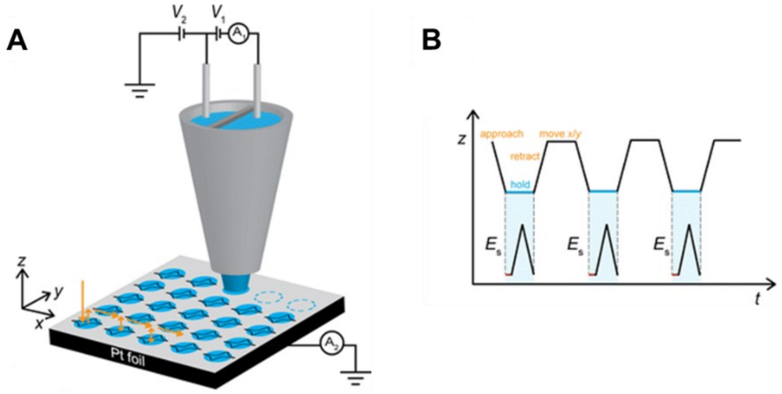

Figure 1.12 Scheme of the SECCM hopping mode (A). Scheme of pipet-to-substrate separation (top) and the corresponding potential profile (bottom) applied to the substrate with time (B). The red lines in the potential profile indicate the hold time before recording a CV, typically 1 s.

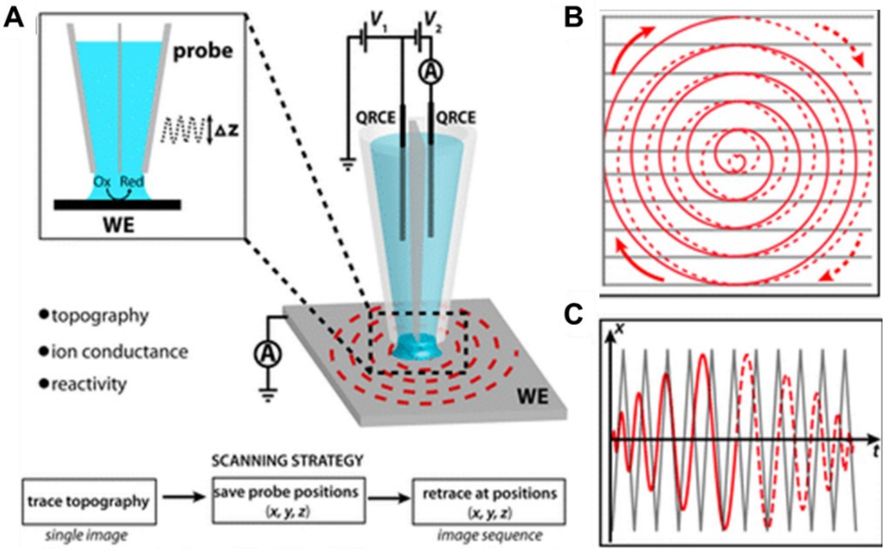

Figure 1.13 Scheme of the fast scanning SECCM routine. An illustration of the SECCM operation principle (A). The implemented spiral scan pattern for high-speed imaging (red solid and dashed lines denoting forward and reverse spirals) compared to typical raster routine (gray lines). The arrows indicate the direction of the probe translation (B). Corresponding probe trajectory on the x-axis during spiral (red solid and dashed lines) and raster (gray lines) scanning (C)[135].

Besides of above constant-distance modes, the constant-time mode was developed in SECCM for a fast scan. Momotenko *et al.* recently reported a new high-speed electrochemical imaging method in SECCM[135]. The response time of positionable feedback and the piezoelectric positioners are key points for the fast scanning technique. In the time constant mode, the probe is modulated by vertical AC oscillation, which is limited at the upper end by the piezoelectric actuator resonance and the corresponding phase shift (with respect to the driving signal), as well as the phase lag (delay) of the positioning sensor. When the probe oscillation is set to a few hundreds of Hz, the update of the vertical position occurs at a scale of about ten milliseconds, which imposes some upper limit on the lateral rates that can be employed while achieving accurate vertical positioning. The scheme is given in **Figure 1.13**. Application of a unique scanning trajectory as an Archimedes spiral pattern from the center toward the outside is the key promotion in this technique. The scanning strategy involves the acquisition of substrate topography in an initial trace from the spiral center outward at slow probe translation rate (few μm/s), and then a series of quick retrace scans (back inward toward the spiral origin) using the set of recorded spatial coordinates (x, y, and z) with a sequence of substrate potentials. As a result, this approach allows the acquisition of a series of high-resolution images (typically 1000 pixels μm^2) at rates approaching 4 seconds per frame, while collecting up to 8000 image pixels per second, about 1000 times faster than typical imaging speeds used up to now.

1.1.3.2 Nanoscale characterization of structures and functions

sp^2 carbon materials: sp^2 carbon-based materials, such as graphite, graphene and carbon nanotubes, have widespread applications in electrochemistry associated systems, such as rechargeable batteries, supercapacitor, electrocatalyst. Studying its behavior in electrochemical reactions in nanoscale is significant for understanding the mechanism and kinetics even further improvement of the structures. SECCM allowing locally synchronous topography and electrochemical activity analysis becomes a good candidate for characterization of carbon materials. Step edge of graphite/graphene is a particular focus to study in nanomaterial because the different states impact the density of electronic states (DOS). The highly oriented pyrolytic graphite (HOPG) with five different grades was firstly studied by Unwin and co-workers[136]. It's found that the electrochemical characteristic is independent of surface quality, the basal plane of HOPG shows electron transfer activities. Furthermore, SECCM imaging suggested that pristine basal surface supports fast electron transfer, and the electron transfer not only occur at step edges. However, the history of the HOPG surface strongly influences the electrochemical behavior. Once the surface exposed to air, its conductivity and electrochemical activity deteriorate. This is strongly related to the behavior of the first layer[136–138]. Heterogeneous electron transfer of graphene at edges and different stacking layers was investigated by SECCM as well[139–141]. The current image obtained by $Ru(NH_3)_6^{3+/2+}$ redox couple shows clear enhancement of the electrochemical activities only at the edges. The monolayer graphene has the slowest electron transfer rate, increasing to bilayer graphene and ultrathin graphite, the electron transfer kinetics is much faster. What's more, $Ru(NH_3)_6^{3+/2+}$ shows the strong dependence with the electron transfer kinetics of graphene since its standard potential sits close to the intrinsic Fermi level of graphene and graphite[138].

The electrochemical activities of interconnected single-walled carbon nanotube (SWNT) networks were studied by SECCM[142]. Additionally, the electrochemical activities of individual semiconducting and metallic SWNTs were analyzed and compared[143]. The majority of SWNTs are more or less uniformly active. SWNTs with metallic character are as electrochemically active as metal electrodes. While semiconducting SWNTs shows lower electrochemical activities. Similarly, high activities at sidewalls of SWNTs was proved again with a new SECCM configuration with quad-barrel multifunctional probes[143]. Single-walled carbon nanotubes (SWNTs) actually exhibit exceptional electrocatalytic properties in hydrogen peroxide generation or oxygen reduction reaction (ORR). Therefore, oxygen reduction at pristine, kinked, and oxidized sites on individual carbon nanotubes were compared through SECCM analysis[144]. Results show that kinked or oxidized SWNTs showed higher ORR than pristine SWNTs, proving that the electrocatalytic activities of SWNTs can be enhanced by building defects in architectures (kinks) or through surface modification (sidewall oxidation).

Functional materials: SECCM has shown great promise to map functional materials (such as electrocatalytic and energy storage materials) with high resolution. Synchronously local structural and electrochemical analysis directly reveal the reactive sites promoting further understanding of the mechanism and designing of structures with enhanced activity and/or stability. Simple entities including of nanoparticles (NPs), nanoclusters (NCs), and nanosheets as active catalytic materials have been elucidated with SECCM. For example, electrochemical activity of electrodeposited individual Au NPs toward $[N_2H_5]^+$ oxidation [145] were mapped with a nanopipette with 30 nm opening size. It is shown that the individual Au NPs exhibit comparable activities on average. By contrast, at sub-NP level, single AuNPs appear strongly spatially dependent activity. Single ZIF-derived nanocomposite particles towards OER[146], platinum nanoclusters as active material of ORR[147], hexagonal boron nitride (h-BN)[148] and transition metal dichalcogenide nanosheets[149] for HER were also mapped as exemplar systems. SECCM has also been employed to local activities of polycrystalline materials toward HER[150], CO_2 reduction[151] and $[N_2H_5]^+$ oxidation[134] reactions. Recently, (111)-crystal planes of $Fe_{4.5}Ni_{4.5}S_8$[152] and molybdenum disulfide (MoS_2)[153] as highly active HER catalysts were investigated as well with high resolution SECCM. Relationships between structures and electrocatalytic performance were revealed by nanoscale mapping. This local analysis paves the way for a future in electrochemistry in which the activity of nanostructured electroactive materials can be viewed directly and related to underlying structure through electrochemical movies[54].

Besides above characterizations of catalysts, SECCM has been adapted as a tool for screening the electrochemical (charge/discharge) characteristics of energy storage (battery) materials. Cathodic materials $LiFePO_4$ of lithium-ion batteries was screened via SECCM with resolution of ~ 100 μm by Takahashi and co-works[154]. Single nanopipette filled with LiCl electrolyte solution and an Ag/ AgCl quasi-reference counter electrode (QRCE) was approached to be in contact with $LiFePO_4$ and acetylene black complex composite. Because of the addition of conductor acetylene black, it's found that charging/discharging is not homogenous on the composite electrodes, such processes are largely limited to the particle where the perturbation is made. However, this test was operated within the electrochemical stability window of water because of low operating potential of $LiFePO_4$ (ca. 3.45 V vs. Li/Li^+). This is unusual in the battery devices since most of active materials (such as $LiCoO_2$, $LiNi_{0.3}Mn_{0.3}Co_{0.3}O_2$, $LiNi_{0.5}Mn_{1.5}O_4$, $Li_4Ti_5O_{12}$ *etc.*) is operated within the organic solvents[155]. Hence, 0.1 M $LiClO_4$ in propylene carbonate, ionic liquid 1-ethyl-3-methylimidazolium bis(trifluoromethylsulfonyl)imide as electrolyte solution in Li-ion batteries[156], and gel polymer containing 0.1 M tetrabutylammonium hexafluorophosphate (TBAPF6)/DMSO electrolyte in $Li–O_2$ batteries[157] were studied by SECCM more recently.

1.1.4 Summary and comparison of SECM, SICM and SECCM

After 30 years of developments, SECM becomes a powerful technique in local electrochemical analysis and shows a wide variety of applications (which is briefly discussed in the **Section 1.1.1.4**). Concomitantly, the SECM equipment is well commercialized by some companies such as BioLogic, Heka, Bruker, CH Instruments [158]. This success owes to the expectational spatial resolution and advanced probe miniaturization techniques at micrometer scale. Approaching on the pure conductive or insulting sample surface, the probe could be precisely positioned because of significant alternation of the steady-state current. But when the sample is partially conductive or with heterogeneous reactivities, the approaching of the probe may face problems since the steady-state current does not change clearly. Combination with AFM and shear force techniques, SECM with distance regulation has been further developed, which is also discussed in the **Section 1.1.1.3.** Nowadays, nanomaterials and nano single entities catch more attention. Therefore, local electrochemical analysis techniques must be updated to meet the increasing demands of analysis at nanometer scale. Unfortunately, SECM mapping at the nanometer level is still challenging[159]. The resolution of SECM depends on both electrode size and the distance for substrates. The difficulties in fabricating and characterizing nanoelectrodes increase exponentially with decreasing size. More challenging is it is almost impossible to make a nano-electrode with $R_g < 10$.

Significant investment in imaging, and the availability of a controlled geometry fabrication protocol, which currently are all serial under considering[160]. Additionally, the steady-state current of nanoelectrode starts changing only when the probe is approached in close proximity to the sample surface, this also brings difficulties to position of the probe. Normally, nanometer-sized tips are fragile and easily destroyed by electrostatic effects and vibration[161]. These tips are also easily contaminated, so that extremely pure solutions are essential during the analysis[159]. SICM is based on the pipette filled with electrolyte. Instead of sealing the metal wire in the tip of capillary, the wire is only inserted into pipette as a connector. Hence, the fabrication of the probe is relatively simpler and easier. Because the capillary preparation methods are established, characterization of surface charge and ion fluxes at nanometer scale could be achieved by SICM by monitoring of changes in the nanopipette conductance[162]. Besides, development of hopping mode for feedback systems also greatly improves the resolution of SICM, which permits the investigation of delicate and highly convoluted subcellular structures[118]. The applications of SICM and SECM-SICM are discussed in the **Section 1.1.2.2** with some typical characterizations. For both SECM and SICM, the approach of probes is based on the feedback from bulk solutions. So, the entire samples are bathed with electrolyte. This brings difficulties for long-time analysis on substrates especially for the active materials, which surfaces are easily changed immersing in solutions.

For avoiding this drawback, scanning droplets methods have been proposed. In these techniques, the electrolyte is filled in pipettes and only a small meniscus comes out from the tip of capillary. Thus, applying scanning droplets techniques, only the investigated surface of the samples is wetted and other parts remain virgin[126–128,163]. SECCM is one scanning droplets techniques and becomes more attractive in recent 5 years. SECCM relies on the meniscus from capillaries and locally analyzes the target surfaces in air. It mainly shows the applications of the analysis of nanomaterials using electrocatalysis and energy conversion (discussed in **Section 1.1.3.2**). However, because the aqueous solutions come from the capillary, the spreading of the electrolytes is a problem on the substrates with different roughness and hydrophilicity[164]. Thus, controlling the leakage of the electrolyte is one main challenge of this technique. Leakage of electrolytes is also a key problem and attracts much research attention in energy conversion devices[165–169]. For example, lithium hexafluorophosphate ($LiPF_6$) dissolving in carbonate solvent is a common electrolyte applied in Li-ion battery. Once $LiPF_6$ spreads out from the battery cell, it decomposes in humid air to generate harmful substances. In addition, carbonate organic solvents can cause serious pollution to water, atmosphere and soil, and seriously damage the ecosystem. To solve this issue, gel polymer electrolyte is used to replace the traditional liquid electrolyte. The polymer matrix can track electrolytes with hydrogen bond or surface tension. Gel polymer electrolytes exhibit the solid behavior as controlling the leakage and spreading of the solvent. Apart from, gel polymer electrolytes has the good conductivity like liquid electrolytes[165]. Inspired from this, we have developed a novel technique by carrying out local electrochemical analysis based on the gel polymer electrolyte. This new SPEM named as scanning gel electrochemical microscopy (SGECM)[17], which will be introduced systematically in **Section 1.3**. Since the polymer electrolyte is very important in SGECM, we would like to summarize the polymer electrolytes in the following **Section 1.2**. Preparation based on the electrodeposition, and characterization of electrochemical and mechanical properties will be mainly discussed.

1.2 Gel polymer electrolytes

Since Fenton *et al.* discovered that alkali salts could be dissolved in poly(ethylene oxide) (PEO) in 1973[170], thereby opening up the field of polymer electrolytes in electrochemistry. In recent three decades, polymer electrolytes attract increasing attention because of the blooming researches about secondary batteries[165,171–175], fuel cells[176–178], sensors[179–181], supercapacitors[167,168,182,183], electrochromic displays[12,184,185] and dye-sensitized solar cells[169,186,187]. In comparison with the classical electrolyte, the big advantage of polymer electrolyte is free of leakage electrolyte then reducing the risk of devices. Compactness, reliability, and a large operating potential-window are other advantages it can also provide[188].

Polymer electrolytes can be broadly divided into three categories depending on the different behavior of electrolyte in polymer matrix:

(1) Solid polymer electrolytes (SPEs). The electrolytes are covalently bonded with the polymer matrix. Complexation of functional-groups in polymers with cations alkali metal salts results in the formation of polymer–cation complexes referred to as solid-polymer electrolytes (SPEs), like PEO doped as with Na or K salts[174]. There is no liquid component in SPEs, then the solvent is free of leakage.

(2) microporous (Celgard') type polymers where a liquid electrolyte is held within the pores by capillary action. Relying on the capillary force or the surface tension, the solvent is absorbed in the polymer.

(3) Gel polymer electrolytes (GPEs), where the polymer networks work as inert host with the electrolyte immobilized. The electrolyte is maintained in polymer by the hydrogen bond, then the leakage is inhibited.

In comparison to other two types, GPEs contains the advantages of both solid and liquid elements. The dimensional stability could be maintained but the ionic conductivity is better. Consequently, the GPEs attracts more focus recently.

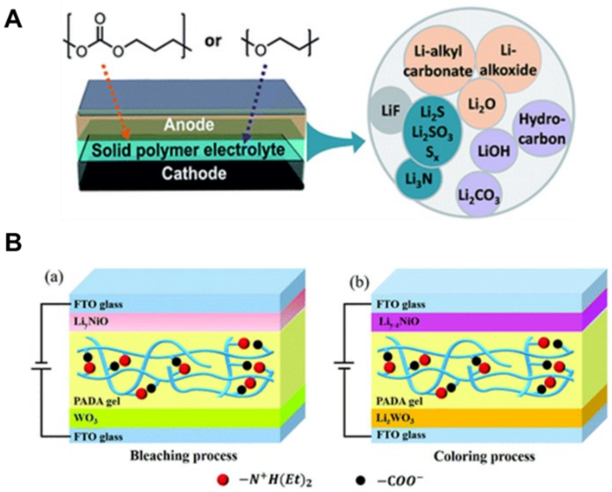

Figure 1.14 Schemes of polymer electrolytes. Solid polymer electrolyte in Li-ion batteries (A) [189]. Gel polymer electrolyte in electrochromic device (B)[190].

1.2.1 Electrodeposition of gel polymer electrolytes

Various methods have been applied for preparation of polymer electrolytes. For example, the solid polymer electrolyte could be prepared by mixing alkali metal salt with a polymer in organic solvents. After evaporation of the solvents, crystallized electrolyte is produced. Typically, poly(ethylene oxide) or poly(propylene oxide) could be doped with Na, K and Li salts[170,191,192] and works as the electrolyte in batteries. Other polymerization approaches are also applied for making solid electrolytes, like free radical polymerization of a lithium salt monomer (LSM) LiPSTFSI for single Li-ion conducting solid polymer electrolytes[174], UV-polymerization of the methacrylate-functionalized poly(ethylene oxide - co - ethylene carbonate) electrolyte[193] for Li-ion batteries.

The GPEs are commonly prepared by gelation of polymer, which is swollen in organic or inorganic solutions. Most gel polymer electrolyte could be physically prepared by heating a mixture of appropriate quantities of a polymer, a plasticizer and a salt to a temperature above the glass-transition temperature of the polymer and cooling to ambient temperatures, such as poly(acrylonitrile), poly(methyl methacrylate), poly(vinyl chloride), poly(vinylidene fluoride), poly(vinylidene fluoride-hexafluoropropylene)[194]. Besides, chemical gelation methods, like addition of crosslinker[195,196], UV-polymerization[197–199] *etc.* were also applied to gel polymer electrolytes preparation. By means of alternative chemical methods, polymer electrolytes can be fabricated by tailoring properties, such as ionic conductivity, stability, mechanical properties, *etc.*

As a synthetic strategy, electro-polymerization offers several advantages over methods. (1), The electro-polymerization is independent of the size and shape of the electrodes. Thus, the deposited polymer electrolyte can cover entire electrode surfaces. (2), The thickness of conformal films could be easily controlled by choosing proper deposition parameters. (3), Material and energy could be saved with high efficiency comparing traditionally chemical-based method. Therefore, in this section, a few samples of electrodeposition of GPEs are listed.

Phenol and derivatives are the first known materials electropolymerized onto substrates forming polymer electrolytes in batteries[200–202]. Phenol monomer or derivatives undergo polymerization reaction due to oxidation into free radicals on the electrode.

The mechanism is shown in **Figure 1.15A**. Examples of electrodeposited polymer are given in **Figure 1.15B**. These insulating films could convert to solid electrolyte films by soaking in a solution like $LiClO_4$-propylene carbonate. Despite the extremely thin nature of the film, the ionic conductivity is extremely low, reaching a maximum of $4 \pm 3 \times 10^{-8}$ S cm^{-1} with a mean film thickness of 40 nm for PSPO.

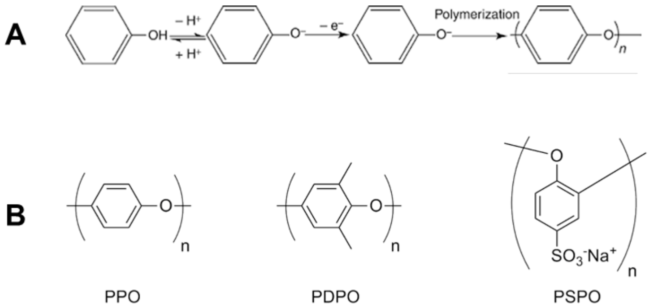

Figure 1.15 Scheme of electropolymerization of phenol (A), examples of PPO-based polymer electrolytes (B).

Copolymer electrolytes based on poly (methyl methacrylate)-polyethylene (PMMA-PEO) could be electropolymerized as the polymer electrode in Li-ion microbattery.
H• radicals can react with the methyl methacrylate monomers carrying out the polymerization then subsequent formation of the PEO-PMMA copolymer, as shown in **Figure 1.16**. In order to achieve this reaction, H• radicals are generated by reduction of H^+ at the potential of –0.66 V (versus saturated calomel electrode). Electrodeposition of PMMA-PEO in self-organized titania nanotubes (TiO_2 nanotubes) have been investigated. This electrolyte promotes the capacity of the microbattery because of high electrode/ electrolyte interface[203–205]. Base on this, complete all-solid-state microbattery was constructed by deposition of polymethyl methacrylate—polyethylene glycol (PMMA-PEG) thin polymer layer as electrolyte and utilization of porous lithium nickel manganese oxide $LiNi_{0.5}Mn_{1.5}O_4$ (LNMO) as cathode and TiO_2 nanotubes as anode[206,207]. Besides, p-sulfonated poly(allyl phenyl ether) (SPAPE) polymer electrolyte could be deposited with carbon nanotubes (CNT) using CV techniques and the microbattery delivers a higher reversible capacity of 750 mAh g^{-1} (276 µAh cm^{-2}).

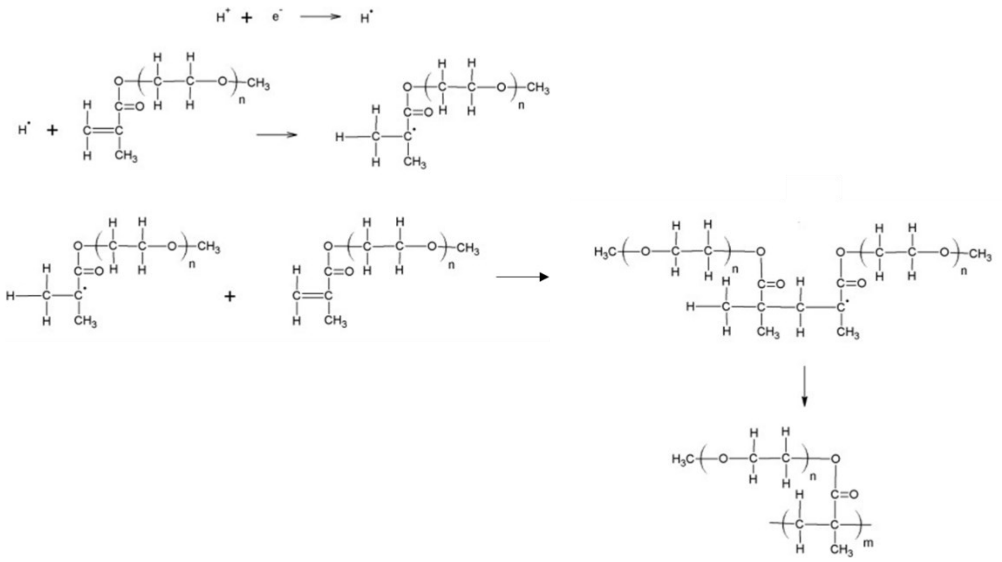

Figure 1.16. Electropolymerization of PEO-PMMA[203].

Because of excellent chemical stability and durability, poly(vinyl alcohol) (PVA) is the most commonly used aqueous GPE polymer. Hence, for increasing the performance of electrolyte, poly(vinyl alcohol) potassium borate (PVAPB) GPEs directly deposited onto the surfaces of active carbon electrodes for electrochemical supercapacitors[208]. Since PVAPB GPEs have good bonding to the active electrode materials, supercapacitors show excellent and stable electrochemical performance (65.9 F g^{-1} at a current density of 0.1 A g^{-1}). As the polymer electrolytes of supercapacitor, poly(o-aminophenol) (PoAP) and poly(m-phenylenediamine) (PmPD) have also been electrodeposited with CNTs[209]. Importantly, the dispersed CNTs provide electron path ways and new reaction sites for continuous electro-polymerization which leads the full coverage of the electrode surface and higher working voltage of the capacitor. The individual coated CNTs in the electrolyte also brought a porous 3D network, which created other interesting application of CO_2 sensor.

Natural polymers are usually used as hosts of electrolytes especially in biomedical applications owing to their excellent biocompatibility. Normally, the prepared polymer electrolyte based on the natural polymers belongs to GPEs, because the numerous hydrophilic bonds are existed in structures and aqueous solvent could be tracked by hydrogen bonds. As one of the most convenient methods, electrodeposition is often applied in fabrication. Chitosan is a cationic polysaccharide and is among the most promising natural biopolymers for biocompatible sensors[210–212]. The chitosan is soluble in aqueous solutions when pH is lower than 6.3. Once the pH is over 6.3, the amino groups in chitosan are deprotonated and ionic repulsions are reduced, allowing associations between chains through attractive interactions. As a result, the dissolved chitosan is physically cross-linked and change to hydrogel. The scheme of chitosan gelation is shown in **Figure 1.17A**. **Electrodeposition is a common method to fabricate the chitosan hydrogel.** The gelation is carried out by locally increasing the pH through generation of OH^- in electrolysis of water[213–216]. Alginate is another nature biocompatible hydrogel and has been widely used to entrap and immobilize biomaterials such as proteins and cells[217–219]. As shown in **Figure 1.18 B**, alginate gels can be fabricated by anodic electrodeposition in which electrochemical acidification (formation of H^+) and the accompanying release of Ca^{2+} in the alginate solution result in deposition of calcium alginate on the electrode surface[220]. The isolation of these polymers limits their application in biosensing. Co-deposition of hydrogels with graphite could increase the conductivity and reproducibility[212,219].

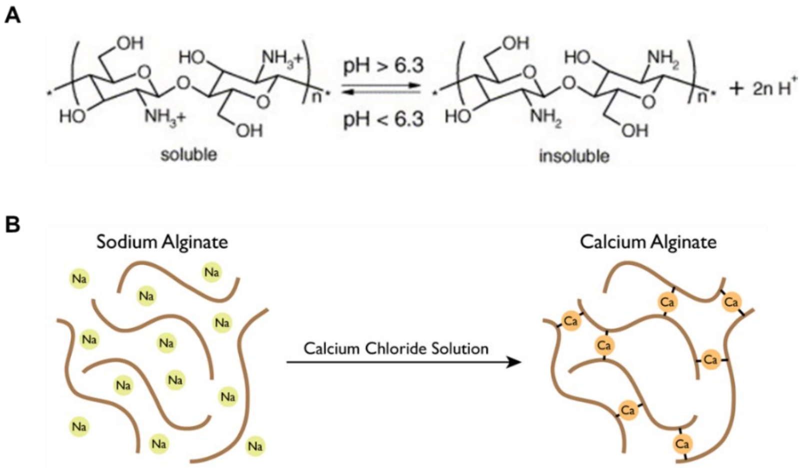

Figure 1.17 Scheme of the gelation of chitosan (A) and alginate-calcium (B).

1.2.2 Mechanical and electrochemical characterization of gel polymer electrolytes

1.2.2.1 Mechanical characterization

Figure 1.18 shows six basic mechanical testing techniques used for polymeric materials:

tension (a) and compression (either unconfined (b) or confined (c)), local indentation with a probe (d) and frequency-based tests such as shear rheometry I or dynamic mechanical analysis (DMA) (f). For both tension and unconfined compression testing, the load–displacement (F–x) data are converted to stress–strain (σ–ε) data using simple geometrical relationships and Young's modulus E and failure strength σ_f[221]. Frequency based sinusoidal testing is commonly carried out using 'black-box' testing systems. A sinusoidal oscillation is applied at a fixed quite small strain but the oscillation frequency is varied. The output is the storage and loss components of the complex modulus as a function of frequency.

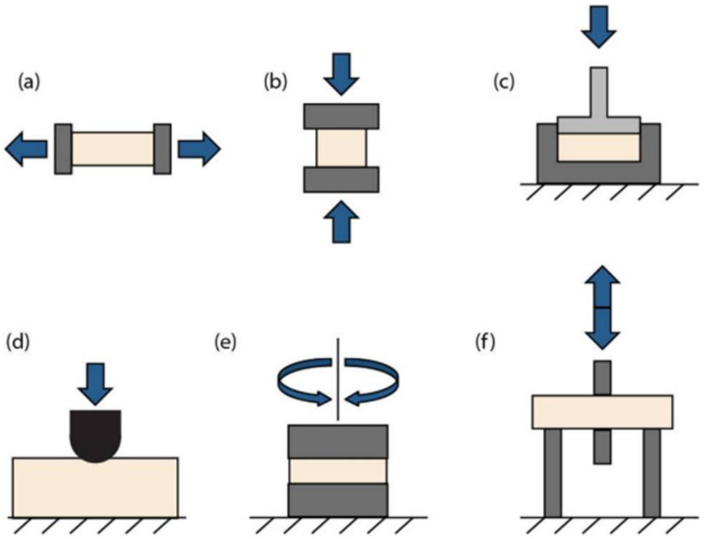

a tension; *b* compression; *c* confined compression; *d* indentation; *e* shear rheometry; *f* dynamic mechanical analysis (DMA), illustrated here for three point bending

Figure 1.18 Six basic mechanical testing techniques for polymeric materials[222].

For gel polymer electrolytes (especially for hydrogels), indentation is usually applied for mechanical characterization because this method has negligible influence on the maintenance of electrolytes in polymers. Nanoindentation or indentation testing at small length scales has been developed for small scales quantitative testing of wide range of materials. Commercial nano-indenters utilize speaker coils or capacitance gages to directly actuate the indenter probe into the sample. AFM is another approach applied for mechanical detection, in which, the tip is actuated indirectly via a calibrated cantilever.

Hertz's contact mechanic theory is used to solve the elastic modulus E of rubber-like polymers. The assumptions employed by Hertz can be summarized as follows[223]:

(1) The strains are small, i.e. $a_c << R$, where a_c is the contact radius and R is the radius of the sphere.

(2) The indented solid is a linear elastic, infinite half space.

(3) The surfaces are frictionless.

(4) Neglecting the deformation of the tip, which can be considered infinitely stiff.

Different equations are used for calculating the modulus considering the geometry of the probe and the thickness of the gel films. Force–indentation and contact radius relationships for the most common geometries are summarized in **Table 1**.

Table 1 Indentation relationships of common indenter shapes.

Model	λ^a	η	a_c (contact radius)
Hertz: sphere of radius *R*	$E^*R^{1/2}$	3/2	$(R\delta)^{1/2}$
Flat cylinder of radius *r*	$3E^*r/2$	1	r
Sharp cone of tip angle 2φ	$3E^*\tan\varphi/(2\pi)$	2	$2\delta \tan\varphi/\pi$
Sharp pyramid of face incline angle $\pi/2-\varphi$, Bilodeau solution[b]	$3(1.4906)E^* \tan\varphi/8$	2	$1.579^{1/2}\delta \tan\varphi/2$
Sharp pyramid, Rico *et al*. Solution[c]	$3E^*\tan\varphi/2^{5/2}$	2	$\delta \tan\varphi/2^{1/2}$
Blunt cone or blunt pyramid of tip angle 2φ, transitioning at radius or half-width b to round tip with radius *R*, with $b = R \cos\varphi$	$F = \frac{3E^*}{2}\left\{a_c - m\frac{{a_c}^2}{\tan\varphi}\left[\frac{\pi}{2} - \arcsin\left(\frac{b}{a_c}\right)\right] - \frac{{a_c}^3}{3R}\right.$ $\left. + ({a_c}^2 - b^2)^{\frac{1}{2}}[m\frac{b}{\tan\varphi} + \frac{{a_c}^2 - b^2}{3R}]\right\}$ $\delta + \frac{a_c}{R}\left[({a_c}^2 - b^2)^{\frac{1}{2}} - a\right] - n\frac{a_c}{\tan\varphi}\left[\frac{\pi}{2} - \arcsin\left(\frac{b}{a_c}\right)\right] = 0$ cone: m = 1/2, n = 1 pyramid: $m = 2^{1/2}$, $n = 2^{3/2}/\pi$		

[a] $E^* = 4E/3(1-v^2)$ where E is Young's modulus and v is Poisson's ratio. [b] Contact radius is actually half the length of one side of the square of contact. [c] Effective contact radius is of a circle with equal contact area.

General force–indentation relationship: $F = \lambda\delta^\eta$. F: force; δ: indentation depth; λ: geometry-dependent elastic constant; η: geometry-dependent exponent.

Because the Hertz contact mechanics model is applied in the characterizations of infinite film (the thickness is ten times larger than the radius of the probe), it will lead to significant errors if the Hertz model is applied to analyze thin films. Dimitriadis *et* *al.* developed a novel model to use corrections for such case[224].

When the indenter is spherical and the film is finite thin,

$$F = \frac{4E}{3(1-\nu^2)} R^{1/2}\delta^{3/2}[1 - \frac{2\alpha_0}{\pi}\chi + \frac{4\alpha_0^2}{\pi^2}\chi^2 - \frac{8}{\pi^3}\left(\alpha_0^3 + \frac{4\pi^2}{15}\beta_0\right)\chi^3 + \frac{16\alpha_0}{\pi^4}\left(\alpha_0^3 + \frac{3\pi^2}{5}\beta_0\right)\chi^4 \quad \textbf{(Equation 1.3)}$$

Where $\chi = \sqrt{R\delta}/h$, and the contacts α_0 and β_0 are functions of the material Poisson's ratio.

When the sample is bonded to the substrate,

$$F = \frac{16\mathrm{E}}{9} R^{\frac{1}{2}}\delta^{\frac{3}{2}}(1 + 1.133\chi + 1.283\chi^2 + 0.769\chi^3 + 0.0975\chi^4) \quad \textbf{(Equation 1.4)}$$

When the sample is soft and viscos, the interaction between probe tip and sample is unavoidable in the indentation. Hence, it is necessary to consider interactive interactions into contact mechanics theory. The JKR (Johnson–Kendall–Roberts) and DMT (Derjaguin–Muller–Toporov) theories are developed based on Hertz contact model.

For the indentation of relatively compliant materials with probes of relatively large radii and strong adhesive forces, the JKR theory is available with the limited error. In contrast, for the conditions of stiff materials, small probe radii, and weak adhesive forces. The DMT theory is applied.

In JKR theory, for a spherical indenter with radius of R[225],

$$\delta = \frac{a^2}{R} - \frac{4}{3}\left(\frac{aF_{ad}}{RE}\right)^{1/2} \quad \textbf{(Equation 1.5)}$$

$$a = [\frac{R}{E}(F_{ad}^{\frac{1}{2}} + (F_{ad} + F)^{\frac{1}{2}})^2]^{1/3} \quad \textbf{(Equation 1.6)}$$

Where F_{ad} is adhesion force (can be also defined as pull-off force), at which the tip and the sample separate when being pulled apart. a is the contact radius between probe tip and the sample. δ is the indentation depth.

For a conical indenter[226],

$$F = 2E[\frac{A}{2R}\left[aA + \frac{a^2-A^2}{2}\left(\frac{\pi}{2} + \arcsin\left(\frac{\left(\frac{a}{A}\right)^2-1}{\left(\frac{a}{A}\right)^2+1}\right)\right)\right] - a\left(\frac{2a\pi\gamma}{E}\right)^{1/2}] \quad \textbf{(Equation 1.7)}$$

$$\delta = \frac{aA}{2R}\left[\frac{\pi}{2} + \arcsin\left(\frac{\left(\frac{a}{A}\right)^2-1}{\left(\frac{a}{A}\right)^2+1}\right)\right] - \left(\frac{2a\pi\gamma}{E}\right)^{1/2} \quad \textbf{(Equation 1.8)}$$

In **Equations 1.7** and **1.8**, $A = Rcot(\alpha)$, where R is half of apex angle. R and α are determined by probes. Elastic modulus E and work of adhesion could be determined from the curve fitting using **Equations 1.7** and **1.8**.

In DMT theory, for the spherical indenter,

$$F + F_{ad} = \frac{4E_s}{3(1-\nu^2)} R^{1/2}\delta^{3/2}$$ (**Equation 1.9**)

Taking other effects such as porous size, viscosity and the evaporation of the immobilized electrolyte, *etc.* into account, the modules for mechanical characterizations are more complicated. The modifications are necessary according to the real cases.

1.2.2.2 Electrochemical characterization

One of the most common and widely recognized techniques for electrochemical characterization is CV. In the case of micro-disk electrode (diameter ≤ 25 μm) which follows semi-spherical diffusion, the voltammogram shows S-shaped curve. The current eventually limits to a constant value that is completely controlled by the diffusion of redox species to the electrode surface, where the electrochemical reaction has decreased its concentration to essentially zero. The steady state current follows the **Equation 1.1**. In the case of a large, planar electrode which follows semi-infinite diffusion, the peak current is expressed by the Randles-Sevcik equation:

$$i_p = 0.4463nFAc(\frac{nF\upsilon D}{RT})^{1/2}$$ (**Equation 1.10**)

For a reversible redox couple, the peak current is proportional to the square root of scan rate ($i \propto \nu^{1/2}$), and the separation of the two peaks ($|E_{pa} - E_{pc}|$) is equal to 59/n mV. Hence, the diffusion coefficient D of electrolyte can be fitted from the plot of i versus $\nu^{1/2}$ [222].

Impedance spectroscopy is a powerful method of analyzing the inner resistance of electrolytes and the diffusion process at electrode interfaces[227–232]. The frequency-dependent impedance Z(ω) of a system is generally determined by applying a voltage perturbation with a small amplitude and detecting the current response (potentiostatic modes). Four elements are usually used to describe the impedance behavior: ohmic resistance, capacitance, constant- phase element (CPE) and Warburg impedance (W). An electric equivalent circuit based above elements is used as a model to describe an electrochemical reaction that takes place at the electrode/electrolyte interface. The values of related elements could be calculated through fitting the plot (Nyquist or Bode plot) obtained from experiments.

It's reported the diffusion coefficient could also be studied by SECM using a micro-disk electrode[233,234]. This approach is based on the difference in the dependence of the transient and steady-state currents on the diffusion current. The chronoamperometric current on a micro disk by diffusion controlling is expressed as follow[234,235]:

$$\frac{i_t}{i} = \left(\frac{\pi^{\frac{1}{2}}}{4}\right) a(Dt)^{-\frac{1}{2}} + 1 \quad \textbf{(Equation 1.11)}$$

i is the steady state current which is given in **Equation 1.1**.

From the **Equations 1.1** and **1.11**, the following relation is obtained:

$$D = (\pi^{\frac{1}{2}} i/(16nFCS))^{\frac{2}{3}} \quad \textbf{(Equation 1.12)}$$

Where, S is the slope of the $\frac{i_t}{i}$ versus $t^{-\frac{1}{2}}$ plot. Thus, D can be determined from S and i_t without knowing the effective tip radius a if C is known.

Alternatively, D can be determined from the chronoamperometric SECM responses for different values of tip displacement, Δd, based on the following approximate analytical relation for a conducting substrate[236]:

$$(Dt_c)^{1/2} = 0.66\,\Delta d + a\ term\ independent\ of\,\Delta d \quad \textbf{(Equation 1.13)}$$

where t_c is the critical time that defines when the SECM undergoes a transition from the microdisk regime to the thin layer cell regime. Above equation can be used to determine D and can be evaluated from a series of plots of the normalized tip current against ${t_c}^{1/2}$ at various Δd, without knowing concentration C and tip radius a.

1.3 Scanning gel electrochemical microscopy (SGECM)

As we discussed in **Section 1.2**, one of the most attractive merits of polymer electrolytes is free of leakage. This is not only significant for increasing the safety of energy storage device, but also helpful in controlling the electrolytes spearing in scanning droplets techniques. SGECM takes this advantage and solves the leakage problem by replacing liquid electrolyte by gel polymer electrolytes[17]. The probe of SGECM, named as “gel probe”, is fabricated by deposition of the gel polymer on a microelectrode with electrolyte immobilized. During the measurements, the gel probe is approached to be in contact with sample surface. Then local electrochemical reactions take place between the gel probe and the sample.

1.3.1 Instrumentation and probe fabrication

SGECM utilizes a gel probe immobilized with electrolyte. By coupling with a piezo motor, the probe can be brought to touch with the sample surface and achieve the local electrochemical analysis. **Figure 1.19A** shows the home-made SGECM setup. The sample is placed on a step motor system (Owis, Staufen, Germany) with movements in *x* and *y* axis. Positioning of gel probe in z axis is more accurately controlled by a piezo in closed-loop mode with position encoder (Physik Instrumente, Karlsruhe, Germany). Electrochemical measurements can be carried out with a PalmSens^3 potentiostat (Palm Instruments BV, Houten, The Netherlands). The current was recorded with a 16-bit data acquisition card (Measurement Computing, Norton, MA). Shear force detection is achieved with two piezoelectric plates mechanically attached to the glass shield of probe. A lock-in amplifier (model 7270 DSP, AMETEK, Inc., Worthington, OH) is used to generate AC signals for actuating one piezoelectric plate and measure the response from another one. All the instruments are controlled with an integrate SGECM program written by VB.net (can be shared upon request). An optical microscope was placed for visualizing the positioning and movement of the gel probe.

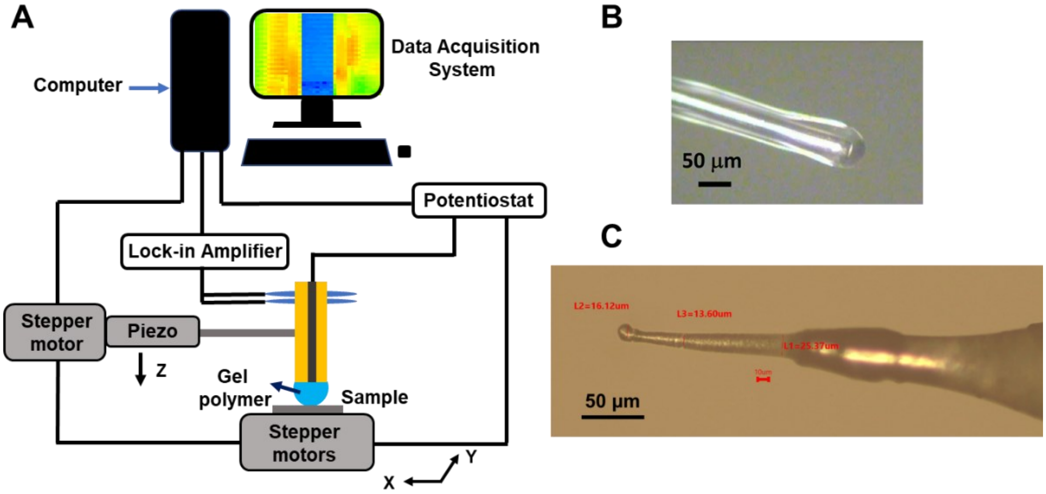

Figure 1.19 Scheme of the SGECM setup (A), gel probe fabricated on a micro-disk electrode (B), gel probe fabricated on an etched metal wire (C).

The gel probe is the heart of SGECM as the electrochemical reactions is taken place on the gel/sample or gel/Pt microelectrode interfaces. Fabrication of the gel probe is based on the electrodeposition of gel polymer on a microelectrode (**Figure 1.19B**). Till now, two gel probes are using in SGECM. One is fabricated by deposition of chitosan on a disk microelectrode. The other is prepared based on deposition of chitosan on an etched metal wire (**Figure 1.19C**). The second one has smaller diameter since the tip of etched wire is very sharp.

1.3.2 Approaching methods – shear force and current feedback

Both shear force and current feedback could be applied to approach the gel probe upon the samples in SECM. The schemes are shown in **Figure 1.20**. For shear force feedback, AC excitation is applied on one plate, and the response signal is recorded from the other one using a lock-in amplifier. An optimized frequency is chosen for obtaining a stable signal, and the approaching of probe stopped when the changed amplitude reaches the threshold (**Figure 1.20 A**). For current feedback, a voltage was applied on the gel probe *versus* the sample during approaching. When the probe is hold in air, the current is zero. Once the probe touches on the sample surface, the current reaches to the set criteria and the approaching is stopped.

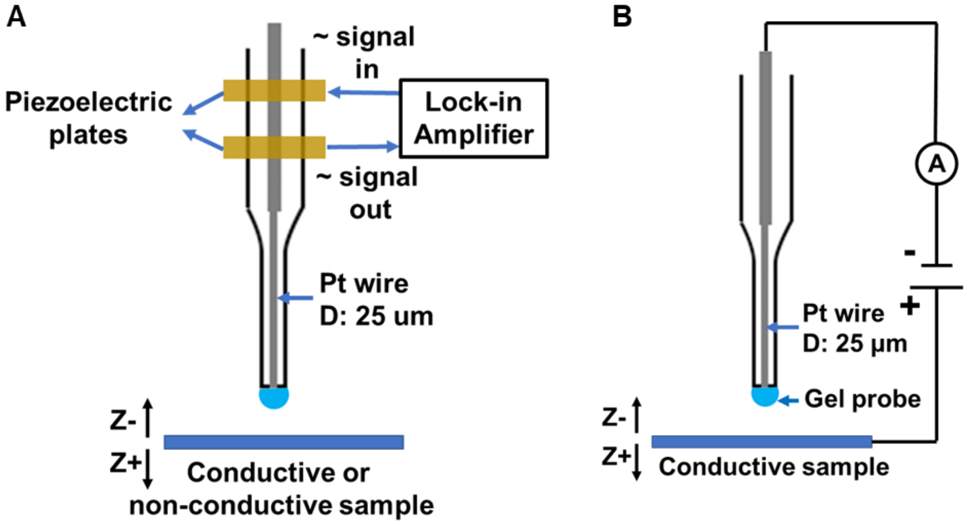

Figure 1.20 Schemes of shear force (A) and current (B) feedback of SGECM.

1.3.3 Amperometric measurements

The amperometric measurements of SECM were shown in the proof of concept work reported by Liang et. al[17]. The gel probe was fabricated based on a Pt micro-disk electrode with the diameter of 25 μm (**Figure 1.19 B**). When the gel probe is in contact with the samples, local chronoamperometry or CV measurements have been carried with the sample as work electrode and Pt microelectrode as reference/counter electrode. The current responds and position were record simultaneously. Consequently, the different materials could be identified by both electrochemical activities and topography. For example, a protective organic coating on Zn-Mg-Al layer with a scratch, and a copper tape on aluminum alloy are differentiated in **Figure 1.20 B and C**.

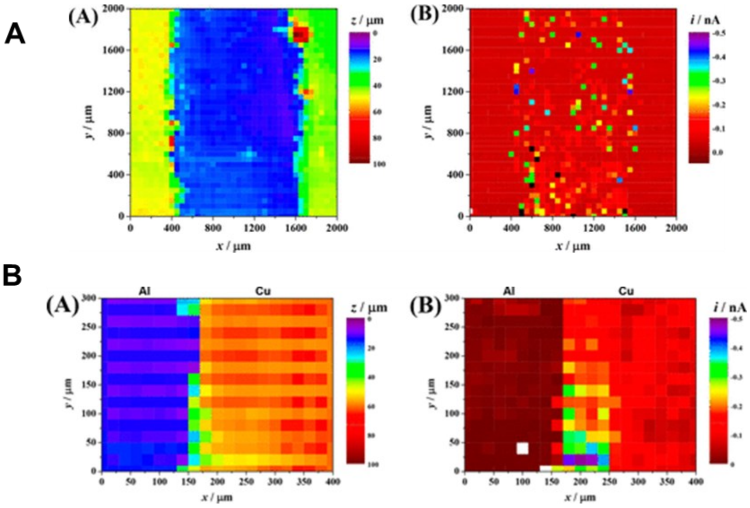

Figure 1.21 Topography and current mapping of scratch on an organic coating with Zn-Mg-Al exposed (E_{surf} = 0.3 V vs. E_{Pt}) (A). Topography and current mapping of copper tape on aluminum alloy (E_{surf} = 0.4 V vs. E_{Pt})

1.3.4 Research aims in this thesis

The target of this thesis is to further develop the SGECM:

Resolution is one of the most important characters of SEPM as it determines the applications of techniques. Thus, with high priority, the lateral physical is quantitatively analyzed in **Chapter II**. Based on the physical resolution, current feedback and shear force feedback in SGECM are compared.

Potentiometric analysis is a very useful method for detecting the local electrochemical activities of materials. So, in **Chapter III**, a novel Ag/AgCl-gel micro-reference electrode is fabricated for achieving the potentiometric measurements of SGECM. The stability and reliability of the probe are evaluated.

Mechanical property is one important aspect affecting the lift time of gel probe. In **Chapter IV**, the gel is improved by cross-linking the hydrogel. The elastic modulus and diffusion coefficient of redox couple in gel probe are quantitatively evaluated.

Specifying the potential applied on samples is more informative for SGECM measurements. For figuring this out, **in Chapter V**, a new gel probe is fabricated base on an integrated probe coupling with a reference electrode. The stability and reliability of the integrated probe are evaluated, the analysis in small droplets is performed. More importantly, the feasibility for further development of the gel probe is discussed.

In **Appendix I**, the optimization of the gel probe fabrication is described.

For cooperation with HEKA, fabrication of gel probe based on their commercialized electrodes is declared in **Appendix II**.

Diffusion coefficient of $Ru(NH_3)_6Cl_3$ in cross-linked chitosan hydrogel on planar electrode is described in **Appendix III** as a supplement of **Chapter IV.**

In **Appendix IV** and **Appendix V**, two mathematic models are built for fitting results tested by the integrated probe of in Fe^{3+} droplet on Fe plate (in **Chapter V**).

Chapter II Scanning gel electrochemical microscopy (SGECM): Lateral physical resolution

2.1 Introduction

Like other SPM techniques, SGECM also has a key issue of resolution, especially the lateral resolution, as it determines the quantification and applications. The lateral resolution has two aspects, scan resolution and physical resolution. The former is determined by the movement of control units (motor or piezo), while the latter refers to the sampling area of a single pixel measurement. With modern instrumentation, the scan resolution can easily reach 0.1 nm, but the physical resolution is usually much lower. Thus, the lateral resolution of SGECM is limited by the physical resolution. Since SGECM is a contact method, the physical resolution is essentially determined by the contact area. Moreover, due to the soft nature of the gel, one may expect that the contact area depends on the force of contact. That is to say, the lateral resolution may be tuned by squeezing or stretching the gel after touching the sample. Therefore, it is highly desired to quantitatively determine the lateral physical resolution of SGECM.

In this chapter, two methods are presented to quantitatively study the lateral physical resolution of SGECM. One method is based on marking single sampling points and measuring their size. This is achieved by locally oxidizing Ag to AgCl with the gel probe. The color change leaves a permanent mark for the contact area, which indicates the lateral physical resolution. Another method is the line scan over a sample with periodic topography and composition. The profile of the sample is measured by the gel probe and a commercial profilometer (as reference). By comparing the results, the lateral physical resolution is analyzed. Apart from the shear force feedback used in previous work[17], current feedback is also used for approaching the gel probe to conductive samples. The lateral resolution of the two feedback protocols is compared.

It is seen that current feedback is more sensitive to gel-sample contact than shear force feedback, but the latter is more versatile regardless of the sample conductivity.

2.2 Experimental section

2.2.1 Gel probe preparation

The gel probes were fabricated by electrodepositing chitosan hydrogel on Pt micro-disk. A 25 μm diameter Pt wire is sealed into a pulled glass capillary by epoxy resin. The outer diameter of the original capillary is 1.5 mm, and after pulling it has a diameter of ca. 50 μm at the tip, which is about two times as that of the Pt wire ($R_g \approx 2$). These electrodes were used for electrodepositing chitosan in a three-electrode system, with a chlorinated Ag wire as quasi-reference electrode (QRE) and a Pt wire as counter electrode. The deposition conditions were carefully optimized to control the shape of the gel deposit. The related experiments are showed in **Appendix I**. Here, the chitosan solution was prepared by dissolving 0.8 wt.% chitosan (medium molecular weight, Aldrich) in 1:1 (*vol.* ratio) glycerol/deionized water containing 0.125 mol/L NaCl. The pH of solution was adjusted to 5.5. Typically, the electrodeposition was carried out by applying a constant potential of −1.1 V (*vs.* Ag/AgCl QRE) for 420 s with the deposition current monitored. The deposition curve and the image of the fabricated gel probe is shown in **Figure 2.1**.

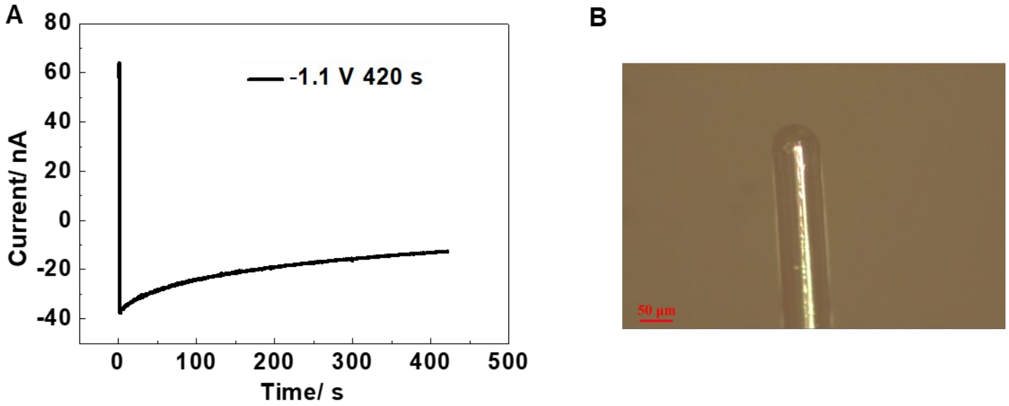

Figure 2.1 Chitosan deposition curve on Pt micro-disk electrode (A) and the image of gel probe (B).

2.2.2 Approaching and retracting the gel probes

The gel probes were initially positioned in air and not in contact with the sample, as verified by optical microscope. They were approached to the sample with the speed of *ca.* 17 µm/s while measuring the current and/or shear force signals, and the contact was sensed by the current or shear force reaching a pre-set threshold. This constituted a closed-loop feedback. For current feedback, the probe stopped when the current reached ±0.1 nA. For shear force feedback, the approaching stopped when the amplitude of signal changed by ±0.2%. After the gel probe touched the sample, it was immediately triggered to retract away from the sample with the speed of *ca.* 68 µm/s. The current and shear force signals were continuously recorded until the probe moved back to the initial position. In this thesis, the contact position (sensed by either current or shear force feedback) is normalized as $z = 0$. Positive z represents further approaching the gel probe (squeezing the gel), and negative z represents retracting the probe away from the sample (stretching the gel).

2.2.3 AgCl deposition on Ag substrate

Ag foil (99.9%, ChemPUR, Karlsruhe, Germany) was cut to $10 \times 10 \times 0.125$ mm^3, polished with Alumina paste (0.05 µm), cleaned with acetone by sonication and dried in air before being used as substrate for deposition. The gel probe was approached to be in contact with the Ag foil with current or shear force feedback, and then the probe was purposely further approached or retracted by a given distance (approaching speed was *ca.* 17 µm/s). For deposition, a voltage of 1.2 V was applied on Ag foil *versus* the gel probe for 300 s, allowing Ag to be chlorinated forming AgCl. After deposition at one point, the probe was withdrawn rapidly (at maximum speed allowed by the piezo) to detach from the sample and then laterally moved by 150 µm for the next point. The deposited AgCl spots were examined by optical microscope (Nikon, Japan) and also characterized by scanning electron microscopy (SEM) equipped with energy dispersive X-ray spectroscopy (EDS) (Hitachi FEG S4800).

2.2.4 Line scan of periodically shaped samples

Two typical samples with periodic shape and composition were analyzed by SGECM with current and shear force feedback. Sample 1 was a TEM grid of Cu (50 mesh, bar width of *ca.* 80 μm, hole size of *ca.* 450 μm, Electron Microscopy China) stick on a flat Fe plate. Sample 2 was commercial Au interdigitated electrodes (DropSens, bands/gaps of 200 μm) with one electrode plated with Cu. The electroplating was carried out at – 0.8 mA for 1 h in a commercial solution (High speed bright copper electroplating solution, 900569-500ML, Aldrich). This yielded a sample with three different materials: Cu (height of *ca.* 10 μm, conductive), ceramic (flat, insulating) and Au (flat, conductive). It was used for demonstrating the versatility of shear force feedback SGECM. The profile of both samples was analyzed on a commercial profilometer (Brüker Dektak XT) by a cone-shape probe of 2 μm radius at a scan resolution of 0.05 μm.

For SGECM line scan, the gel probe was approached to touch the sample by current or shear force feedback, then was positioned to the desired z position and kept for 3 s. This allowed a stable steady state current to be recorded. Afterwards, the probe was withdrawn to detach from the sample and then laterally moved for 2 μm for the next measuring point. Scanning speed of the probe was same with the experiments of AgCl deposition. Sample 1 was measured at 0.5 V (E_{sample} *vs.* E_{probe}), and Sample 2 was measured at 1 V (E_{sample} *vs.* E_{probe}).

2.3 Results and discussion

The first step of any scanning probe technique is approaching the probe close to the sample. In SGECM, the gel probe should be in contact with the sample surface for measuring local electrochemistry, and the contact position would reveal the topography of the sample. Considering its soft nature, the gel probe can be further pressed or stretched after touching the sample. This may affect the contact area thus influence the lateral physical resolution of the measurements. Therefore, it is essential to find sensitive detection of contact by studying the approaching/retracting behaviour of the gel probe.

2.3.1 Approach and retract the gel probe

The gel probes were first approached to the sample with shear force feedback. **Figure 2.2 A** shows that the amplitude of signal is almost constant when the gel probe is far away from the sample, thus it is normalized to 100%. The signal starts to change when the probe gets close or in contact with the sample. We arbitrarily selected ±0.2% as the threshold for stopping the approaching, as this is sufficient to distinguish from the noise. Afterwards, the gel probe is immediately retracted from the sample. It is seen that the signal further increases upon retraction, but it decreases after *ca.* –5 μm. At *ca.* –20 μm the signal recovers almost to the initial value before touching (100%). This phenomenon is qualitatively reproducible (**Figure 2.2 B and C**), yet the exact values of change are different perhaps because of the complexity of shear force signals (as discussed in **Introduction 1.1.1.3**). Overall, the signal change perhaps originates from pressing and stretching of the gel during the approaching and retraction.

When approaching the gel probe to a conductive sample, current could also be monitored by applying a voltage between them. **Figure 2.3** compares the variation of current (measured at 1.2 V (E_{sample} *vs.* E_{probe})) and shear force signals when approaching the gel probe. It is clearly seen that the current sharply increases from 0 (with noise) to *ca.* 3.3 nA at one position, which indicates that the gel probe touches the sample. This position is normalized to $z = 0$. At the same time, the shear force signal also starts to change, which can be explained by the contact. Nevertheless, the probe is further approached for *ca.* 4 μm until the shear force amplitude reaches the threshold (±0.2%) for stopping the approaching. The results indicate that current feedback is much more sensitive to gel-sample contact than shear force feedback. It should be noted that the sensitivity of shear force feedback could be improved by reducing the threshold, but it would also increase the risk of stopping the approaching before touching ("fake contact") due to the noise and drift of the signal[39].

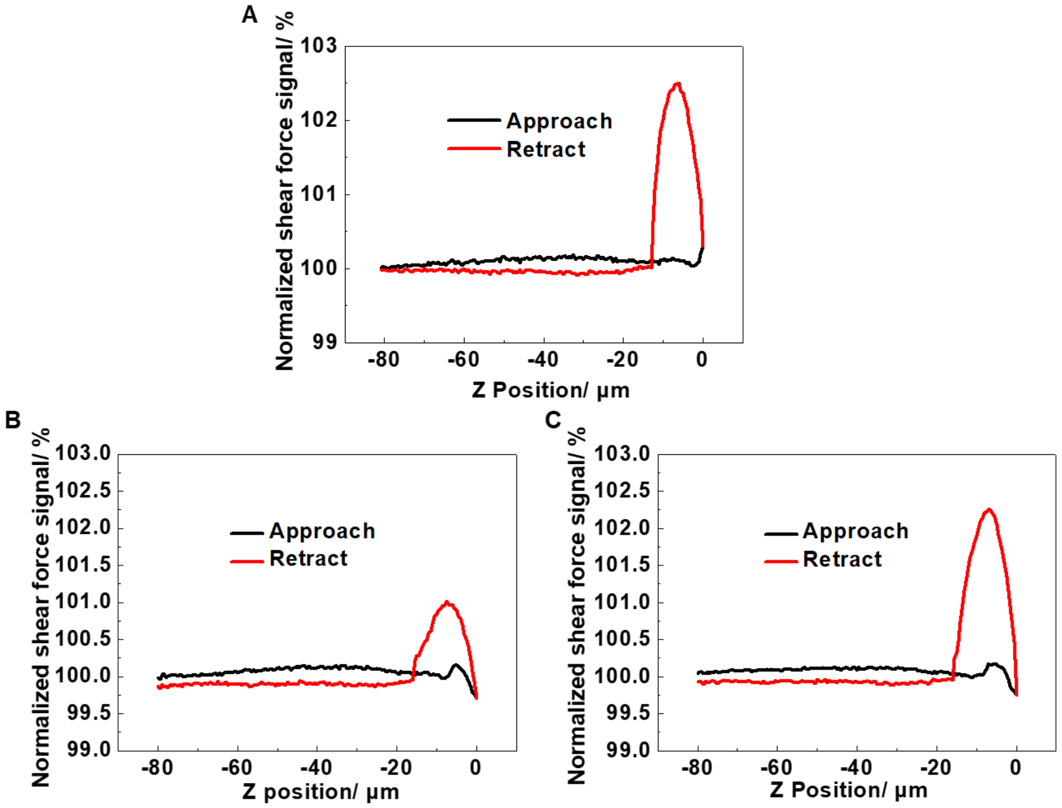

Figure 2.2 Approach-retract curves of shear force feedback with the shear force threshold of ±0.2%.

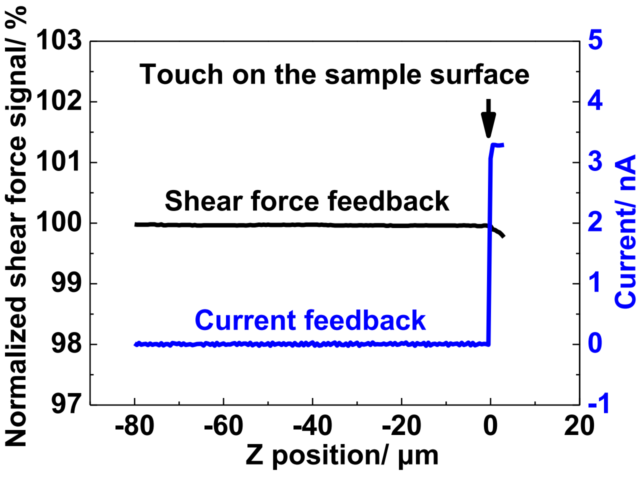

Figure 2.3 Approach curves of shear force and current feedback.

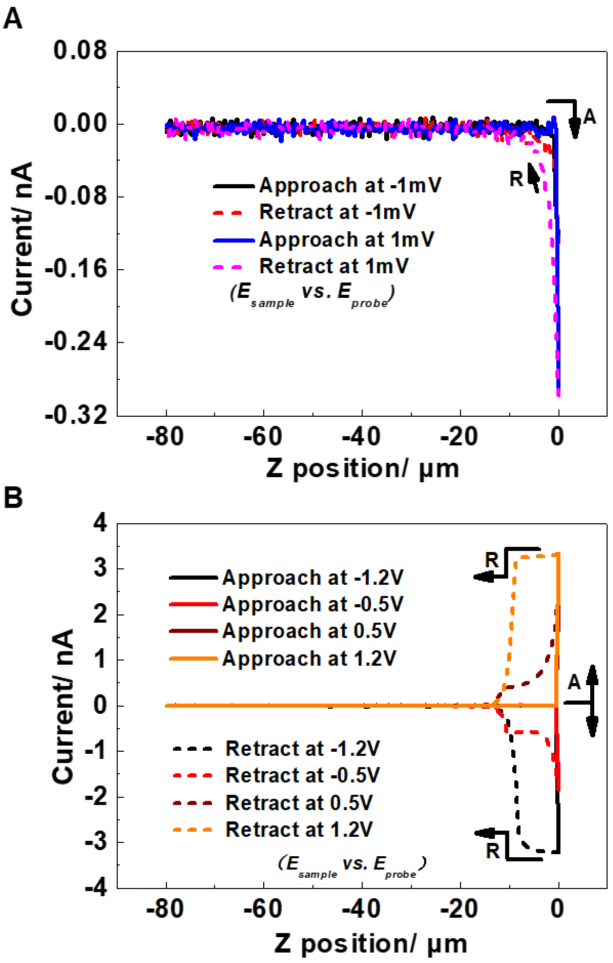

Figure 2.4 (A)Approach and retract curves of current feedback at ±1 mV (E_{sample} *vs.* E_{probe}); (B) Approach and retract curves of current feedback at ±1.2 V and ±0.5 V (E_{sample} *vs.* E_{probe}).

The sharp spike of current in **Figure 2.3** is technically ideal for constructing a feedback loop. Therefore, we further studied the approaching and retracting behaviour of gel probes by current feedback under a constant applied voltage. In principle, when the gel probe touches a conductive sample, any potential that is different from the open circuit potential (OCP) of the two-electrode system (E_{sample} *vs.* E_{probe}) would give a current response. Therefore, even the OCP is unknown, the gel probe could still approach with an arbitrarily selected voltage. For example, current spikes are detected upon touching the gel probe with an Ag plate in a wide range of the applied voltage (**Figure 2.4**). As the voltage increases, the current upon contact (the first point recorded with absolute value above a threshold that differentiates the noise) also increases, but even applying ±1 mV is sufficient for detecting the contact. Considering the time interval of data acquisition (*ca.* 17 ms), the current upon contact mainly reflects the non-Faradaic behaviour of the system. Therefore, the polarity of current depends on the open circuit potential of the Pt/gel/Ag system, which is not zero. This explains the same polarity of current response for ±1 mV. Moreover, the probes are immediately retracted from the sample after touching, and the current is monitored with the same voltage as approaching. Qualitatively, it is seen that the gel probe remains in contact with the sample after retracting for a certain distance. This can be explained by the stretching of the gel upon retraction that compensates its adhesion with the sample surface. Once the stretching force exceeds the adhesion, the gel detaches from the sample and the current response returns to zero (with noise). The detail current variation depends on the applied voltage. For example, at ±1.2 V (E_{sample} *vs.* E_{probe}) the current is almost unchanged up to *ca.* –10 μm, and then decreases upon further retraction. At *ca.* –16 μm, the current decreases to zero (with noise). The approach/retract curves in current feedback (**Figure 2.5A**), and the approach/press/retract curves in shear force feedback (**Figure 2.5B**) are highly reproducible after a few cycles, confirming that the gel probe undergoes elastic deformation. In **Figure 2.5A**, the gel remains in contact with the sample by retraction up to *ca.* –16 μm. While, in **Figure 2.5B,** pressing causes more deformation of the gel, so it is detached from the sample surface with longer starch length (*ca.* –31 μm). It should be noted that the initial several approach-retract cycles may remove the loosely absorbed solvent in the gel. This step is practically important for quantitative measurements. At ± 0.5 V, the current significantly decreases before reaching a plateau. Interestingly, after ca. −11 μm the current decreases again until returning zero at ca. −16 μm. At ± 1 mV, the current gradually decreases until merging in the noise at around −10 μm. The difference in detaching position might indicate that the applied voltage affects the adhesion of the gel with the sample. Quantitative analysis of the retracting current is very complicated, because it is a two-electrode system affected by both non-Faradaic and Faradaic processes, as well as the change in the electrical resistance of the gel due to stretching. This will be further explored in future.

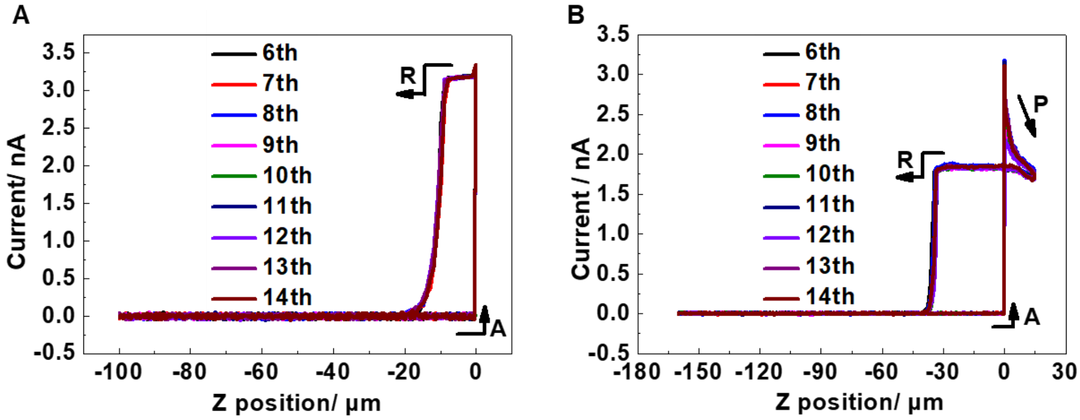

Figure 2.5 Multiple approach/retract (A) and approach/press/retract (B) curves at voltage of 1.2 V (E_{sample} *vs.* E_{probe}) in current feedback.

Approach and retract curves are very informative. First, it helps setting up a feedback loop with appropriate threshold for detecting the contact between the gel probe and the sample. Moreover, it shows that the gel probe can be elastically pressed or stretched in a certain range while keeping contact with the sample. This soft contact allows electrochemical measurements to be carried out at different *z*, which will be explored in the following sections. For conductive samples, current feedback is more sensitive to touching than shear force feedback, thus it is more favourable. It can be technically carried out at almost any voltage, providing high flexibility for choosing the voltage according to the need. Nevertheless, shear force feedback is more versatile, which is still useful for the samples with unknown conductivity, such as partially non-conductive samples.

2.3.2 Determination of lateral physical resolution by AgCl deposition

The soft contact as seen from the approach-retract curves may affect the contact area where electrochemical reactions occur, and this may change the lateral physical resolution of SGECM. The most straightforward way to analyze such resolution is permanently marking single sampling points (pixels). This is achieved by locally oxidizing Ag in the presence of Cl^- forming AgCl, as illustrated in **Figure 2.6**. The gel probe is approached to an Ag plate with either current or shear force feedback, and then positioned at different *z*. A voltage is then applied to locally oxidize Ag in the contact area. This leaves spots with permanent colour change on the sample. **Figure 2.7A** shows the SEM image of a typical spot. It is clearly seen that deposition is formed. The deposit is analyzed by EDX and it clearly shows a Cl peak (**Figure 2.7B**). The results confirm the deposition of AgCl by oxidizing the Ag plate, thus the physical resolution of SGECM can be derived from the size of the spots.

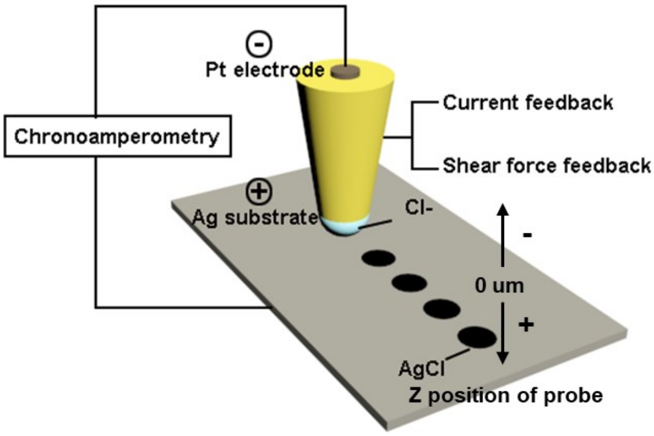

Figure 2.6 Scheme of AgCl deposition by current and shear force feedback in SGECM.

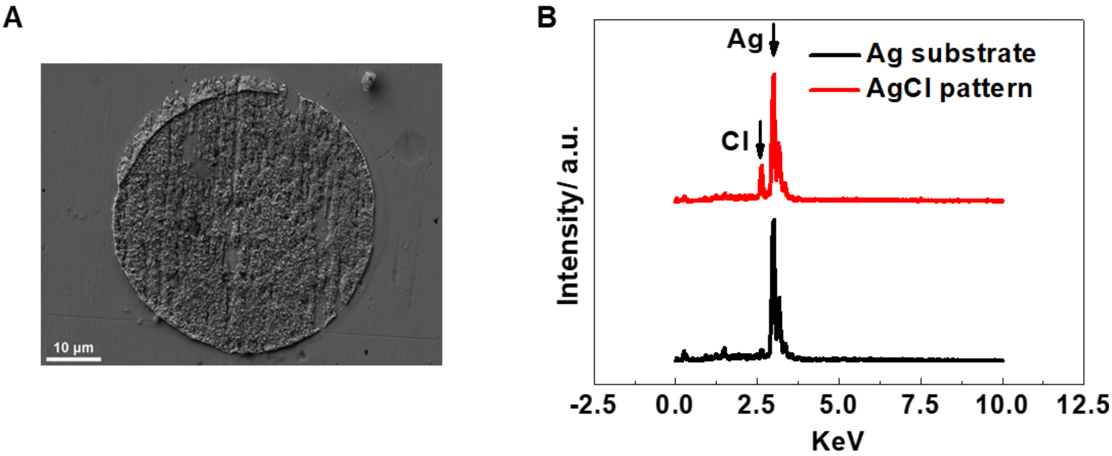

Figure 2.7 SEM image (A) and EDX (B) of a typical AgCl spot deposited at touching position ($z = 0$ μm) of current feedback.

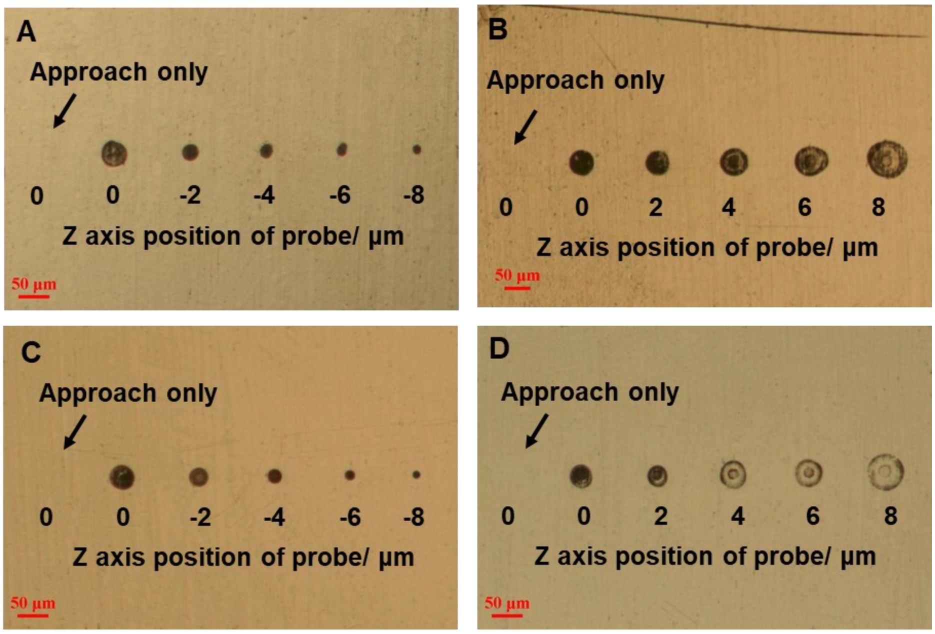

Figure 2.8 AgCl depositions on Ag substrate by current feedback (E_{sample} *vs.* E_{probe} = 1.2 V) with the gel probe positioned at negative (A)(C), positive (B)(D) *z* after touching the sample.

Figure 2.8 shows the image of AgCl spots deposited at 1.2 V (E_{sample} *vs.* E_{probe}) for 300 s. The spot deposited at $z = 0$ has diameter of *ca.* 50 μm, which is about two times the diameter of the Pt microelectrode and is close to the diameter of the glass shield. At negative *z* (pulling the gel probe after touching), it is clearly seen that the size of spots decreases (**Figure 2.8A**). In contrary, at positive *z* (pressing the gel probe after touching) the size of spots slightly increases (**Figure 2.8B**). The size of spots reflects the area of contact. Considering that the stiffness of the gel is constant for the same probe, the area of contact is proportional to the total force of interaction at the gel/sample interface which is the vector sum of the squeezing/stretching of the gel and the gel/sample adhesion. At negative *z*, the gel is stretched to counterbalance the adhesion, decreasing the total force, while at positive *z* the gel is squeezed adding the total force. This explains the trend as illustrated in **Figure 2.9**. The results indicate that the lateral physical resolution of SGECM can be tuned in the range of 14 to 78 μm by pulling or pressing the same gel probe. This is an important feature of SGECM, which originates from the soft contact between the gel probe and the sample surface. This trend of flexible resolution is reproducible with different gel probes, even though the exact values slightly differ (**Figure 2.8 C and Figure 2.8 D**). It should be noted that the spots deposited at intensive pressing of the gel probe ($z > 4$ µm) are not homogeneous. Apart from the outer rings that reflect the area of contact, round shape depositions with diameter of around 25 µm are seen in the center of the spots. This can be explained by the current distribution, which is more localized when the microelectrode is closer to the sample, similar as direct mode SECM[237, 238].

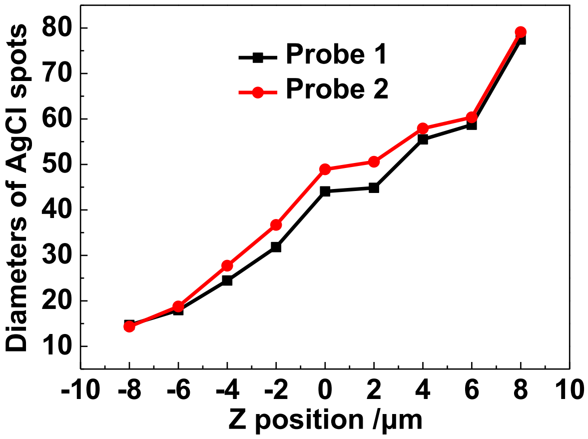

Figure 2.9 Size of AgCl spots as a function of *z* in current feedback.

The flexible resolution is also seen when approaching the gel probe by shear force feedback. Considering that the gel is already pressed when the approaching stops (**Figure 2.3**), only pulling (negative *z*) is tested. **Figure 2.10** shows that the deposition at touching position has diameter of *ca.* 63 µm. This is close to the diameter of the spot deposited at $z = 4$ µm in current feedback (**Figure 2.9**), confirming that the gel probe is indeed pressed. The deposition is reproducible with the same probe, which is also proved in **Figure 2.10A and Figure 2.10B**. Moreover, the difference in touching position is consistent with that seen from approach curves in **Figure 2.3**. By pulling the gel probe, the size of the spot also decreases, which agrees with the trend observed with current feedback. This is also reproduced with another gel probe (**Figure 2.11**). The results confirm that the contact area between the gel probe and the sample depends on the pressing/pulling of the gel probe, thus the lateral physical resolution of SGECM is tuneable in the range of tens of microns with the same gel probe. In addition, it further proves that current feedback is more sensitive than shear force feedback for detecting the contact of gel probe on conductive surfaces.

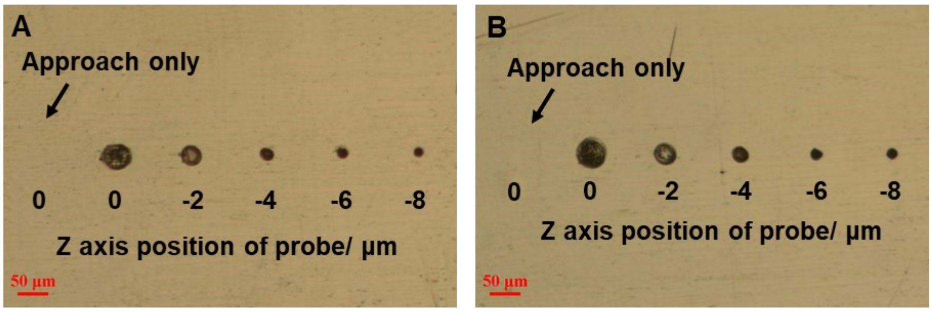

Figure 2.10 AgCl depositions on Ag substrate by shear force feedback, with the gel probe positioned at different negative *z* after touching the sample. (A) and (B) are the repeat experiments with the same probe.

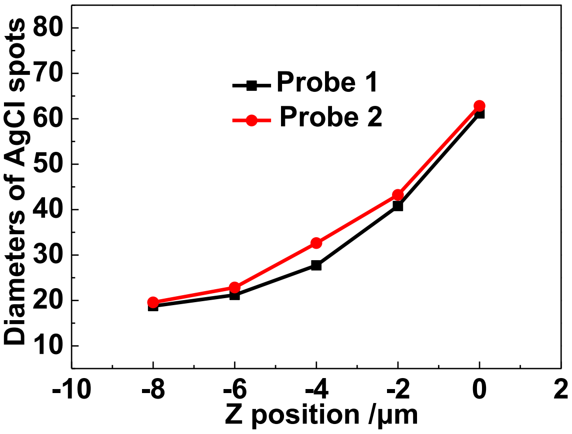

Figure 2.11 Size of AgCl spots as a function of *z* in shear force feedback.

2.3.3 Determination of lateral physical resolution by line scan of periodically shaped samples

Besides marking single pixels on the Ag plate, another approach for determining lateral physical resolution is to scan periodically shaped samples. Here, a Cu TEM grid stick on a flat Fe plate is taken as a reference sample, as demonstrated in **Figure 2.12**. The topography of the sample can be retrieved from the touching position coordinates in line scan of SGECM, and the lateral physical resolution is analyzed by comparing with the results from commercial profilometry measured at the same area.

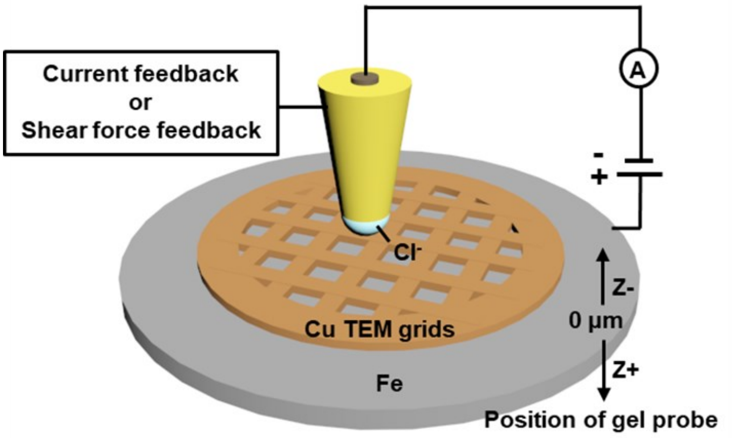

Figure 2.12 Scheme of line scan on Cu TEM grid/Fe plate by current and shear force feedback SGECM.

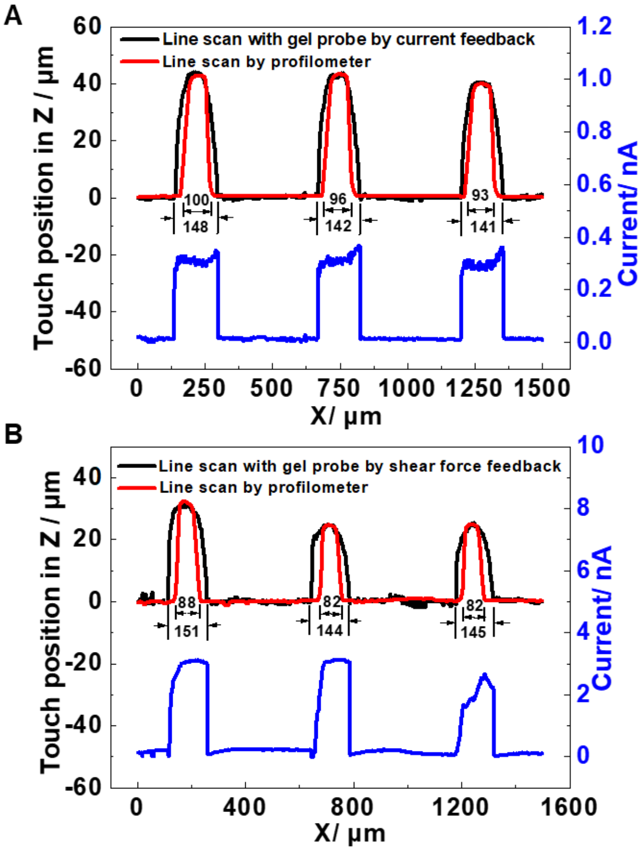

Figure 2.13 Line scan of profile and steady state current by current (B) and shear force (C) feedback. The data were recorded at touching position with E_{sample} *vs.* E_{probe} = 0.5 V after waiting for 3 s.

Figure 2.13A shows the profile of Cu grid bars measured from line scan of current feedback SGECM (black curve) and profilometry (red curve). At the edges of the bars, the SGECM profile shows arc and the profilometry shows trapezoid shape. This is because the gel probe has quasi-hemispherical shape, while the profilometry uses cone shape probes. The height of the bars is almost the same for both curves, indicating that SGECM is reliable for topography measurements in *z* axis. Nevertheless, it should be noted that the profile from SGECM shows "wider" bars than profilometry. This blurring effect is due to the larger diameter of the gel probe as compared with the profilometer probe (d = 4 μm). The difference in the measured width indicates that the lateral physical resolution of SGECM is *ca.* 46-48 μm, with the gel probe touching the sample by current feedback (**Table 2.1**). The value is similar as that determined from AgCl deposition at $z = 0$. The same probe is also used for line scan SGECM with shear force feedback (**Figure 2.13B**). The height of the bars can also be reliably measured, but the width appears even larger than in current feedback SGECM, suggesting that the lateral physical resolution is poorer. The calculated lateral physical resolution is *ca.* 62.5 μm (**Table 2.1**). This confirms that the gel probe is already pressed at touching position of shear force feedback, which agrees with the trend observed in approach curves (**Figure 2.3**) and AgCl depositions (**Figures 2.9 and 2.11**). As compared with SECCM, the resolution is almost one order of magnitude inferior, but it is tuneable by pressing or stretching the same gel probe[239].

Apart from the touching coordinates that reflect the topography, the steady state current under a constant voltage is also recorded when the gel probe touches the sample. This indicates the reactivity of the sample. From **Figure 2.13**, it is clearly seen that the current measured on Cu grid is much higher than that on the Fe substrate in both current and shear force feedback. The redox behaviour of Cu/Cu^{2+} can be seen from the peaks in CV, while Fe is more inert perhaps due to the passivation (**Figure 2.14**). As a result, the current in SGECM may differentiate the two metals based on their different reactivity. It is interesting to see that the current measured with shear force feedback is almost 10 times higher than that measured with current feedback. Considering that the contact area in shear force feedback is only less than 2 times higher than that in current feedback, there should be other factors causing this significant difference. One possibility is that the distance between the Pt microelectrode and the sample is reduced in shear force feedback due to the pressing of the gel. This may facilitate the redox of Cu, like in the sample generation-tip collection mode SECM[240,87].

Table 2.1 Physical resolution of SGECM by current and shear force feedback. D_b is the difference in the measured width of the same bar. Unit is μm.

Feedback	D_b1	D_b2	D_b3	R_{SGECM}
Current	48	46	48	47 ± 1
Shear force	63	62	63	62.5 ± 0.5

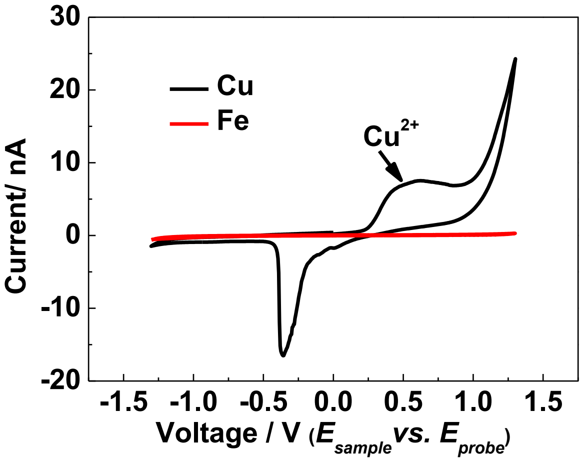

Figure 2.14 CV of the gel probe on Cu TEM grid and Fe plate.

Since the topography is measured based on the touching position in SGECM, it is obviously only possible to determine the physical resolution at $z = 0$ from the profile. Nevertheless, the current response in line scan allows examining the flexible resolution feature of SGECM by pulling or pressing the gel probe. **Figure 2.15** compares the topography with steady state current at different z measured at the edge of a Cu grid bar using current feedback. At $z = 0$ (**Figure 2.15A**), the current step fits well with the profile step in lateral position, indicating that the two measurements have the same physical resolution which is trivial to understand. By pulling the probe to $z = -2$ μm (**Figure 2.15B**), the current decreases before the touching position when scanning from the Cu bar to the Fe substrate. This suggests that pulling the gel probe would reduce the contact area thus increase the physical resolution of the measurement. In contrary, when pressing the probe to $z = 4$ μm (**Figure 2.15C**), high current is still measured even when the probe laterally leaves the Cu bar at touching position. This is likely due to the pressing of the probe that increases the contact area and re-includes the Cu part. The pressing of the probe also yields an increase in the absolute value of current on Cu, which has been discussed in the previous paragraph. Similar trends are also observed with shear force feedback (**Figure 2.16**). The results provide another proof for the flexible resolution feature of SGECM.

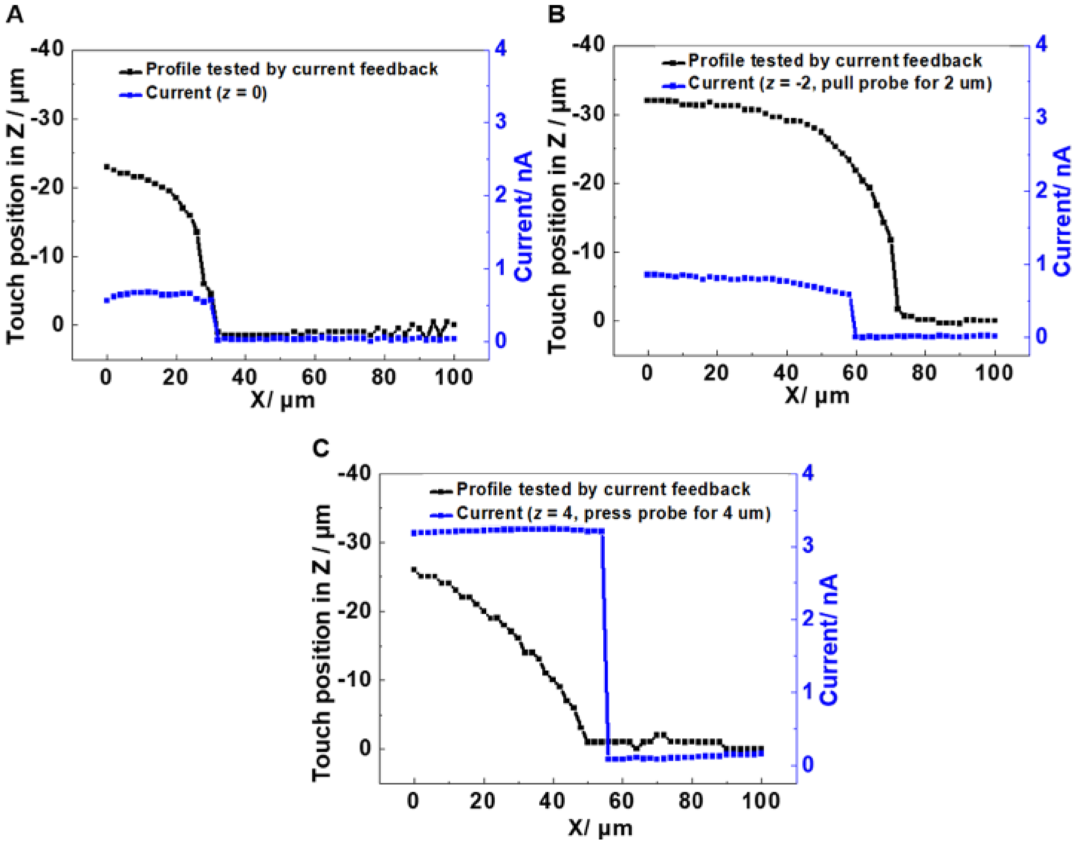

Figure 2.15 Line scan of profile and steady state current on Cu TEM grid/Fe plate by current feedback SGECM. The current is recorded at $z = 0$ (A), –2 (B) and 4 (C) μm at E_{sample} *vs.* $E_{probe} = 0.5$ V after waiting for 3 s.

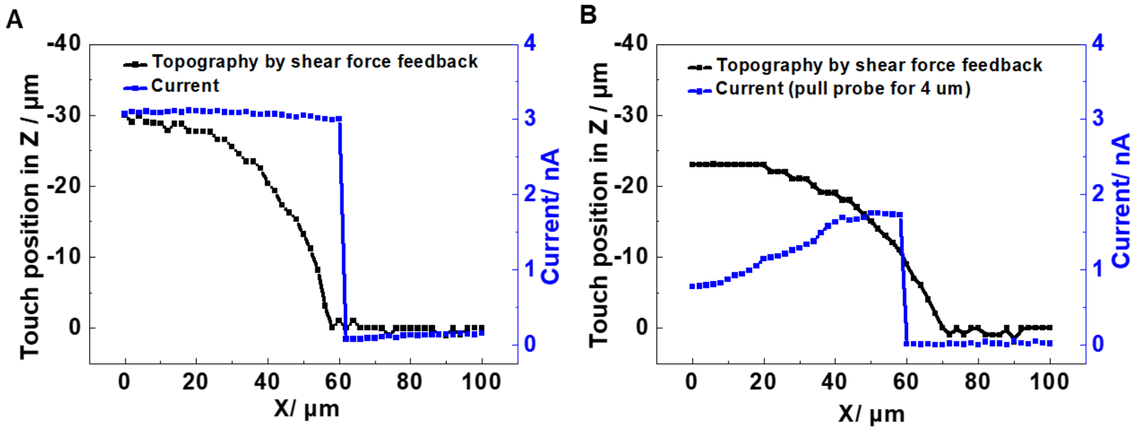

Figure 2.16 Line scan of profile and steady state current on Cu TEM grid/Fe plate by shear force feedback SGECM. The current is recorded at z = 0 (A) and –4 (B) μm at Esample vs. Eprobe = 0.5 V after waiting for 3 s.

From the results above, it is clear that the current feedback is more sensitive to touching than shear force feedback, because the gel is already pressed at the touching position in the latter. Therefore, it is more favourable to use current feedback for approaching the gel probe to the sample. Nevertheless, current feedback requires the whole sample to be conductive, while shear force feedback does not have this restriction. For example, **Figure 2.17** illustrates Au interdigitated electrodes with one electrode plated with Cu. In this case, the sample consists of Au and Cu that are both conductive, as well as insulating ceramic between them. Thus, it can only be measured with shear force feedback SGECM. **Figure 2.18** shows the profile and steady state current of a line scan. Since the thickness of Au interdigitated electrodes is negligible, only Cu plating bars of *ca.* 10 μm height are visible in the profile. This is in agreement with the profilometry (**Figure 2.19**). Meanwhile, current signals could reveal both Cu and Au, as well as the insulating ceramic. As shown in **Figure 2.20**, CV was carried out when the gel probe touches different parts of modified interdigitated electrodes. It is seen that Cu is significantly oxidized at E_{sample} *vs.* E_{probe} = 1 V, while Au has much lower current response at the same potential. This can be explained by its higher electrochemical activity towards oxidation. As expected, current is almost 0 (with noise) when the gel probe touches the ceramic part of the sample. This example demonstrates the versatility of shear force feedback SGECM, which can be used in measuring any sample with unknown conductivity.

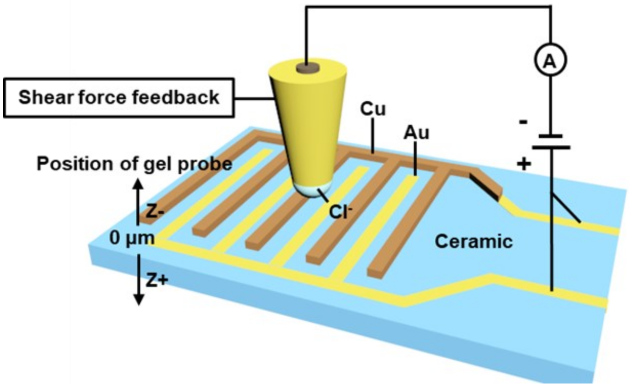

Figure 2.17 Scheme of line scan on Cu-plated Au interdigitated electrodes by shear force feedback SGECM.

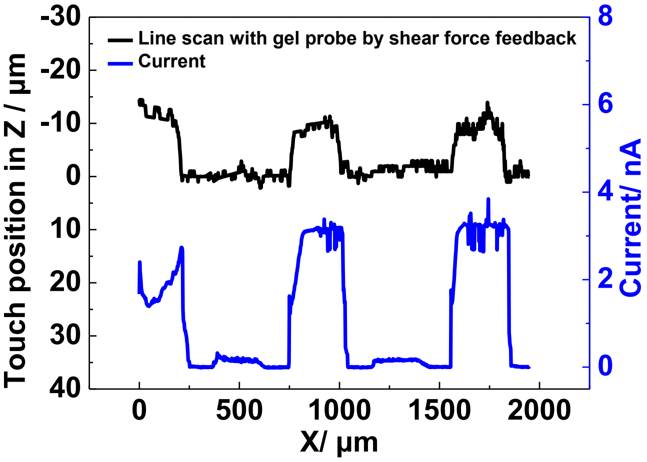

Figure 2.18 Line scan of profile and steady state current (E_{sample} *vs.* E_{probe} = 1.0 V) measured at touching position by shear force feedback.

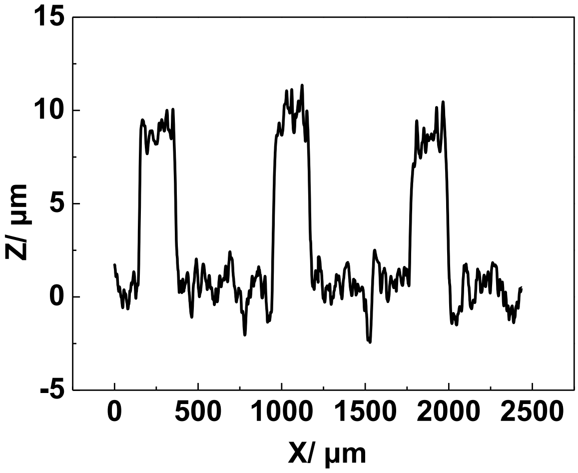

Figure 2.19 Surface profile of the Cu-plated Au interdigitated electrodes as measured by profilometry (Brüker Dektak XT).

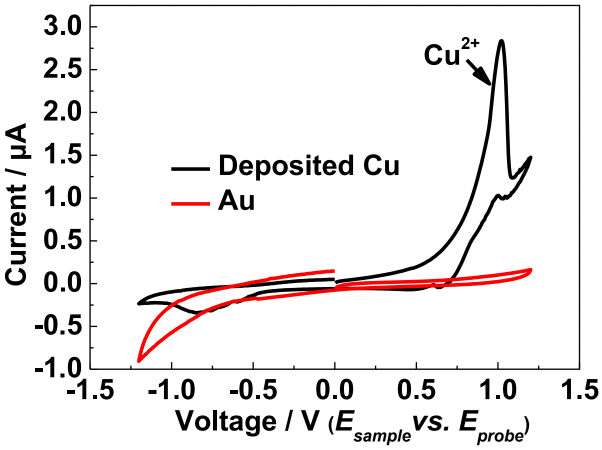

Figure 2.20 CV of the gel probe on Au and Cu-plated surfaces in modified interdigitated electrodes.

2.4 Summary

In conclusion, lateral physical resolution of SGECM is quantitatively analyzed from two aspects: the size of single sampling spots, and the line scan of periodically shaped reference samples. The former is achieved by locally oxidizing Ag to AgCl by the gel probe, leaving permanent colour change on the sample surface. The latter is carried out on a Cu TEM grid stick on a Fe plate. From both experiments, it is seen that current feedback has higher lateral physical resolution than shear force feedback with the same gel probe. This is because current feedback is more sensitive to the contact between the gel probe and the sample, and the gel is already pressed when shear force feedback indicates the touching. Therefore, current feedback is more favourable for conductive samples, but shear force feedback is more versatile especially to the samples with unknown conductivity. For the probe fabricated by electrodepositing chitosan on a 25 µm Pt disk electrode with Rg ≈ 2, the lateral physical resolution at touching position (z = 0) is *ca.* 50 µm for current feedback and *ca.* 63 µm for shear force feedback. More importantly, due to the soft nature of the gel, the physical resolution measured by AgCl deposition can be flexibly tuned from 14 to 78 µm by pulling or pressing the gel probe for a certain distance after touching the sample.

Chapter III Scanning gel electrochemical microscopy (SGECM): Potentiometric measurements

Apart from amperometric measurements in the previous chapter, SGECM can also be used for potentiometric measurements. This requires adaptation of both the instrument and the probe. For the instrument, the voltameter with high input resistance (Keithley 6430) is configured in SGECM to mapping the potential and topography simultaneously; for the probe, the chitosan is deposited on a micro-disk electrode with Ag wire is sealed. The Ag surface is oxidized to AgCl following the hydrogel deposition to specify the measured potential. In this chapter, the development and the results are discussed.

3.1 Introduction

Detection of the surface potential has been developed to an important analytical method to understand the mechanism of surface reactions. Varied characterization techniques have been developed for measuring the potential. The most established and commercialized one is Kelvin probe microscopy (KPM)[241–243]. It is powerful in detection of the contact potentials difference (CPD), which is the electrostatic potential difference arising between probe tip and sample surface as they are brought together in electrical contact and thermodynamic equilibrium is achieved. KPM has been achieved a sensitivity to contact potential variations in the mV range, obtaining a wide range of applications. For further developing KPM, force measurement was combined and named as Kelvin probe force microscopy (KPFM)[10,244–247]. It has higher resolution for both the contact potential difference and the lateral dimension and allows the simultaneous imaging of topography and contact potential difference. Although KPFM obtains superior spatial resolution with relatively high energy sensitivity compared to other measurement techniques, KPFM still has several limitations. First, the measurement is affected by the roughness of the surface and then the measured surface potential value does not always represent of the contact potential between the tip and sample. Second, KPFM sometimes may not well reflect the electrochemical information of sample surface. For example, the corrosion potential of the material exposed in a corrosive media is a mixed electrochemical potential affected by both the oxidation of the material and the reduction of the media (typically O_2 or H^+).

Local electrochemical techniques also have been developed to detect the local electrochemical potential. Scanning reference electrode technique (SRET)[248,248–250] and scanning droplet cell (SDC)[127,128,163,251] are mainly included. SRET allows the measurement of localized variation of potential (due to current flow) over the surface of an electrochemically active specimen. When it's working, the whole specimen is immersed in the solution and the probe is held at a small constant height above the specimen surface. This brings difficulties in measurements of highly reactive samples. Additionally, same with the KPFM, non-contact detection brings the other difficulty for the analyzing irregular surfaces. SDC is based on a small capillary filled with electrolyte solution. Small electrolyte droplets are positioned on the sample surface and enable a spatially resolved surface analysis or modification. Since the electrolyte is immobilized in the capillary, SDC shows an advantage of air operation, which means only the investigated surface is wetted, the other parts of the sample remain virgin. However, the spreading of droplet can be affected by the hydrophobicity and roughness of the sample surface, which causes a huge challenge of quantitative analysis.

Considering the importance of the potentiometric measurements, the potentiometric measurement of SGECM has been developed in this chapter. The analysis is based on a gel-based micro-reference electrode, which is fabricated by deposition of chitosan on Ag micro-disk electrode followed with Ag chlorination. The advantages of the potentiometric measurements by SGECM are:

(1) The real contact potential between gel probe and sample could be analyzed, which reflects the electrochemical properties of samples.

(2) The operation could be achieved in air, and the spreading of electrolyte could be inhibited by immobilization the electrolyte in the hydrogel.

3.2 Experimental section

3.2.1 Preparation of the gel-based micro-reference electrode

Micro-disk electrode of Ag was fabricated by embedding Ag wire of 50 μm diameter (99.99%, Alfa Aesar, USA) in pulled glass capillaries by epoxy resin. The diameter ratio of the insulating shield to the Ag wire (R_g) was approximately 2. The Ag micro-disk electrode was immersed in a chitosan solution containing 1% w/v chitosan (medium molecular weight, Aldrich), 0.125 mol/L $NaNO_3$, and 0.125 mol/L NaCl in 1:1 (vol. ratio) glycerol/H_2O. The pH of the solution was adjusted to 5.5 by HCl. The two-step electrodeposition was carried out in a three-electrode system with the Ag micro-disk electrode as working electrode, Ag wire coated with AgCl as quasi reference electrode (Ag/AgCl QRE) and a Pt wire as counter electrode. First, −1.75 V was applied for 150 s allowing chitosan to be electrodeposited. Then, the potential was immediately switched to 0.1 V for 30 s to chlorinate Ag. After preparation, the gel-based micro-reference electrode (denoted as Ag/AgCl-gel) was either used as is or soaked in an electrolyte solution according to the need.

3.2.2 SGECM potentiometric measurements with the gel-based micro-reference electrode

The Ag/AgCl-gel electrode was used as the gel probe for SGECM potentiometric measurements. The probe was approached to be in contact with the sample by shear force feedback. Once the probe touched the sample (defined as the reference z position as determined by 0.6% change in the amplitude of shear force signals), it was held for 2 s allowing a stable potential between the sample and the probe to be recorded by a voltammeter with high input resistance (Keithley 6430). For sequential measurements such as line scan or mapping, the probe was retracted for 70 μm, laterally moved for 50 μm, and re-approached to the sample for the next acquisition. Line scans of 1500 or 2000 μm and maps of 2000 × 2000 μm^2 were generated with such tapping schemes.

The stability of the Ag/AgCl-gel probe was evaluated by SGECM line scans on ITO surface. The gel was soaked in redox couple solutions with three different ratio (1:0.1, 0.1:0.1 and 0.1:1, in mmol/L) of $[Fe(CN)_6]^{3-}/[Fe(CN)_6]^{4-}$, 0.1 mol/L KCl in 1:1 (vol. ratio) glycerol/H2O for 15 min. The mapping experiments were carried out using the as-prepared gel probe. The sample was made of two strips of conductive Cu tape on an Al plate. The thickness of the tape was ca. 40-70 μm as measured by profilometry (Brüker Dektak XT). This is a typical sample mimicking the galvanic couple of metals. All the solutions used in this work were prepared with analytical grade chemicals and high-purity water (Purelab, Elga). The electrodeposition and SGECM measurements were operated at room temperature without special control of humidity.

3.3 Results and discussion

3.3.1 Probe fabrication

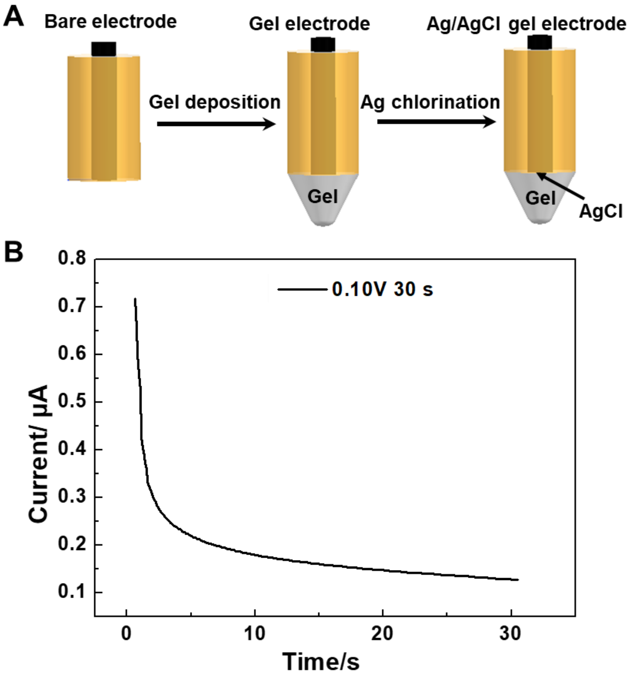

Figure 3.1 Scheme of the preparation of Ag/AgCl-gel probe(A), Ag Chlorination. (Potential *vs*. Ag/AgCl QRE) and image of the probe (B).

Figure 3.1A shows the scheme for preparing the Ag/AgCl-gel probe. Same with the gel probe fabricated with Pt microelectrode, chitosan could also be deposited on the Ag micro-disk electrode to fabricate the probe for potentiometric measurements. Since the Ag is not active as Pt, more negative potential (−1.75 for 150 s) must be applied in electrolysis of the water. Following the gel deposition, the Ag surface is oxidized to AgCl at 0.1 V for 30 s immediately in the same solution. The image of the probe and the oxidation curve of Ag are given in **Figure 3.1B**. AgCl was expected to form on Ag surface due to the presence of Cl- in the solution. The thickness of AgCl was estimated to be around 0.7 μm, from the oxidation charge by Faraday's Law.

3.3.2 Stability and reliability of the probe

Before applying the potentiometric measurements of SGECM, it is necessary to characterize the stability and reliability of the gel probe as micro-reference electrode. This was achieved by soaking three groups of redox couple electrolytes into gel electrodes. The electrode carrying the new electrolyte was approached to contact ITO surface until the shear force signal changed by 0.6%. Then the electrode was retracted for 2 μm and kept for 2 s for potential measurement. The scheme is given in **Figure 3.2A**. Here, ITO served as a flat conductive substrate, so the potential is determined by the ratio of redox couple. It is seen from **Figure 3.2B** that the average potential of 1:0.1, 0.1:0.1 and 0.1:1 mmol/L $[Fe(CN)_6]^{3-}/[Fe(CN)_6]^{4-}$soaked probes were 210, 148 and 85 mV, respectively. The potential difference followed well the Nernst Equation, indicating that the Ag/AgCl$^-$gel probes were reliable reference electrodes. Moreover, the variation of potential for the same probe over line scan of 2000 μm (82 sampling points, about 500 s) was less than 10 mV (standard deviation < 2 mV). This confirmed that the probes were stable for potentiometric measurements in SGECM.

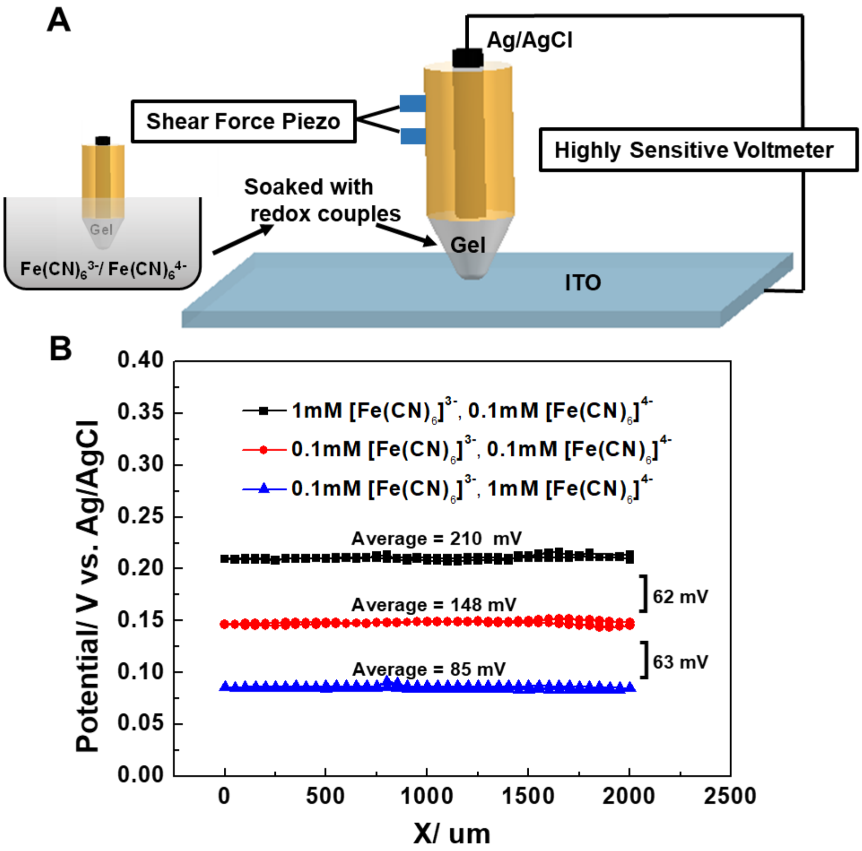

Figure 3.2 Scheme of the reliability test of Ag/AgCl-gel electrodes(A), Potentiometric line scan using Ag/AgCl-gel electrodes soaked with different concentration of $[Fe(CN)_6]^{3-}/[Fe(CN)_6]^{4-}$(B).

3.3.3 Potentiometric measurements by SGECM

The Ag/AgCl-gel probes were used in potentiometric SGECM measurements for simultaneously imaging the topography and electrochemical potential of the sample (**Figure 3.3A**). A freshly prepared probe was taken to measure an Al plate with two strips of Cu tape (surface profile shown in **Figure 3.3B**). With the shear force feedback, the probe was approached to the sample at each sampling point (x, y), and the reference z position (indicating contact) was recorded for constructing the topography map (**Figure 3.4A**). The steps between the Cu tapes and the Al substrate are clearly seen. The thickness of the tape is *ca.* 40-70 μm, and the edges of the tapes are slightly thicker than the bulk. This is in accordance with the trend measured by profilometry. Moreover, the potential between the sample and the gel probe was also measured at each sampling point when the probe touched the sample, and the potential map of the sample was generated accordingly (**Figure 3.4B**). Significant difference in potential is observed for Al and Cu surfaces, and therefore the steps between them could also be identified from the potential map. Here, the potential refers to the electrochemical potential (corrosion potential) at the sample/gel interface, which is determined by the kinetics of oxidation of the metal and the reduction of oxidants such as O_2 in the gel. It is *ca.* −0.18 V for Cu and −0.5 V for Al, indicating that Al is more active than Cu. The values are close to those measured in neutral electrolyte solutions. Based on the results, one can simultaneously analyze the topography and the local electrochemical reactivity of samples.

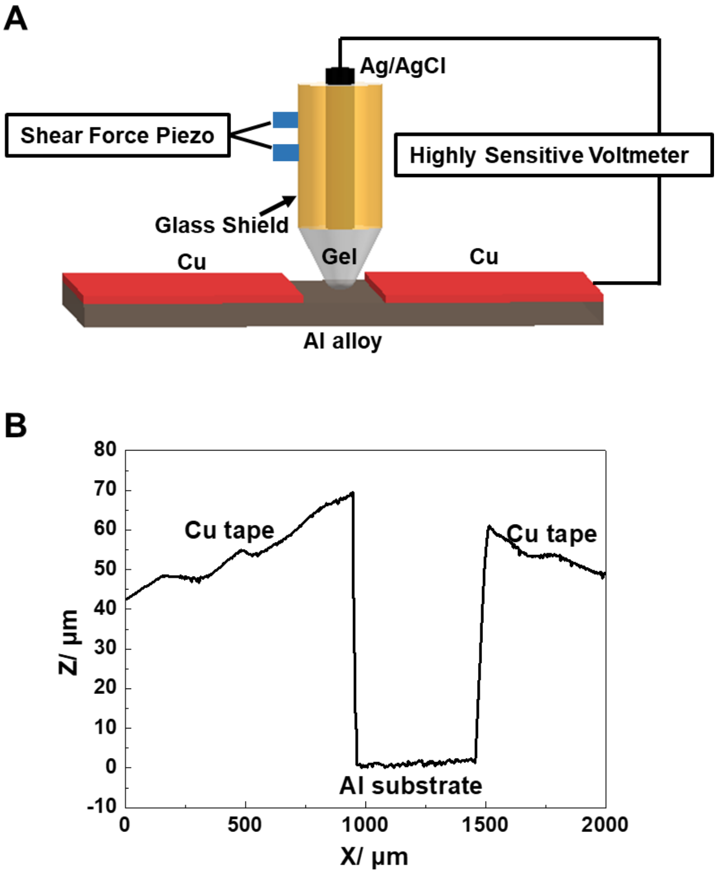

Figure 3.3 Scheme of potentiometric measurement on Al-Cu sample using Ag/AgCl-gel electrode (A), Surface profile of Cu tapes on Al substrate (B).

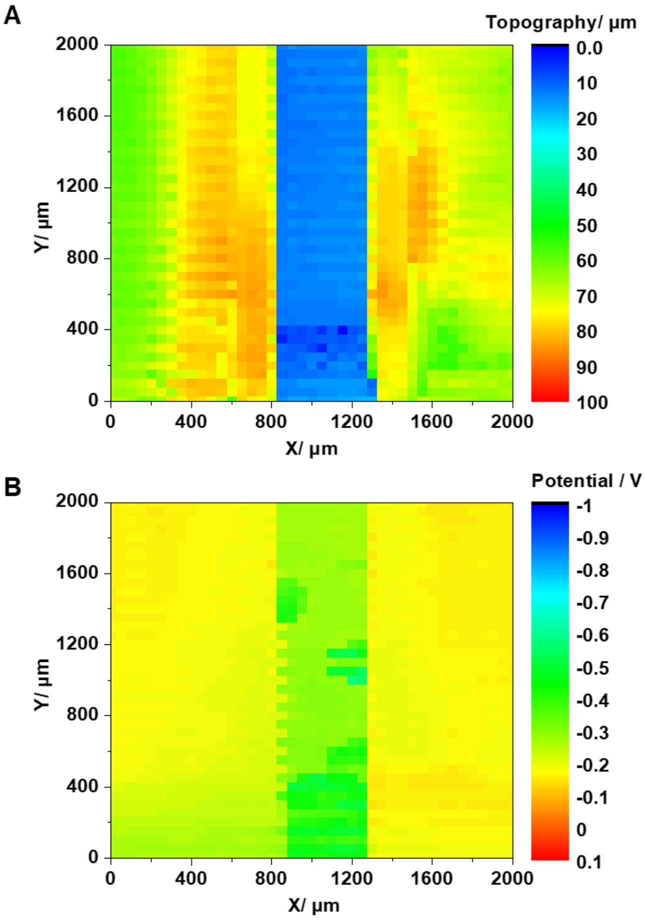

Figure 3.4 Topography (A) and potential mapping (B) by SGECM potentiometric measurement mode on Al substrate with Cu tapes.

After the first imaging, the probe was used to measure the same sample again. The results are shown in **Figure 3.5**. It is seen that the copper tape and aluminum substrate could still be distinguished from both the topography and the potential mapping. Nevertheless, the boundary between aluminum and copper is less clear from the topography image. In the potential mapping, the potential of copper tape has a bit positive shift. Since the copper tape was corroded after the first test, the corrosion products may cover on the copper surface alternating the corrosion potential.

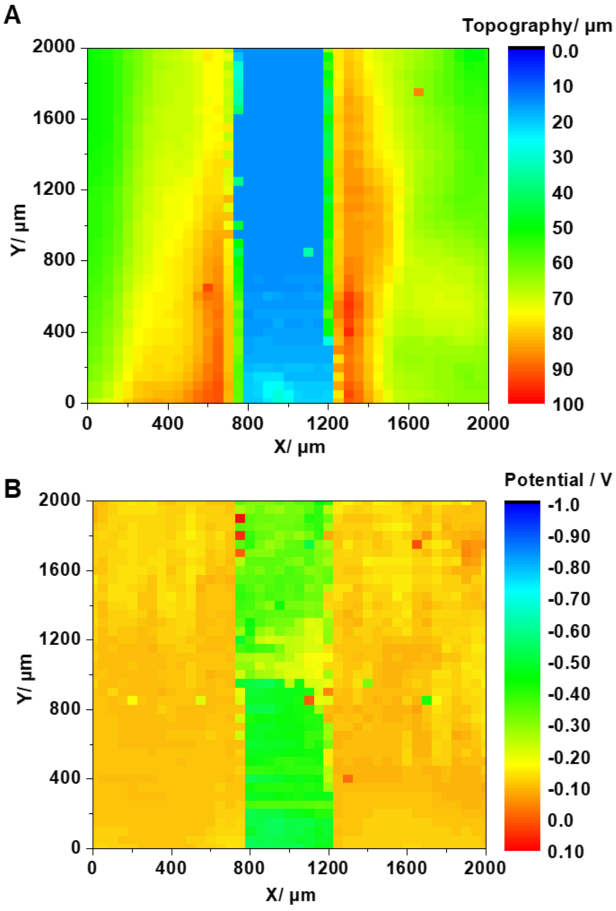

Figure 3.5 The second test with the same electrode on the same sample. (A) topography image, (B) potential image.

As compared with current mapping at constant applied potential, a major advantage of the potentiometric mapping is that the results are much less dependent on the contact area between the gel and the sample. For example, **Figure 3.6** shows two potential scans over the same line of the sample. They were purposely measured with different probe-sample distance, *i.e.* with the probe withdrawn 2 and 5 µm from the reference *z* position. From **Chapter II** it is known that the contact area would be different, even though the exact values were not measured. It is seen that the two lines almost overlap, indicating that the potentiometric measurement is not sensitive to the contact area and the pressure of the gel. This is different from amperometric measurements and may allow reliable potential to be measured even without accurate control of the probe-sample distance.

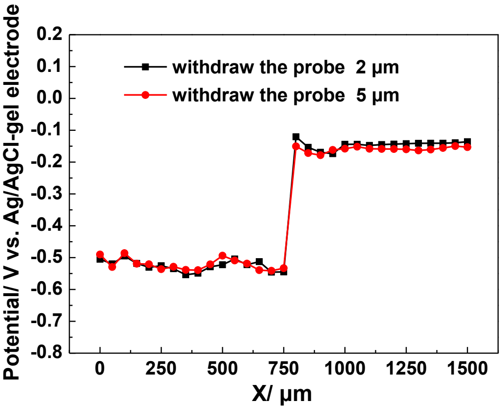

Figure 3.6 Potentiometric line scans on Al-Cu sample with gel probe withdrawn 2 and 5 μm from the reference *z* position.

3.4 Summary

Ag/AgCl-gel micro-reference electrodes were developed as potentiometric probes for SGECM measurements. The probes were prepared by electrodeposition of chitosan hydrogel on Ag micro-disk electrodes followed by Ag chlorination. They were approached to the sample surface by shear force feedback, and the potential between the sample and the probe were recorded by a highly sensitive voltammeter. Experiments on ITO (using the probe soaked with $Fe(CN)_6^{3-}/Fe(CN)_6^{4-}$ redox couple) proved that the probes were reliable and stable. Simultaneous mapping of topography and electrochemical potential was demonstrated on a model sample consisting of Cu tapes on Al plate. The two metals were clearly identified from both topography and potential maps. All the measurements were carried out with the sample exposed in air, which offers possibility for measuring complex-shaped samples in field tests. Moreover, the potential was not sensitive to the pressing of the gel, indicating that reliable potentiometric measurements can be conducted even without accurate control of the probe-sample distance. SGECM potentiometric measurements may be highly useful for locally analyzing the redox state of materials and the corrosion potential of metals.

Chapter IV Improvement of the gel probe by cross-linking

4.1 Introduction

In both amperometric and potentiometric measurements, the gel probe is approached to be in contact with the sample surface. The resolution of the analysis with SGECM is based on the contact area between gel hydrogel probe and the sample surface. Because of the soft nature of the gel, the gel is deformed during the approaching and the retracting. For example, the gel is squeezed when the probe is touching with sample surface by shear force feedback. The gel is also stretched when the probe is withdrawn because of the adhesion force between hydrogel and sample surface. Considering that the gel probe undergoes at least one pressing-stretching-restoration cycle at each sampling point, it suffers thousands of times the mechanical deformation during one array scan. Thus, it is critical to improve the mechanical stability of the gel probe to ensure the reproducibility of the tests.

Covalent cross-linking is a known method to enhance the mechanical strength of hydrogel. For chitosan, the most common covalent cross-linker is glutaraldehyde (dialdehyde). Aldehyde groups of dialdehydes enter into reactions with primary amine groups of chitosan, thus forming the Shiff's bases[252]. As a result, amine groups are blocked and chitosan structures are more inert and resistant to acidic media. The scheme of the reaction is given in **Figure 4.1**. However, the hydrophobicity of hydrogel will increase after cross-linking with glutaraldehyde, leading to a decrease in water content and ionic conductivity. Hence, the mechanical and electrochemical properties of chitosan shall be balanced for covalent cross-linking.

In this chapter, the mechanical strength of gel probe is improved by cross-linking the chitosan with glutaraldehyde. As the elastic modulus is one important parameter of mechanical properties of materials and the diffusion coefficient is often taken for quantitative electrochemical analysis, different methods have been applied to study the elastic modules of the hydrogel and the diffusion coefficient of redox couples in hydrogel. Besides, the limitations of these methods for testing such gel probes are also discussed.

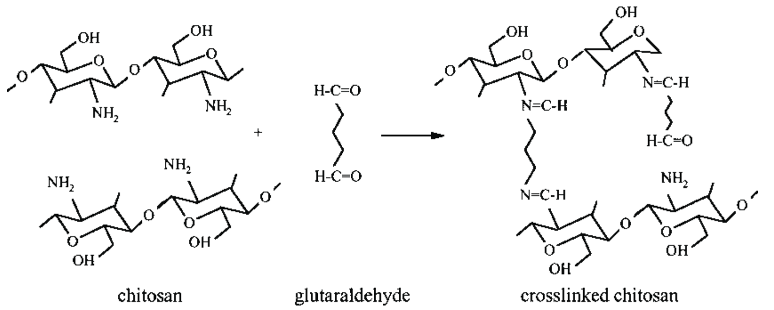

Figure 4.1 Scheme of the cross-linking reaction of chitosan with glutaraldehyde[253].

4.2 Experimental section

For cross-linking the hydrogel, the gel probe (fabricated with the same protocol in **Chapter II**) was immersed into 0.2% glutaraldehyde solution, which was prepared by diluting 25% glutaraldehyde solution in deionized water and glycerol (1:1 in volume) mixed solvent. After 2 hours, the probe was removed and rinsed in glutaraldehyde-free solutions based on water/glycerol (1:1 in volume) mixed solvent. In order to evaluate the factor of solvent to the stability of chitosan hydrogel, the cross-linked gel probe is immersed into 20 mM potassium ferrocyanide $K_4[Fe(CN)_6]$/ 0.1M KCl solutions with water/glycerol (1:1 in volume) as mixed solvent or pure deionized water as solvent.

The elastic modulus characterization of the hydrogel of probe was carried out by indentation on a micro-force sensing platform (FEMTO TOOLS, FT-MA30). The measurement is based on approaching a capacitive force sensing probe (FT-S200, spherical tip with radius of 25 μm) to the hydrogel sample at a set speed of 1 μm/s while recording the vertical position and the force signals. Once it touches the gel, it starts pressing until the force reaches a preset threshold of 10 μN. Afterwards, the probe was retracted from the gel. The measured force versus the displacement of the force probe is record for further quantitative analysis.

The ion diffusion behavior of the gel probe was studied with model redox probes by two methods. First method is approaching a gel probe (same with the probe in **Chapter**

II) soaked with 20 mM $K_4[Fe(CN)_6]$ on a microelectrode with smaller active diameter. The purpose here is to inhibit the positive feedback between two electrodes. This microelectrode was fabricated through sealing an etched Pt wire with sharp tip in a capillary by epoxy resin. After careful polishing, the exposed active diameter of Pt wire tip is *ca.* 4.5 μm. The cyclic voltammetry is measured with this microelectrode as working electrode and the gel probe as reference/counter electrode. Second method is immersing the gel probe into 1 mM $Fc(MeOH)_2$ immediately then carried out the cyclic voltammetry with a Pt wire as the reference/counter electrode. For both methods, the diffusion coefficient value of the redox couples could be estimated from the steady state current in voltammograms according to the **Equation 1.1**.

4.3 Results and discussion

4.3.1 Cross-linking of the gel probe

Figure 4.2A shows the fresh gel probe deposited in chitosan solution. The shape of the hydrogel is in consistent with the hemispherical diffusion of micro-disk electrode. After cross-linking in the glutaraldehyde solution for 2 hours, the shape of the gel is almost the same (**Figure 4.2B**). After cross-linking, the gel probe was immersed into 20 mM $K_4[Fe(CN)_6]$ solution to wash the residual glutaraldehyde and soak the redox couple in gel (**Figure 4.2C**). It is interesting that the solvent plays an important role in exchanging the electrolyte in gel. As shown in **Figure 4.3**, the gel is deposited and crosslinked under the same conditions. However, when the probe was immersed into pure water solutions, the gel was dissolved. Because of the strong solvent exchange between hydrogel and the bulk solution, the structure of the hydrogel was destroyed by the diluting of the glycerol. So, it suggests that the solvents should be always the same during soaking or exchanging the electrolytes in order to avoid the dissolution of gel.

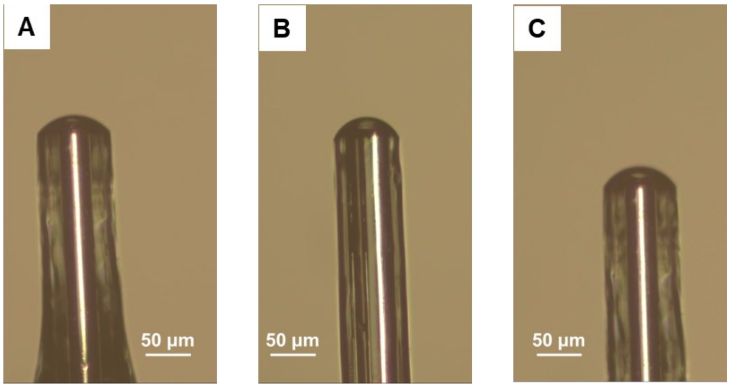

Figure 4.2 Images of gel probe after deposition in chitosan solution (A), after immerse in 0.2% glutaraldehyde solution for 2 hours (B), after immerse in 20 mM $K_4[Fe(CN)_6]$ solution with water/glycerol (1:1 in volume) as solvent for 5 minutes (C).

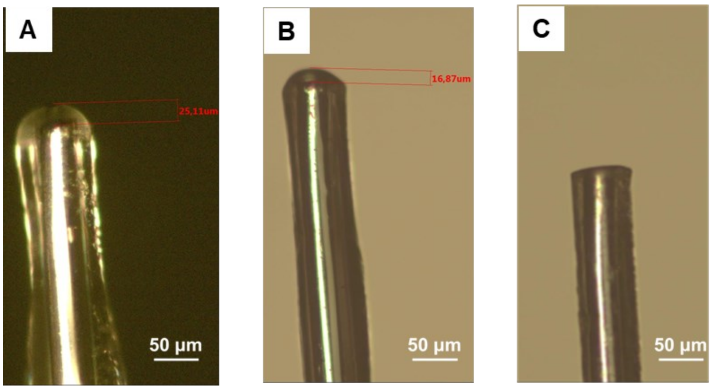

Figure 4.3 Images of gel probe after deposition in chitosan solution (A), after immerse in 0.2% glutaraldehyde solution for 2 hours (B), after immerse in 20 mM $K_4[Fe(CN)_6]$/ 0.1M KCl solution with pure deionized water as solvent for 5 minutes (C).

4.3.2 Elasticity test of the gel probe

Elastic modulus is a measure for the resistance of an object or substance against elastic deformation when a stress is applied to it. Here, the elastic modulus is tested to evaluate the mechanical properties of hydrogel. The indentation test was applied to the gel probe before or after cross-linking. The probe was approached into the hydrogel and then retract to be detached with the force recorded versus the displacement. The curves are shown in **Figure 4.4**. It is obvious that force is zero when the probe is far away from the gel. When the force sensing probe touches the gel, the force decreases suddenly and shows a negative spike because of the adhesion force. The position is normalized to 0. As the probe further approaches, the force increases gradually until reaching the threshold. It is seen that the slope of curve in positive force is higher after crosslinking the gel. This means the gel is more tough after reaction with glutaraldehyde due to the chemical bond generated between amino (chitosan) and carbonyl (glutaraldehyde) groups.

The curves with the positive force feedback are fitted based on the **Equation 1.4**. The factors of the finite thickness of the material is considered and the Poisson's ratio is assumed 0.5. The fitting curves are given in **Figure 4.5A** and **Figure 4.5B**. It is shown that the Young's modulus of blank gel and cross-linked gel are 3.834×10^4 N/m^2 and 1.8405×10^5 N/m^2, respectively. It is obvious that the mechanical strength of chitosan hydrogel is enhanced after cross-linking. However, as the adhesion force between the force probe and the hydrogel could not be neglected, the fitting based on Hertz model is not accurate. This also explains the bad quality of the fitting.

The retract curves are more informative than the approach curves. Since the adhesion information could be read from the retract curves, they are often used to study the elastic modulus based on the adhesion force. The lowest points in curves represent the adhesion force between the hydrogel and the force probe tip[223]. It's seen that the chitosan without cross-linking shows much higher adhesion force (*ca.* 27 μN) than the cross-linked chitosan (*ca.* 12 μN). This also proves that the mechanical property of chitosan is improved with the glutaraldehyde. In addition, for the fresh hydrogel, the force probe was withdrawn for *ca.* 70 μm to be detached with the hydrogel, demonstrating that the structure of the cross-linked hydrogel is stronger and deformation is less, which agrees well with the approaching tests.

Considering the adhesion force, the retract curves of fresh gel and cross-linked gel are fitted by the JKR (**Equation 1.5** and **Equation 1.6**) and DMT (**Equation 1.9**) models. However, as shown in **Figure 4.6**, the JKR model cannot fit the curves very well. While, for the DMT model, it can just matchable with the fresh gel. The extracted elastic modulus is 4.833×10^4 N/m^2 with a not perfect R-square value. Why these two models are not working well for fitting the force-displacement curves measured on our gel probes? The reason might be:

(1) For both JKR and DMT models, the radius of the force probe is much smaller than the touched surface. Then the deformation of the gel in tangent plane is negligible. But in our tests, the size of the force probe is comparable with the deposited hydrogel, then the deformation of the gel indeed affects the measurement and causes the errors in fitting.

(2) In the derivation of equations of models, the Poisson's ratio of chitosan is assumed as 0.5. However, this value is the Poisson's ratio of incompressible materials. When the chitosan is swelling, the migration of the solvent should be pay attention. Then the Poisson's ratio should be detected purposely based on the models which taking the viscoelastic and poroelastic deformation into account[254].

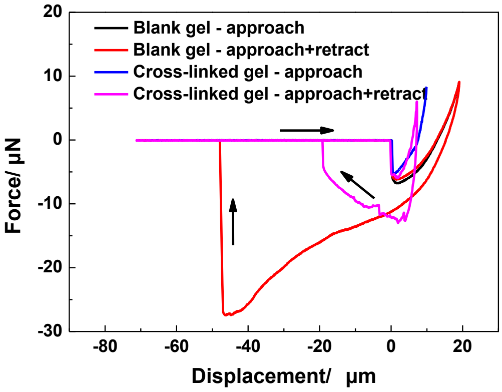

Figure 4.4 Microforce test of chitosan hydrogel deposited on the Pt microelectrode.

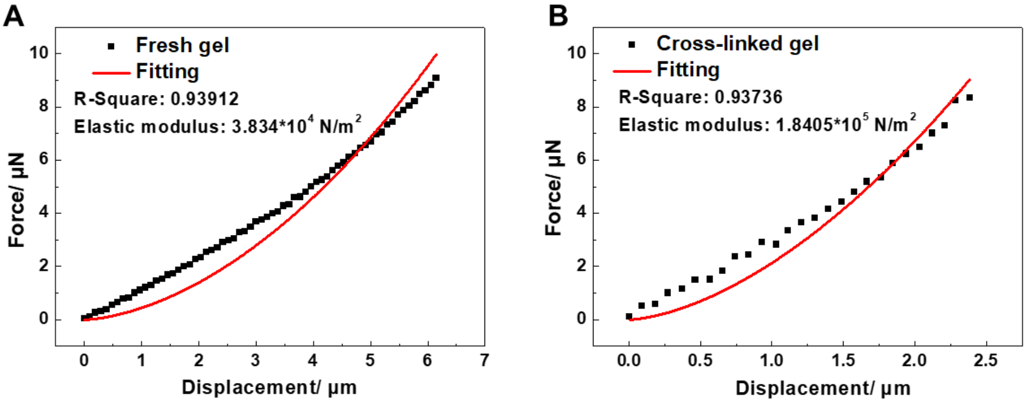

Figure 4.5 Data fitting of approach curves based on the Hertz mode. Fresh gel without cross-linking (A), cross-linked gel (B).

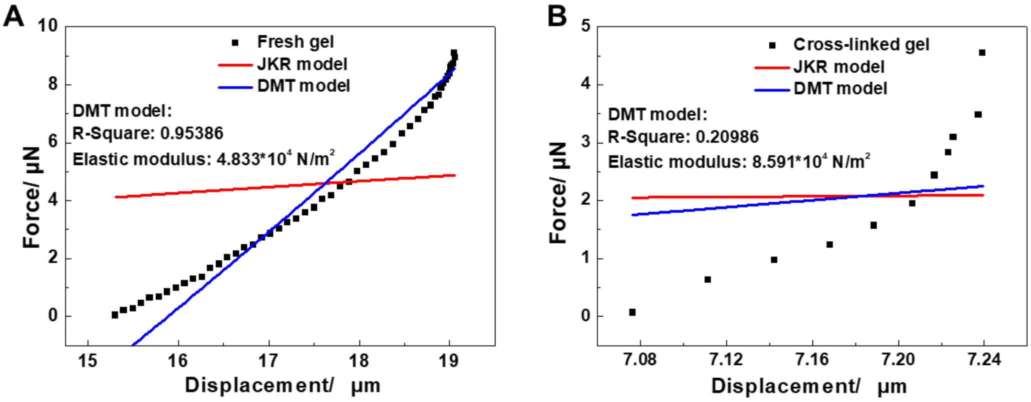

Figure 4.6 Data fitting of approach curves based on the JKR model and DMT model. Fresh gel without cross-linking (A), cross-linked gel (B).

4.3.3 Diffusion coefficient test of the gel probe

In order to improve the mechanical strength of gel without sacrificing too much the conductivity of electrolyte, diffusion coefficient is a key parameter to be tested. Apart from that, for quantitative analysis in SGECM, it is also necessary to know the exact value of diffusion coefficient of redox species in hydrogel. The diffusion coefficient is affected by the glycerol in solvent, the hydrogel deposited on the electrode, and the cross-linker. In order to study the factor of the glycerol, the cyclic voltammetry scans were carried out in 20 mM $K_4[Fe(CN)_6]$ solutions with Pt wire as reference and counter electrode. The solvents of solutions are deionized water and mixture of deionized water and glycerol, respectively. The result is shown in **Figure 4.7A**. It is seen that the steady state current in water and glycerol solution is much lower (around 7 times) than in water. In aqueous solution with 0.1M KCl as supporting electrolyte, the diffusion coefficient of $K_4[Fe(CN)_6]$ is 6.6×10^{-12} m^2 s^{-1} [255]. So, in the water and glycerol (1:1 in volume) solution, the diffusion coefficient of $K_4[Fe(CN)_6]$ is around 9.4×10^{-13} m^2 s^{-1}.

For in-situ studying the electrochemical behavior of the gel probe, the setup in **Figure 4.6** is used to achieve the cyclic voltammetry. The gel probe immobilized with 20 mM $K_4[Fe(CN)_6]$ was approached on the 4.5 µm microelectrode with shear force feedback. The cyclic voltammetry was achieved with 4.5 µm microelectrode as working electrode, and 25 µm microelectrode as reference and counter electrode. The curves are shown in **Figure 4.7 B** and **Figure 4.7 C.** Comparing with the steady-state current tested by bare 4.5 µm microelectrode, the current in gel is much lower. Perhaps the gel is squeezed by during approaching then the diffusion layer is limited by the deformed gel. As the results, the current is inhibited. However, this still is the preliminary result, we cannot conclude that the diffusion coefficient is indeed affected by the coated gel.

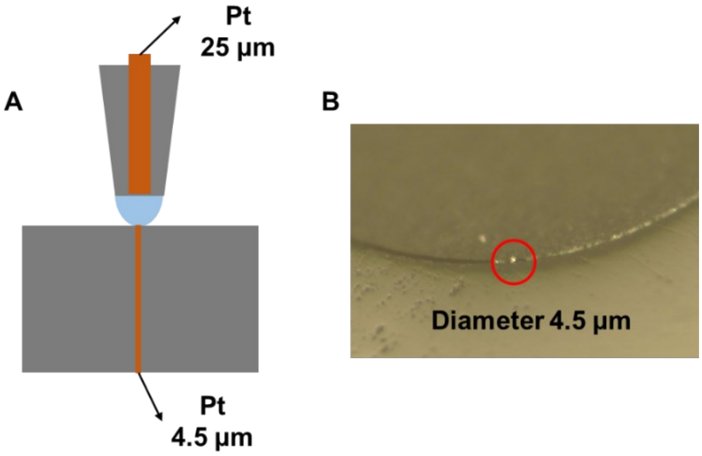

Figure 4.7 Scheme of the in-situ characterization of the gel probe (A), image of the Pt microelectrode with diameter of 4.5 µm (B).

The electrochemical behavior of the gel probe was also analyzed through immersing the probe into 1mM $Fc(MeOH)_2$ bulk solution and applying cyclic voltammetry. The voltammograms are shown in **Figure 4.8 B**. It is seen that the steady state current of the probe coated with fresh gel is higher than the bare Pt electrode. This may be caused by the adsorption of $Fc(MeOH)_2$ in chitosan. It is reported that this behavior does not appreciably differ the diffusion coefficient[214]. After cross-linking the gel for 2 and 4 hours, the current is lower than in the fresh gel because the protonated amino groups are covalently bonded. But comparing with the bare electrode, the current is overlapped at 0.3 V. This means that the gel after cross-linking for 2 and 4 hours has negligible effect on the diffusion coefficient. However, at 0.45V, the current is higher, perhaps because of the accumulation of the $Fc(MeOH)_2$ in the chitosan. After crosslinking 16h, it's seen that the steady state obviously decreased, which means the diffusion coefficient is lower. After cross-linking, the molecular mesh size is shrinking and the resistance of diffusion of redox species is raised.

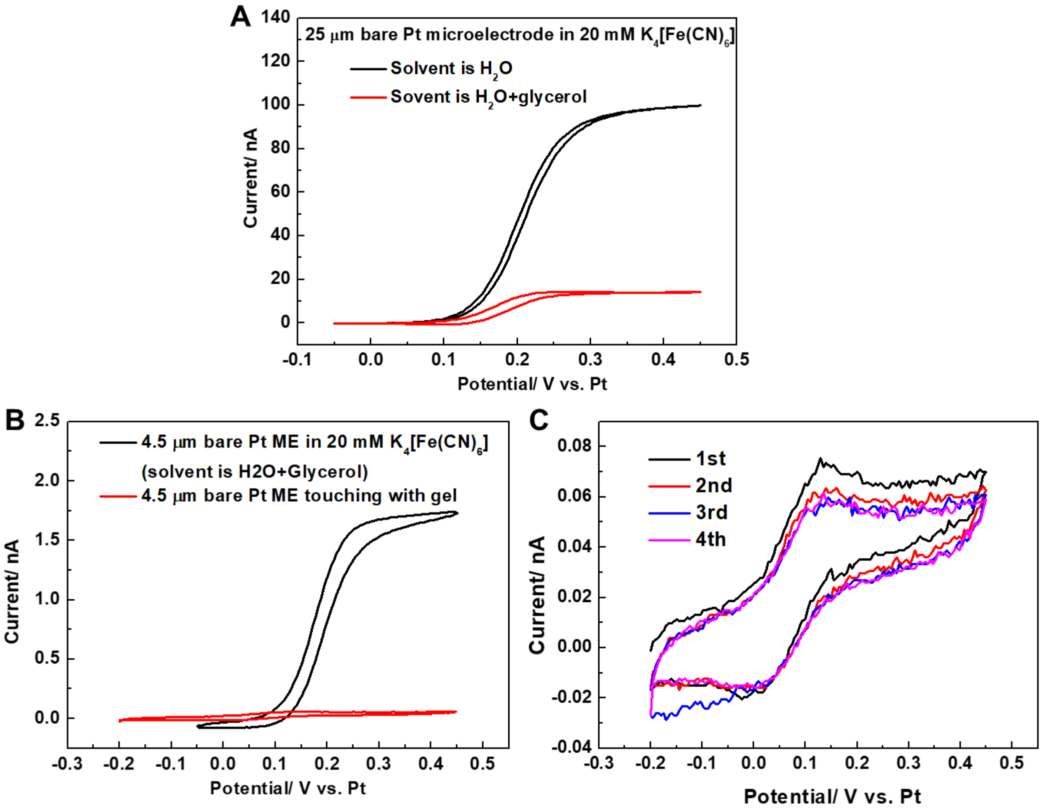

Figure 4.8 CV of 25 μm Pt microelectrode in 20 mM $K_4[Fe(CN)_6]$ bulk solutions, the solvents are deionized water and the mixture of deionized water and glycerol (A). CV of 4.5 μm Pt microelectrode in 20 mM $K_4[Fe(CN)_6]$ bulk solutions with adding glycerol in solvent, and in gel soaked with 20 mM $K_4[Fe(CN)_6]$ with water and glycerol as solvent (B). Full range of the CV of 4.5 μm Pt microelectrode tested in gel in **Figure 4.8B** (C).

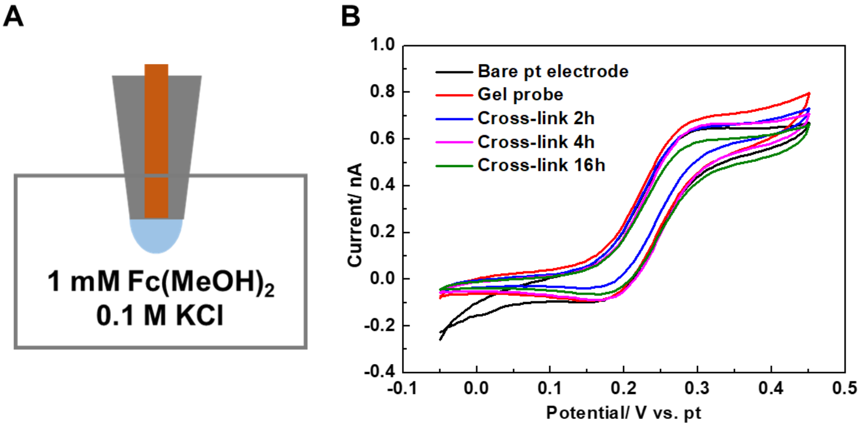

Figure 4.9 Scheme of the CV of gel probe immersed in 1mM $Fc(MeOH)_2$ solution (A). Cyclic voltammograms of the gel probe without and with cross-linking (B).

4.4 Summary

In this chapter, attempts have been made to improve the performance of gel probe for the application in SGECM. This was achieved by cross-linking the electrodeposited chitosan with glutaraldehyde. The mechanical properties and the electrochemical behavior of the gel probe were analyzed. The micro-indentation tests show that the elastic modulus was enhanced after cross-linking 2 hours in 0.2% glutaraldehyde solution. The cyclic voltammetry suggests that the diffusion coefficient of redox couple is 7 times inhibited by the glycerol in solvent. By immersing the gel probe into bulk $Fc(MeOH)_2$ solutions, we found that deposited gel or cross-linking of gel for a short time (2 hours, 4 hours) have no significant effect on the diffusion coefficient. However, the diffusion coefficient was decreased obviously after long-time cross-linking (16 hours).

Chapter V Development of the integrated probe for local electrochemical analysis

5.1 Introduction

So far, both amperometric and potentiometric measurements have been carried out in SGECM. Once the gel probe is approached to touch with the sample surfaces by current or shear force feedback, the local electrochemical analysis could be performed. In amperometric analysis, the potential (either constant or alternative) is applied between the gel probe and sample with recording the current response. In potentiometric analysis, the potential between the Ag/AgCl reference gel probe and the sample is recorded by a voltammeter with the high input resistance. However, all these measurements are carried out with two-electrode system. Consequently, it is promising to build a three-electrode system, in which, electrochemical signature of the sample could be studied independently.

In this chapter, a new integrated probe is presented for further developing a gel probe to specify the potential applied on samples. For fabricating the integrated probe, a Pt microelctrode wrapped with Ag/AgCl wire on its shield is inserted into an external capillary filled with electrolyte. A special holder is printed for fixing the internal microelctrode and the external capillary. The integrated probe is carefully characterized and used for analyzing the small volume droplets by potentiometry and anodic stripping. Electrodeposition of chitosan on such integrated probes is also tried, which might open the door for local electrochemical analysis by SGECM with three-electrode system.

5.2 Experimental section

5.2.1 Chemical and materials

The metal wires (Pt of 25 μm and 1 mm diameter, Ag of 50 μm diameter) and the Pt foil are purchased from ChemPUR, Germany. The glass capillaries (One from Sutter

Instrument, one from Hilgenberg GMBH). Metal plates of Fe and Cu, as well as microscope glass slides, are used as samples for droplet analysis. The metal plates are polished with SiC paper up to 4000 grit and then cleaned by sonication in ethanol and acetone. For comparison, one Fe plate is coated with silane by electrodeposition. The deposition solution consists of 3.3 vol. % MTEOS (methyltriethoxysilane, Sigma), 1.15 vol. % TEOS (tetraethoxysilane, Sigma), 2/1 (v/v) ethanol/water mixed solvent and 0.2 M $NaNO_3$, with pH adjusted to 4 using hydrochloric acid. The solution is pre-hydrolyzed at 35 °C for 48 h. The electrodeposition is carried out on Fe plate at –1.4 V (vs. Ag/AgCl) for 300 s, and the film is rinsed by water and dried before use[256–258]. All the chemicals used in this work are reagent grade and used without further purification.

5.2.2 Preparation of the integrated probe

The integrated probe consists of three parts: a Pt micro-disk electrode, an Ag/AgCl wire, and an outer capillary filled with electrolyte, as illustrated in **Figure 5.1A**. The Pt micro-disk electrode is prepared with the same way as in **Chapter II**. The Ag/AgCl wire is prepared by oxidizing a 50 μm diameter Ag wire in 0.1 M KCl solution at 0.12 V (vs. Ag/AgCl) for 30 s. After rinsing with deionized water, the wire is wrapped around the glass shield of Pt microelectrode and fixed with tacky glue. The outer capillary with 1.8 mm inner diameter is pulled to have a short tip of *ca.* 1 cm. Then the Pt micro-disk electrode stick with Ag/AgCl wire is inserted into the outer capillary and naturally breaks its tip to have an opening of *ca.* 100 μm (**Figure 5.1B**). The inner micro-disk electrode and the outer capillary are fixed together with screw in a 3D printed holder that allows fixing to a motor for positioning the probe. The last step is to soak 0.1 mol/L KCl electrolyte into the integrated probe through the thin gap at the tip between the inner electrode and the outer capillary to obtain a real reference electrode. The photo of the parts and the integrated probe is shown in **Figure 5.1B**. We recommend to use Cu wire with insulating coating to make the electrical contact for both the Pt microelectrode and the Ag/AgCl wire to avoid short contact between them. Like classical reference electrodes, the integrated probe can be stored by immersion in 0.1 M KCl solution when not in use.

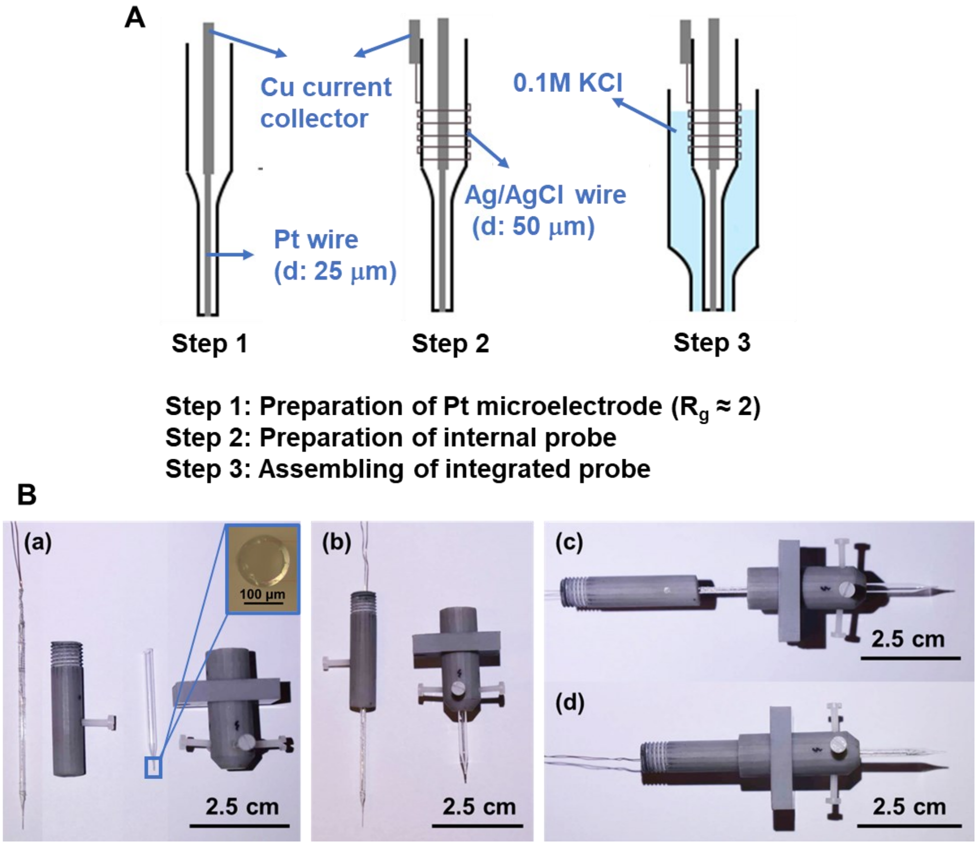

Figure 5.1 Scheme of the fabrication of the integrated probe (A), photographs illustrating different steps of the fabrication (B).

A major technical advantage of this design is the ease of preparation and refreshing of the probe. All the three parts do not have strict dimension requirement, and they can be easily dismantled and remounted. After dismantling the probe, the inner microelectrode can be polished, the electrolyte of the reference electrode can be replaced, and even the Ag/AgCl wire can be regenerated if needed. This means that the integrated probe can be easily and completely refreshed, which is highly important for electrochemical analysis. Moreover, the Ag/AgCl wire has much higher area than the Pt microelectrode, so it can also serve as counter electrode in a two-electrode system for amperometric measurements. The ring-shaped gap between the inner microelectrode and the outer capillary allows uniform symmetrical current distribution.

5.2.3 Characterization of the integrated probe

The integrated probe is characterized by electrochemical impendence microscopy (EIS), potentiometry and CV in bulk electrolyte solutions of large volume (ca. 20 mL). EIS is performed in 0.1 M KCl solution for measuring the resistance of the reference electrode of the integrated probe. The Ag/AgCl wire of the integrated probe is connected as working electrode (WE), a commercial Ag/AgCl electrode is used as reference electrode (RE) and a Pt foil is used as counter electrode (CE). The measurement is carried out at open circuit potential (OCP) with a 10 mV sinusoidal perturbation in the frequency range of 100 kHz to 0.1 Hz on an Autolab potentiostat (PGSTAT302N, Metrohm).

The potentiometry of the integrated probe is carried out in Fe^{3+}/Fe^{2+} redox couple solutions. The Fe^{3+}/Fe^{2+} solutions are prepared by dissolving $Fe_2(SO_4)_3$ and $FeSO_4$ in 0.1M KCl electrolyte with the ratio of 50:1, 10:1, 1:1, 1:10, 1:50 (in 10^{-3} mol/L). The OCP between the Pt microelectrode and the Ag/AgCl reference electrode of the integrated probe is recorded by a voltammeter with high input resistance (Keithley 6430). In order to estimate the response time of the integrated probe, the OCP was also record in Fe^{3+}/Fe^{2+} solution with step concentrations that were operated by dropping one specie into the initial solution every 600 s. The solution was kept stirring for accelerating the mixture of the added species.

The CV of the integrated probe is measured in a solution with 1 mM ferrocene methanol (FcMeOH) and 0.1 M KCl. The Pt microelectrode of the integrated probe is connected as WE. For two-electrode system that involves only the integrated probe, the Ag/AgCl wire is connected as both RE and CE. A three-electrode system that connects the Ag/AgCl wire of the integrated probe as RE and a separate Pt wire (1 mm diameter) as CE is also measured for comparison. The potential is scanned in the range of 0 to 0.6V at 10 mV/s scan rate.

5.2.4 Electrochemical analysis in droplets

Figure 5.2 illustrates the setup of droplet analysis using the integrated probe. A major concern is to keep the humidity of the environment to minimize the evaporation of the droplet. The sample is placed in a 3D printed plastic chamber with water reservoir. The hole at the top of the chamber allows putting the droplet by micropipette and inserting the integrated probe. Afterward, the gap between the probe and the chamber is rapidly sealed with parafilm, and then the probe is approached to be in contact with the droplet. 20 µL droplets of $Fe(NO_3)_3$ in concentration of 1, 5, 10, 25, 50 mM are dropped on bare and silane-treated Fe plates for potentiometric measurements. The measurement configuration is the same as potentiometric characterization of the probe in bulk solution. For amperometric measurements, 20 µL droplets of 0.1 M H_2SO_4 are dropped on Cu plates, and concentration of Cu^{2+} is traced by anodic stripping using the integrated probe. The Pt microelectrode is connected as WE, and the Ag/AgCl wire is connected as RE and CE for a two-electrode system. The stripping is carried out by preconcentration of Cu at –0.2 V for 30 s followed by CV scans from –0.08 to 0.6 V at scan rate of 50 mV/s. The calibration of Cu stripping was achieved by the integrated probe in 0.1 M H_2SO_4 and $CuSO_4$ solutions with concentration of 1, 2.5, 5, 10, 50 mM. For both potentiometric and amperometric measurements, control experiments are carried out on glass slides with the same protocols.

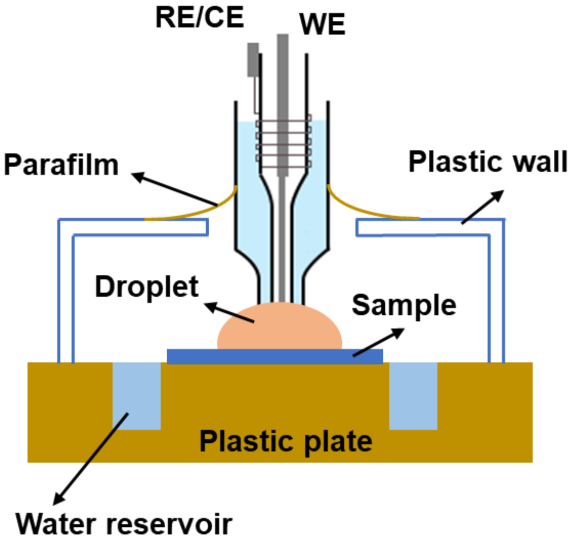

Figure 5.2 Scheme of the setup for electrochemical droplet analysis using integrated probe.

5.3 Results and discussion

In the integrated probe, the inner Pt microelectrode serves as WE, and the Ag/AgCl wire with KCl electrolyte serves as RE. Therefore, it is essential to evaluate the stability and reliability of the configuration especially for the Ag/AgCl RE. This is first carried out in bulk solutions by measuring their electrochemical behavior. Three aspects are tested: the ohmic resistance in the gap between the inner microelectrode and the outer capillary, the potentiometric and voltammetric measurements in standard redox solutions. As a further step, the probes are used for droplet analysis. Potentiometric analysis is carried out by following the open circuit potential of a Fe^{3+} droplet on Fe plate, and amperometric analysis of Cu^{2+} by anodic stripping is measured in a H_2SO_4 droplet on Cu plate. Based on the results, the kinetics of metal oxidation is also analyzed.

5.3.1 Evaluation of the integrated probe in bulk solutions

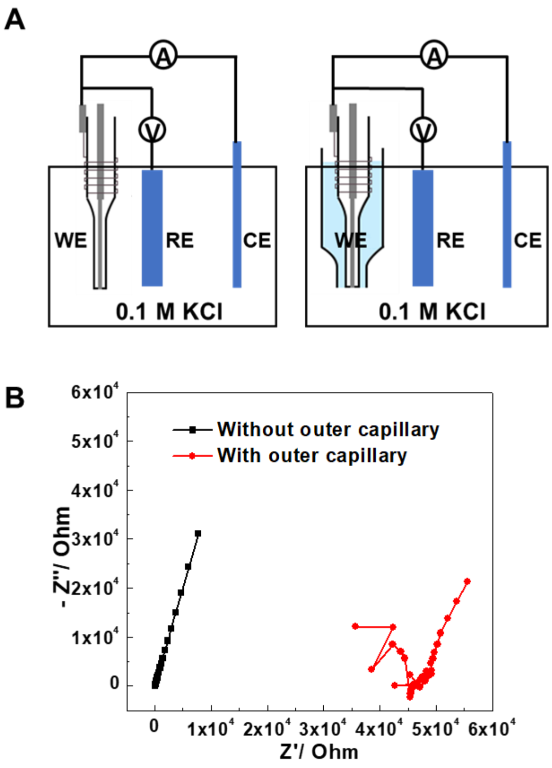

Figure 5.3 Scheme of EIS measurement (A), Nyquist plot of Ag/AgCl wire of the integrated probe in 0.1 M KCl solution with/without outer capillary (B).

A major criterion for RE is the ohmic resistance that originates from the ion exchange between its internal electrolyte and the external measurement media, as it determines the ohmic drop in electrochemical measurements[259]. In the integrated probe, it is mainly affected by the gap between the inner microelectrode and the outer capillary, which should allow ion exchange yet have low rate of solution leakage. Here, the ohmic resistance is measured by EIS in a two-electrode system, with the Ag/AgCl wire of the integrated probe as WE and a Pt foil as CE as illustrated in **Figure 5.3A**[227,260]. In this case, the DC resistance at high frequency mainly reflects the ion transfer resistance of the gap. From the Nyquist diagram, it is seen that the interception of the curve with the real axis is *ca*. 46 kΩ. It is much higher than that measured without the outer capillary (*ca.* 40 Ω), which confirms that the resistance indeed corresponds to the ion exchange through the gap.

Based on the measured resistance value, one may estimate the response time and ohmic drop of the integrated probe. Considering that the WE has a diameter of 25 μm, the double layer capacitance is about 98 pF (in 0.1 M KCl solution[261]), and the current in typical CV or amperometric measurements usually does not exceed 10 nA. Thus, one may estimate that the time constant of the cell is *ca.* 4.5 μs, and the IR drop at the RE is *ca.* 0.46 mV. This is acceptable for most of the electrochemical measurements, which will be further confirmed by potentiometric and voltammetric analysis. However, one should pay attention on the IR drop if using electrodes of larger diameter as WE in the integrated probe.

The potentiometric analysis of the integrated probe is carried out in redox couple solutions by measuring the OCP between the inner Pt microelectrode and the Ag/AgCl wire in the outer capillary, as illustrated in **Figure 5.4A**. The probe is initially placed in air, and then it is approached to immerse in the redox solution when the potential is monitored. **Figure 5.4B** shows the potential of the probe measured in Fe^{3+}/Fe^{2+} redox couple solutions with different ratio. The small plateau in the first 20 s corresponds to the “free” potential of the probe in air, which is meaningless. When the probe is in contact with the solution, the potential changes quickly before reaching equilibrium. The response time approaching from air to be in contact with electrolyte is *ca.* 50-150 s depending on the solution. After immersion, the response time of the probe for redox concentration change is recorded by concentration step measurements. The potential stairs are shown in **Figure 5.4D**. It’s seen that the initial response of the probe from air to the solution is similar with **Figure 5.4B**. However, once the probe is already immersed into solution, the response is much faster (*ca.* 30 s). It is still longer than usual potentiometric measurements with a large WE and RE, which might be attributed to the small area of the Pt microelectrode and the resistance of the ion exchange gap of RE. However, once the equilibrium is reached, the potential is highly stable for a long time of measurement. The potential versus the Fe^{3+}/Fe^{2+} ratio can be well fitted to Nernst equation as shown in **Figure 5.4C**. The slope is *ca.* 59 mV, and the R^2 is 0.996. Besides, the potential steps are symmetrical in **Figure 5.4D**, and the potential differences between two neighboring stairs are same. This also strictly follows the Nernst equation. The results in both **Figure 5.4B** and **Figure 5.4D** confirm that the integrated probe is reliable for potentiometric analysis in redox solutions.

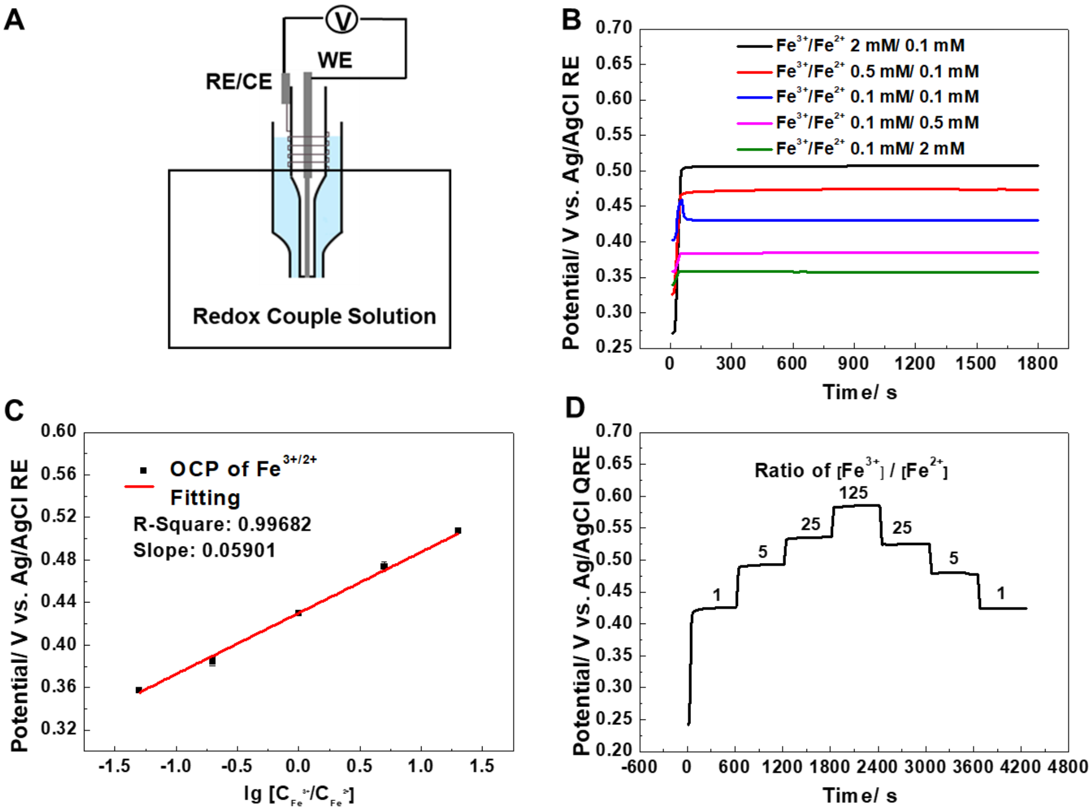

Figure 5.4 Scheme of potentiometric measurements of the integrated probe in bulk solutions(A), potential variation in Fe^{3+}/Fe^{2+} redox solutions with different concentration ratio (B), potential versus log($[Fe^{3+}]/[Fe^{2+}]$) (C), potential steps with different $[Fe^{3+}]/[Fe^{2+}]$ ratio (D).

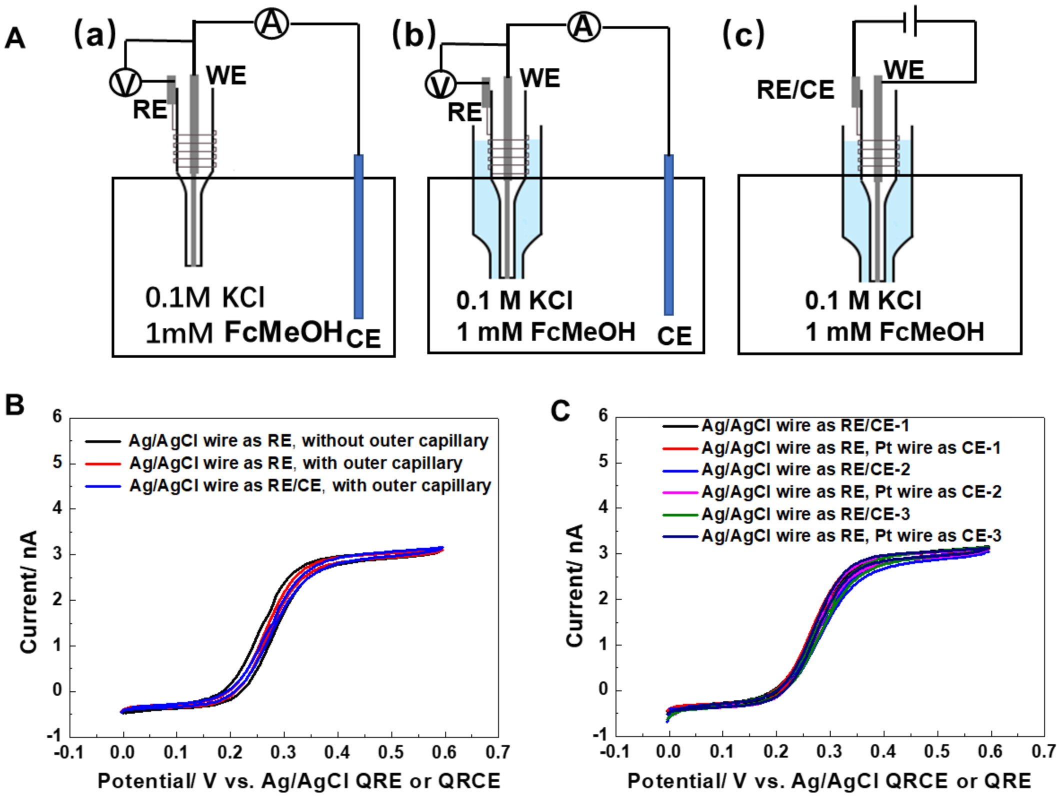

Figure 5.5 Schemes of CV in 0.1mM FcMeOH solution by integrated probe(A), CV of the integrated probe in 0.1mM FcMeOH solution with different configurations (B), CV measurements by two electrodes and three electrodes configurations (C). Scan rate in CV measurement is 10 mV/s.

Besides potentiometry, the integrated probe is also used for voltammetric measurements, taking advantage of the small size of the WE. Different configurations are compared for the measurement and illustrated in Figure **5.5A:** (a) Pt microelectrode as WE, Ag/AgCl wire as quasi-reference electrode (QRE) without outer capillary, and a Pt wire of 1 mm diameter as CE; (b) Pt microelectrode as WE, Ag/AgCl wire with 0.1 mol/L KCl in the outer capillary as RE, and a Pt wire of 1 mm diameter as CE; (c) Pt microelectrode as WE, and Ag/AgCl wire in 0.1 mol/L KCl in the outer capillary connected as both RE and CE. The results show classical sigmoidal shape voltammogram of microelectrodes in 0.1mM FcMeOH solution, and there is no significant difference between the three configurations (**Figure 5.5B**). Moreover, the measurements are highly reproducible with configuration (c) as shown in Figure 5C. This suggests that the Ag/AgCl wire in 0.1 mol/L KCl in the outer capillary functions well as RE, and it can even be used as CE as the area of Ag/AgCl is much higher than that of Pt microelectrode so that the polarization is negligible. The resistance of the gap between Pt microelectrode and the outer capillary appears to have no significant influence on the results, which is due to the low current in the measurement. This suggests that the integrated probe can also be used for voltammetric analysis in a two-electrode system, with the Pt microelectrode as WE and the Ag/AgCl wire in 0.1 mol/L KCl in the outer capillary as RE and CE.

The results above show that the integrated probe has acceptable ohmic resistance for the gap between the Pt microelectrode and the outer capillary. This allows the probe to be reliably used for potentiometric and voltammetric measurements in bulk solutions with large volume. Considering the small size of the tip of the probe (ca. 100 μm diameter), it opens the door for electrochemical measurements in small droplets. This will be demonstrated in the following sections.

5.3.2 Potentiometric measurements of Fe^{3+} droplets on Fe plate

As designed, the small size of the tip of the integrated probe (*ca.* 100 μm diameter) allows electrochemical measurements in small droplets. This is especially useful for tracking the evolution of chemistry of droplets, which may further indirectly reveal the kinetics of reactions at the droplet/substrate interface. For example, Turyan *et al.* analyzed the oxidation kinetics of therapeutic proteins in 150 μL droplets by potentiometry for rapid screening of their activities[262]. A classical qualitative method for evaluating the corrosion activity of metals is by droplets that change color upon reaction with the metal, *e.g.* $CuSO_4$. Here, we demonstrate an example of potentiometric analysis using the integrated probe for tracking the reduction of Fe^{3+} in a 20 μL droplet by steel substrate. The reactions are as follows:

$Fe^{3+} + e \leftrightharpoons Fe^{2+}$ (R1)

$Fe^{2+} + 2e \leftrightharpoons Fe_{surf}$ (R2)

The concentration ratio between Fe^{3+} and Fe^{2+} in the droplet follows Nernst Equation, which can be measured by the potential of the integrated probe:

$$E_{probe} = E^0_{Fe^{3+}/Fe^{2+}} - \frac{RT}{F} ln \frac{[Fe^{2+}]}{[Fe^{3+}]} \quad \textbf{(Equation 5.1)}$$

where $E^0_{Fe^{3+}/Fe^{2+}}$ refers to the standard electrode potential of Fe^{3+}/Fe^{2+} redox couple, R is the ideal gas constant (8.314 $J·K^{-1}·mol^{-1}$), T is the temperature (298 K) and F is the Faradic constant (96,485 $C·mol^{-1}$). As a result, knowing the initial concentration of Fe^{3+} and Fe^{2+} in the droplet, with the stoichiometry and the measured potential of the probe, one may derive the concentration of Fe^{3+} and Fe^{2+} at any time in the droplet. They can be expressed as follows:

$$[Fe^{3+}] = \frac{\frac{3}{2}[Fe^{3+}]_0 + [Fe^{2+}]_0}{\frac{3}{2} + exp\left[\frac{F}{RT}\left(E^0_{Fe^{3+}/Fe^{2+}} - E_{probe}\right)\right]} \quad \textbf{(Equation 5.2)}$$

$$[Fe^{2+}] = \frac{\frac{3}{2}[Fe^{3+}]_0 + [Fe^{2+}]_0}{1 + \frac{3}{2} exp\left[-\frac{F}{RT}\left(E^0_{Fe^{3+}/Fe^{2+}} - E_{probe}\right)\right]} \quad \textbf{(Equation 5.3)}$$

where $[Fe^{3+}]_0$ and $[Fe^{2+}]_0$ refer to the initial concentration of Fe^{3+} and Fe^{2+} in the droplet, respectively. As a result, the concentration variation as a function of time can be tracked, and it reflects the kinetics of the two reactions R1 and R2, notably the latter which corresponds to the oxidation reactivity of the steel surface and measures its corrosion resistance.

Figure 5.6 shows the variation of the probe potential as a function of time for 20 μL droplets on bare steel, silane-coated steel and glass substrates. In all measurements, the potential takes *ca.* 100 s to stabilize. Afterwards, the potential is almost constant in the droplet on glass substrate, and the value is the same as that measured in bulk solution. This suggests that after the response time of the integrated probe, the potentiometric measurements are reliable in small droplets. When the droplet is on bare steel substrate, it is seen that the potential decreases sharply until *ca.* 400s before reaching a plateau. This can be explained by the oxidization of Fe plate by Fe^{3+}, which consumes Fe^{3+} in the droplet and generates Fe^{2+} following the redox reactions R1 and R2. Due to the depletion of Fe^{3+} oxidant, the reactions spontaneously slow down and the system reaches equilibrium, which explains the potential of the integrated probe reaching a plateau. For comparison, we also tested the potentiometry of Fe^{3+} droplet on silane treated Fe plate. The silane treatment is a known method for temporary protection of metals again corrosion[256–258]. The general trend of the results is the same as on bare Fe plate, but the initial potential decrease is less steep, and the final equilibrium potential is more positive. This suggests that the generation of Fe^{2+} is slower, on silane-treated Fe plate than on bare Fe plate, which qualitatively supports the expected corrosion inhibition effect. Nevertheless, this inhibition is less significant with the increase of Fe^{3+} concentration. This might be related to the stronger attack of the silane film in more harsh media with higher concentration of the oxidant. Similar trends are also seen with other concentration of Fe^{3+}. Similar experimental systems have also been used in scanning electrochemical microscopy for analyzing localized corrosion of Fe, where Fe substrate is locally oxidized to Fe^{2+} and then Fe^{2+} is further oxidized to Fe^{3+} on the microelectrode contributing to the measured current.

Potentiometry has an advantage of not perturbing the electrochemical system. Thus, it is especially suitable for *in-situ* monitoring the variation of concentration of redox species with time, and only very small volume of analyte is required with miniaturized integrated probes. In theory, the results in **Figure 5.6** make it possible to further quantitatively analyse the kinetics of both reactions R1 and R2. However, in practice, attention must be paid for the experimental control. Rigorously, the potential measured from the integrated probe reflects only the surface concentration of Fe^{3+} and Fe^{2+} near the probe. Thus, the derivation of **Equation 5.2** and **Equation 5.3** from **Equation 5.1** requires an approximation that the concentration distribution is always uniform in the droplet. When the droplet is static on the surface, this approximation is unlikely fulfilled considering the size of the droplet. Assume the droplet has a contact angle of 60° with a flat surface, a 20 μL droplet has a height of *ca.* 0.156 cm. This will take *ca.* 76 s for an analyte generated on the sample surface to reach the top of the droplet (approximately taking linear diffusion with diffusion coefficient 2×10^{-5} cm^2/s) where the integrated probe is likely positioned. Another concern is the shape of the droplet, which depends on the contact angle and changes due to the capillary force when in contact with the integrated probe. This complicates the geometry for simulating the electrochemistry with mass transport in the droplet, even with the contact angle measured. Moreover, the response time of the probe is also an issue. From **Figure 5.4D** and **Figure 5.6**, it is clearly seen that the potential takes time to reach equilibrium. This limits the time resolution of the measurement, especially when the potential rapidly changes with time such as between 100 and 300 s in **Figure 5.6**. With all these considerations, the experiments need to be very carefully designed for meaningful quantitative analysis of the kinetics of the interfacial reactions between the droplet and the sample.

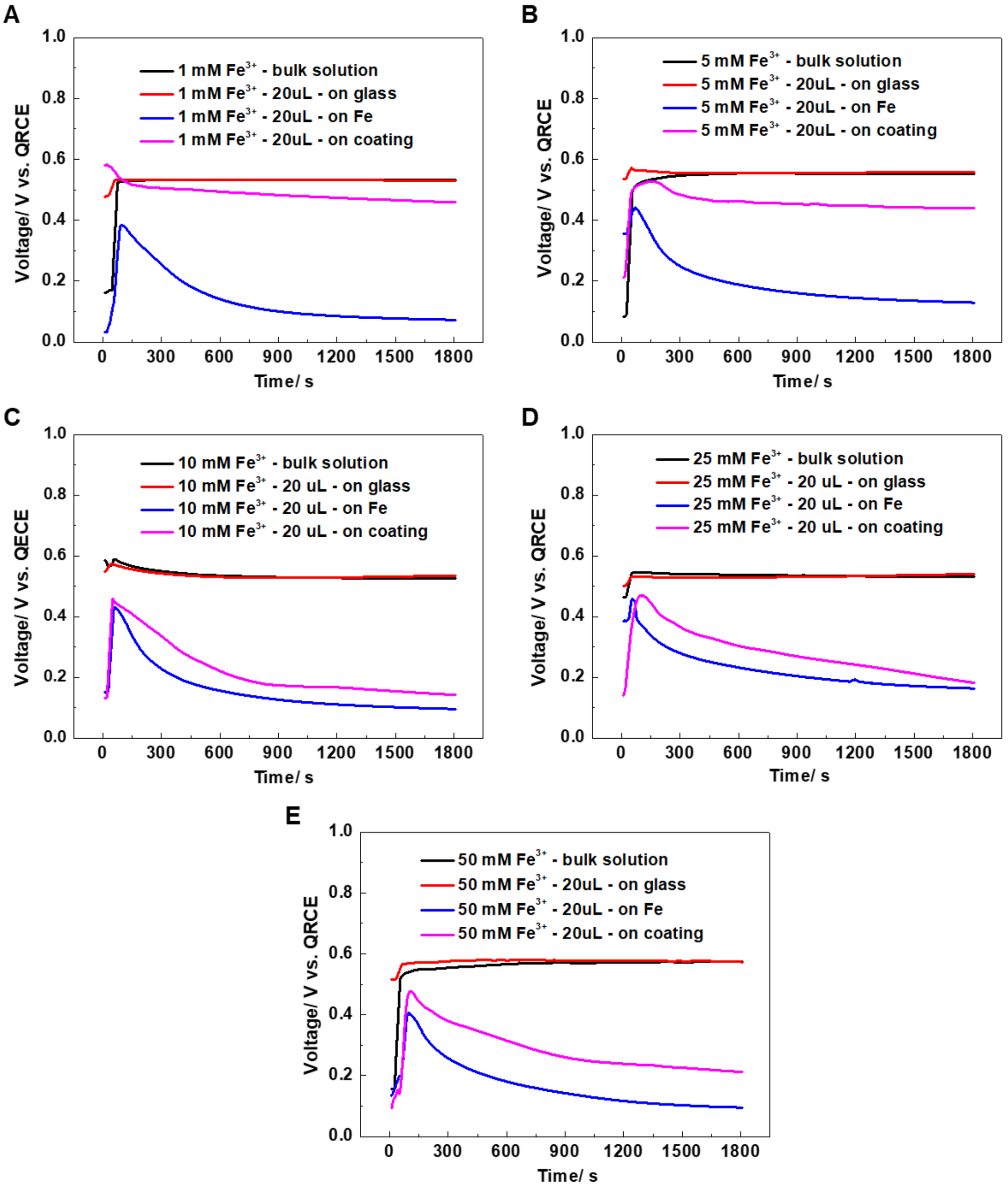

Figure 5.6 OCP measurements of different concentration of Fe^{3+} by integrated probe in bulk solution, 20 μL droplet on insulating glass, 20 μL droplet on Fe plate, and 20 μL droplet on Fe plate with silane coating. (A): 1 mM Fe^{3+}, (B): 5 mM Fe^{3+}, (C): 10 mM Fe^{3+}, (D): 25 mM Fe^{3+}, (E): 50 mM Fe^{3+}.

5.3.3 Anodic stripping voltammetry in H_2SO_4 droplet on Cu plate

As shown in **Figure 5.5**, the integrated probe can also be used for voltametric analysis by connecting the Ag/AgCl as both RE and CE. This is further extended to droplet analysis in the form of stripping voltammetry. Stripping voltammetry is a powerful electrochemical measurement for analyzing low concentration of species. With a preconcentration step, the detection limit can reach nM range[263,264], and it is ideal for electroanalysis of metal ions via electrodeposition followed by anodic stripping[265–268]. The electrode is naturally renewed after stripping, thus it can be used to monitor the change of metal ion concentration in a droplet during the corrosion process[269].

Here, we demonstrate a model system that mimics atmospheric corrosion of Cu in acidic spray. 20 μL of 0.1 M H_2SO_4 is dropped on Cu substrate, and the dissolution of Cu is followed by anodic stripping analysis of Cu^{2+} concentration in the droplet using the integrated probe. **Figure 5.7A** shows the anodic stripping signals at different time measured in-situ in the H_2SO_4 droplet from the integrated probe. For each measurement, the integrated probe is pre-conditioned at –0.2 V (Pt WE *vs.* Ag/AgCl RE/CE) for 30 s for pre-concentration, and then CV was performed from –0.08 to 0.6 V (Pt WE *vs.* Ag/AgCl QRE/CE) for stripping Cu. It is seen that the area of the stripping peak increases as a function of time, which indicates the corrosion of Cu in the H_2SO_4 droplet. As the charge of Cu stripping is linear with the concentration of Cu^{2+} (calibration curve in **Figure 5.7B**), one may derive the variation of Cu^{2+} concentration in the droplet, as shown in **Figure 5.7C**. It is clearly seen that the signal is low in the first 25 minutes, and afterwards it increases with time. Considering that it takes less than 5 minutes for Cu^{2+} ions to diffuse from the substrate to the top of the droplet (same estimation as in **5.3.4**, and even less time expected due to the pre-concentration that facilitates the diffusion), this phenomenon cannot be only attributed to the lag of detection. According to Mattsson and Bockris[270] and other research workers[271,272], the anodic dissolution of copper takes place through two consecutive steps:

$Cu_s - e^- = Cu(I)_{ads}$ (fast step) (R3)

$Cu(I)_{ads} - e^- = Cu(II)_{sol}$ (the rate-determining step) (R4)

R3 is called incubation period, where the corrosion yields adsorbed Cu(I) species that do not dissolve in the solution[273]. This may explain the low concentration of Cu^{2+} analyzed from the droplet at the initial stage of corrosion. Later, due to the fast kinetics of R4, the Cu^{2+} concentration increases rapidly and can be followed by anodic stripping voltammetry.

The chemical analysis of the corrosion product in corrosive media is often used for evaluating the corrosion rate, which is a key characteristic for metallic structures. As compared with classical chemical analysis such as ion chromatography[274,275] and inductively coupled plasma atomic emission spectroscopy[276], the integrated probe does not consume the sample and requires only very small volume so that it has merits in in-situ measurements as demonstrated in **Figure 5.2**. The corrosion rate is often expressed as weight loss of the metal per time. In the case of H_2SO_4 droplet on Cu, the weight loss of Cu turns into Cu^{2+} ions in the droplet, thus it can be derived from the following equation:

$$Corrosion\,rate = \frac{V_{droplet}}{\rho_{Cu}A} \cdot \frac{d[\mathrm{Cu}^{2+}]}{dt} \quad \textbf{(Equation 5.4)}$$

where ρ_{Cu} is the density of Cu metal, A is the wetted area of the droplet, $V_{droplet}$ is the volume of the droplet. The corrosion rate is in the unit of thickness per time (μm/min), which can be calculated from the time derivative of **Figure 5.7C**. This simple calculation does not take into account the formation of Cu(I), but it could still qualitatively reflect the corrosion behavior. The results are shown in **Figure 5.7D**. Note that two different areas of the substrate are tested. The trend of corrosion is similar, but the exact rate is different. This is probably due to the inhomogeneity of the surface, which may sensitively affect the initial stage of corrosion. In another word, it suggests that the integrated probe may offer the possibility to evaluate the local corrosion rate in atmospheric corrosion.

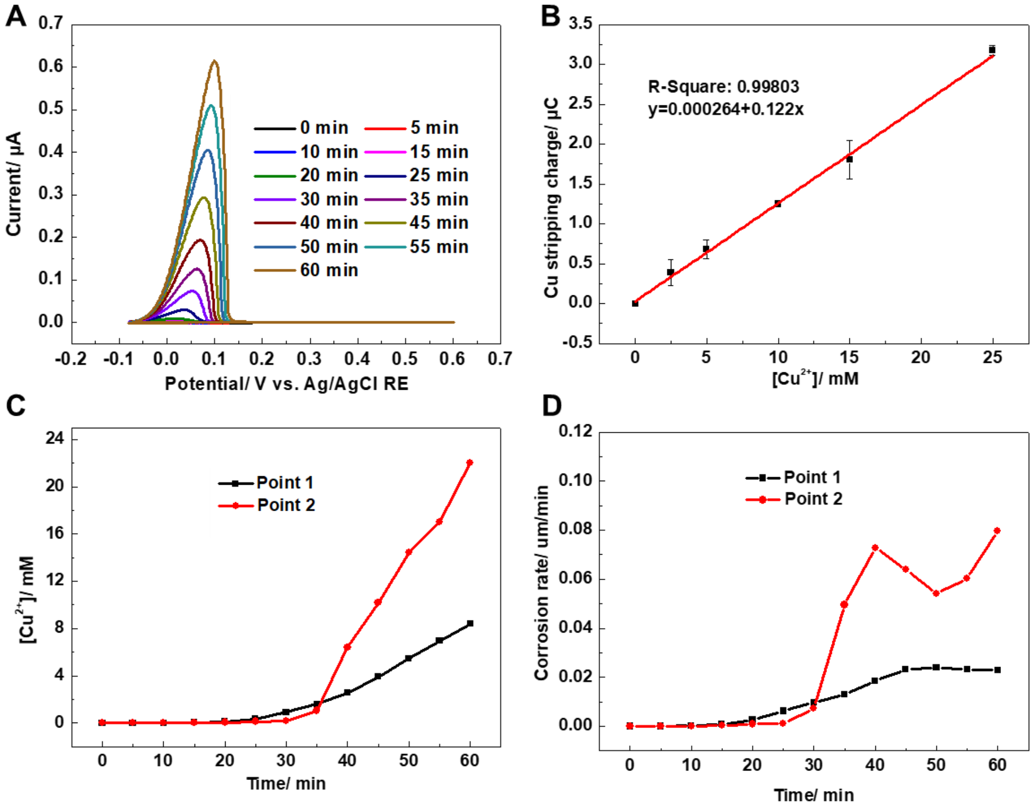

Figure 5.7 Anodic stripping signals of Cu measured in 20 µL 0.1 M H_2SO_4 droplet on Cu plate at different time with interval of 5 min (A), calibration curve of Cu stripping charge *vs.* concentration by the integrated probe in Cu^{2+} bulk solutions (B), $[Cu^{2+}]$ in the droplet as the function of time (C), the corrosion rate of Cu in µm/min, calculated with ρ_{Cu} = 8.89 g/cm^3 and A ≈ 0.28 cm^2 (D).

5.3.4 Attempt to prepare gel-coated integrated probe

For carrying out the local electrochemical analysis in SGECM with three-electrode configuration, the gel probe is fabricated based on the integrated probe. Coating the gel on the entire integrated electrode is challenging because the gel is not easy to be deposited in the gap between gel probe and capillary. Once, the gap is covered with gel, the physical resolution of the gel probe will be worse. Therefore, the gel deposited on the bare micro-disk electrode. Afterwards, the inner gel probe is inserted into outer capillary filled with electrolyte. Here, the inner gel probe is fabricated by the anodic deposition of the gel on Au micro-disk electrode with diameter of 25 µm. The method for preparing the bare Au micro-disk electrode is same with the Pt and Ag micro-disk electrodes in **Chapter II** and **Chapter III**. The solutions and parameters for the gel deposition is same with the **Appendix I**. The gel probe for constructing three-electrodes system is assembled by inserting the normal gel probe into the capillary filled with 0.1M NaCl. The image of final gel probe is shown in **Figure 5.10A**. Because the hydrogel is buffered with the electrolyte, the gel is not shrinking. After approaching this gel probe on a Pt plate with current feedback, cyclic voltammetry is carried out as shown in **Figure 5.10A**. The Pt plate is WE, Pt microelectrode is CE and the Ag/AgCl is RE. The hydrogen evolution peak could be clearly observed at –0.4 V (*vs.* Ag/AgCl) on the Pt plate. This shows the possibility of this gel probe in local electrochemical analysis by SGECM. The advantages of the gel probe based on the integrated probe might be:

(1) The potential applied on the sample could be measured relying on the three-electrodes system.
(2) The electrolyte in capillary is enough to eliminate the influence of the electrolyte evaporation to the analysis.
(3) The glycerol is not necessary in the solvent, which simplify the quantitative analysis.
(4) The physical resolution should be similar with the normal gel probe fabricated with the bare micro-disk electrode.
(5) The approaching of the probe could be carried out by the AC signal.

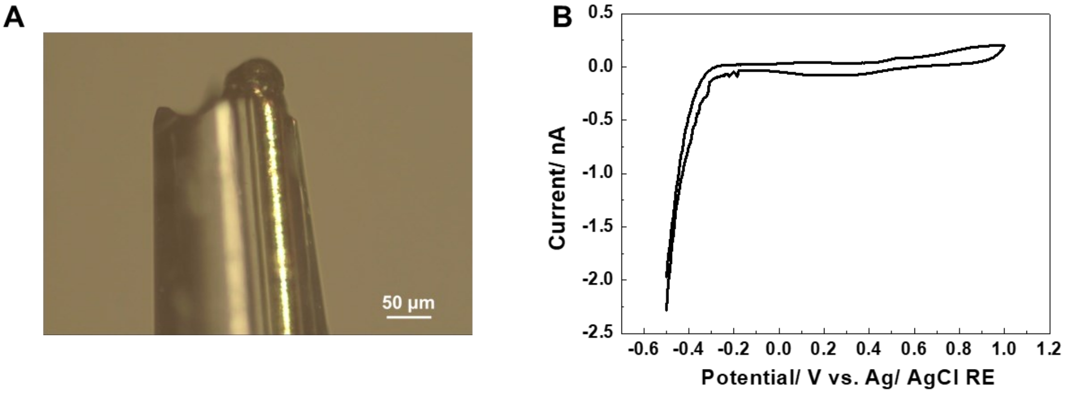

Figure 5.10 Image of the gel probe for SGECM based on the bare integrated probe (A). Cyclic voltammograms of the gel probe on the Pt plate (B).

5.4 Summary

In conclusion, an integrated probe is developed for the electrochemical analysis in small volume droplets. The integrated probe consists of Pt microelectrode, Ag/AgCl wire fixed on the shield of the microelectrode, and external capillary soaked with electrolyte. With the designed holder, the probe is prepared and refreshed easily. The ohmic drop, capability and reproducibility of potentiometric and voltammetric measurements are systematically characterized. In the results, the negligible ohmic drop of the integrated probe is demonstrated. For this reason, the probe works well in potentiometric and voltammetric detection. Furthermore, the electrochemical analysis in small volume droplets by the integrated probe is achieved. The reaction of Fe^{3+}/Fe is recorded through potentiometric method. Moreover, H_2SO_4/Cu is measured by anodic stripping method. Electrodeposition of chitosan is carried out on the inner micro-disk electrode, and then the electrode is inserted into an outer capillary forming integrated gel probe. Cyclic voltametric analysis on a Pt plate could be carried out and the potential. Clearly, the fabrication of integrated gel probe has to be further explored, but the preliminary results are optimistic for using integrated gel probes in local electrochemical analysis with SGECM.

General conclusion

Scanning gel electrochemical microscopy (SGECM) is a novel scanning electrochemical probe technique for local electrochemical analysis. The concept is based on a gel probe that is in soft contact with the sample surface, allowing local electrochemical measurements to be performed at the gel/sample interface with the confined gel electrolyte. This thesis is devoted to the development of SGECM for more quantitative analysis, better reliability, and new operational modes.

The most important character of SGECM is the lateral physical resolution, which depends on the shape of gel probe as well as the control of approaching. The electrodeposition of chitosan on micro-disk electrode is optimized to reproducibly fabricate gel probes. These gel probes are approached to the sample surface by either shear force or current feedback, and the lateral physical resolution is quantitatively analyzed by marking the contact area of a single pixel and the line scan of periodically shaped reference samples. The results show an important feature of flexible resolution due to the soft nature of the hydrogel. For the probe fabricated by electrodepositing chitosan on a 25 μm Pt disk electrode with $R_g \approx 2$, the lateral physical resolution at touching position is *ca.* 50 μm for current feedback and *ca.* 63 μm for shear force feedback. After pulling or pressing the gel probe for a certain distance after contacting with the sample, the resolution could be tuned from 14 to 78 μm. With the same gel probe, current feedback has higher lateral physical resolution than shear force feedback at touching position because it is more sensitive to the gel-sample contact. Therefore, current feedback is more favourable for conductive samples, but shear force feedback is more versatile especially for unknown partially conductive samples.

Potentiometric measurements of SGECM are achieved with the development of Ag/AgCl-gel micro-reference electrode. The electrodes are prepared by electrodeposition of chitosan hydrogel on Ag micro-disk electrodes followed by Ag chlorination. They are approached to the sample by shear force feedback with the potential versus the sample recorded by a highly sensitive voltammeter. Topography and electrochemical potential of a model sample consisting of Cu tapes on Al plate are simultaneously mapped. The two metals were clearly identified from both topography and potential maps. Moreover, the potential is insensitive to the pressing of the gel, indicating that reliable potentiometric measurements can be conducted even without accurate control of the probe-sample distance.

As the gel probe undergoes thousands of pressing-stretching cycles during mapping, it is highly desired to improve the mechanical strength of the gel. Attempts have been made by a post-treatment of electrodeposited gel by glutaraldehyde, which serves as a chemical cross-linker. Results indicate that after cross-linking for 2 hours in 0.2% glutaraldehyde solution, the elastic modulus of hydrogel is clearly enhanced, while the diffusion coefficient of the redox couple in hydrogel does not obviously change.

Preliminary attempts have also been made for developing integrated gel probes for SGECM measurements in three-electrode system. First, an integrated probe consisting of Pt microelectrode, Ag/AgCl wire fixed on the shield of the microelectrode and external capillary soaked with electrolyte is developed. The integrated probe shows the capabilities of electroanalysis in small volume droplets by potentiometry of Fe^{3+}/Fe^{2+} from oxidation of Fe and anodic stripping of Cu^{2+} generated from Cu corrosion in H_2SO_4.

Overall, the thesis quantifies the lateral physical resolution of SGECM by shear force and current feedback and reveals an important feature of flexible resolution by controlling the vertical position of the gel probe after contacting sample surface, develops new Ag/AgCl-gel micro-reference electrodes towards potentiometric mode of SGECM, improves the mechanical strength of gel probes by cross-linking with glutaraldehyde, as well as attempts to develop integrated gel probes for SGECM measurements in three-electrode system.

Perspectives

In this thesis, several questions in terms of the gel probe characterization and improvement that we have no exact answers yet are:

1. Quantitative analysis of the elastic modulus of the hydrogel deposited on the micro-disk electrode. Both experimental and modeling parts should be further studied. (**Chapter IV**)
2. In-situ and quantitative analysis of the diffusion coefficient of the species in the gel probe. In **Chapter IV**, even though the diffusion coefficient of the redox couple in hydrogel could be quantitatively solved by immersing the gel probe in bulk solution and performing cyclical voltammetry, the in-situ tests by leaving the gel probe in air is still challenging. Till now, the experimental design might be ok for in-situ measurements, but the data analysis should be investigated based on a mathematic model with specific boundary conditions.
3. Systematical studying of the gel probe based on the integrated probe in SGECM. The approaching by AC current, IR drop of electrolyte between the capillary and the hydrogel, the evaporation of the electrolyte, the CV of single point on metal, *etc.* should be further explored. (**Chapter V**)

For solving the question 1, a new force probe should be prepared by sticking an etched tungsten wire with a conical tip on commercial force probe with a silicon flap. Since the size of the hydrogel is much bigger than the conical tip, the deformation of the gel could be negligible. Thus, JKR and DMT models might works for fitting the data. For example, JKR model based on a conical probe (**Equation 1.7** and **Equation 1.8**) might useful. Of course, considering the viscoelastic properties and permeability of the hydrogel, more experiments should be designed to test the modules of hydrogel[277]. Instead of analyzing the force versus displacement, the force on the indenter as a function of time F(t) will be record. The data could be analyzed based on the existing model and the shear modulus and the Poisson's ratio could be solved[254,278].

For solving the question 2, the new mathematic model should be used for fitting the data. The redox couples on micro-disk electrode in bulk solution follows the semi-spherical diffusion. One boundary condition used for solving the semi-spherical diffusion is that assuming the concentration of the redox couple is a constant value at where far from the micro-disk electrode. However, this boundary condition is not suitable for solving the redox reactions in gel probe. Because the limited gel size cannot be considered as the bulk solution. Then for solving the diffusion equation, new boundary condition should be applied for the gel probe. The geometry of the gel probe (especially after touching with the sample surface) and the diffusion layer thickness ($\delta = \sqrt{\pi D t}$) should be considered.

Comparing question 1 and 2, solving question 3 is more about the instrumentation and experimental operation. The AC signal detection will be similar with the SECCM AC approaching. The oscillation of piezoelectric positioner could be modulated and the probe is vibrated in z axis. The AC current between the Pt micro-disk electrode and the inner reference electrode could be identified and stop the movement of the probe. Similar with the integrated probe, the IR drop of the electrode could be evaluated by the resistance obtained from EIS. For the gel probe, the EIS might be tested by the same configuration with **Figure 5.3A** but immersing the gel probe into bulk solution. Approaching gel probe soaked with NaCl on a metal plate (Ag, Cu, Fe, *etc.*), the CV could be applied to study the reactions. Or soaking the redox mediator in gel probe and scanning CV between inner Pt microelectrode and inner reference electrode, the reaction of samples could be monitored by using the redox couple as mediators.

Development of new operation modes/measurements of SGECM:

Force is a versatile method for approaching the probe. Combination of the force with SGECM, the electrochemical and force detection might be achieved simultaneously on the sample surface. The gel probe could be prepared based on deposition of the hydrogel on the tungsten force probe (discussed above), the probe could be approached by the force feedback in micro-force setup. And the electrochemical reaction could be applied through a potentiostat. For monitoring the force, position, and the electrochemical signal with the same time scale, the software of the microforce setup should be modified based on the LABVIEW. With this setup, the deformation of the gel during the measurements in SGECM could also be studied by the approach and retract curves on a model sample (like well-polished Pt plate).

Expanding applications of SGECM in corrosion:

For the corrosion analysis, SGECM shows attractive advantages and huge potential. First, the characterization is operated in air. The corrosion of the active sample surface could be tested in-situ and the sample surface is always fresh for testing. Second, the leakage of the electrolyte is controlled. Then the crystals caused by the electrolyte evaporation will not affect the corrosion reaction. So, the SGECM should be powerful for locally analyzing the corrosion behavior. For example, it’s reported that the grain of the as-cast Mg could be refined from 800-1500 μm to 50-100 μm by process-equal-channel-angular-pressing[279]. The grain refinement generates more crystalline defects, resulting in the enhanced strength and weak corrosion resistance. Classical EIS and polarization curves can only provide the information about entire sample surface. For further understanding the mechanism of grain corrosion, and evaluating the effect of grain size to corrosion resistance, local analysis might be informative and meaningful. By soaking NaCl solutions in gel probe in SGECM, the samples with or without grain refinement could be mapped by OCP and polarization curves. The different corrosion behavior could be compared and evaluated.

References

(1) Astruc, D. Introduction: Nanoparticles in Catalysis. *Chem. Rev.* **2020**, *120* (2), 461–463.

(2) Hosaka, T.; Kubota, K.; Hameed, A. S.; Komaba, S. Research Development on K-Ion Batteries. *Chem. Rev.* **2020**, *120*, 6358–6466.

(3) Duchêne, L.; Remhof, A.; Hagemann, H.; Battaglia, C. Status and Prospects of Hydroborate Electrolytes for All-Solid-State Batteries. *Energy Storage Mater.* **2020**, *25*, 782–794.

(4) Farag, A. A. Applications of Nanomaterials in Corrosion Protection Coatings and Inhibitors. *Corros. Rev.* **2020**, *38* (1), 67–86.

(5) Isaacson, B. M.; Bloebaum, R. D. Bone Bioelectricity: What Have We Learned in the Past 160 Years? *J. Biomed. Mater. Res. - Part A* **2010**, *95* (4), 1270–1279.

(6) Rahimnejad, M.; Adhami, A.; Darvari, S.; Zirepour, A.; Oh, S. E. Microbial Fuel Cell as New Technol Ogy for Bioelectricity Generation: A Review. *Alexandria Eng. J.* **2015**, *54* (3), 745–756.

(7) Suprun, E. V.; Shumyantseva, V. V.; Archakov, A. I. Protein Electrochemistry: Application in Medicine. A Review. *Electrochim. Acta* **2014**, *140*, 72–82.

(8) Matyushov, D. V. Dynamical Effects in Protein Electrochemistry. *J. Phys. Chem. B* **2019**, *123* (34), 7290–7301.

(9) Ozawa, F.; Ino, K.; Shiku, H.; Matsue, T. Electrochemical Hydrogel Lithography of Calcium-Alginate Hydrogels for Cell Culture. *Materials (Basel).* **2016**, *9* (9), 1–7.

(10) Jönsson, M.; Thierry, D.; LeBozec, N. The Influence of Microstructure on the Corrosion Behaviour of AZ91D Studied by Scanning Kelvin Probe Force Microscopy and Scanning Kelvin Probe. *Corros. Sci.* **2006**, *48* (5), 1193–1208.

(11) Fang, C.; Huang, Y.; Zhang, W.; Han, J.; Deng, Z.; Cao, Y.; Yang, H. Routes to High Energy Cathodes of Sodium-Ion Batteries. *Adv. Energy Mater.* **2016**, *6* (5).

(12) Wang, Y.; Zheng, R.; Luo, J.; Malik, H. A.; Wan, Z.; Jia, C.; Weng, X.; Xie, J.;

Deng, L.; Yao, X. Self-Healing Dynamically Cross Linked Versatile Polymer Electrolyte: A Novel Approach towards High Performance, Flexible Electrochromic Devices. *Electrochim. Acta* **2019**, *320*, 134489.

(13) Hou, H.; Vacandio, F.; Vona, M. L. Di; Knauth, P. Sulfonated Polyphenyl Ether by Electropolymerization. *Electrochim. Acta* **2012**, *81*, 58–63.

(14) Walcarius, A.; Minteer, S. D.; Wang, J.; Lin, Y.; Merkoçi, A. Nanomaterials for Bio-Functionalized Electrodes: Recent Trends. *J. Mater. Chem. B* **2013**, *1* (38), 4878–4908.

(15) Huanga, V. M.; Wua, S. L.; Orazema, M. E.; Pébère, N.; Tribollet, B.; Vivier, V. Local Electrochemical Impedance Spectroscopy: A Review and Some Recent Developments. *Electrochim. Acta* **2011**, *56*, 8048–8057.

(16) Gharbi, O.; Ngo, K.; Turmine, M.; Vivier, V. Local Electrochemical Impedance Spectroscopy: A Window into Heterogeneous Interfaces. *Curr. Opin. Electrochem.* **2020**, *20*, 1–7.

(17) Liu, L.; Etienne, M.; Walcarius, A. Scanning Gel Electrochemical Microscopy for Topography and Electrochemical Imaging. *Anal. Chem.* **2018**, *90* (15), 8889–8895.

(18) Polcari, D.; Dauphin-Ducharme, P.; Mauzeroll, J. Scanning Electrochemical Microscopy: A Comprehensive Review of Experimental Parameters from 1989 to 2015. *Chem. Rev.* **2016**, *116* (22), 13234–13278.

(19) Bard, A. J.; Fan, F. R. F.; Kwak, J.; Lev, O. Scanning Electrochemical Microscopy. Introduction and Principles. *Anal. Chem.* **1989**, *61* (2), 132–138.

(20) Engstrom, R. C.; Pharr, C. M. Scanning Electrochemical Microscopy. *Anal. Chem.* **1989**, *61* (19), 1099A-1104A.

(21) Danis, L.; Polcari, D.; Kwan, A.; Gateman, S. M.; Mauzeroll, J. Fabrication of Carbon, Gold, Platinum, Silver, and Mercury Ultramicroelectrodes with Controlled Geometry. *Anal. Chem.* **2015**, *87* (5), 2565–2569.

(22) Fernández, J. L.; Walsh, D. A.; Bard, A. J. Thermodynamic Guidelines for the Design of Bimetallic Catalysts for Oxygen Electroreduction and Rapid Screening by Scanning Electrochemical Microscopy. M-Co (M: Pd, Ag, Au). *J.*

Am. Chem. Soc. **2005**, *127* (1), 357–365.

(23) Eckhard, K.; Schuhmann, W. Localised Visualisation of O_2 Consumption and H_2O_2 Formation by Means of SECM for the Characterisation of Fuel Cell Catalyst Activity. *Electrochim. Acta* **2007**, *53*, 1164–1169.

(24) Jamali, S. S.; Moulton, S. E.; Tallman, D. E.; Forsyth, M.; Weber, J.; Wallace, G. G. Applications of Scanning Electrochemical Microscopy (SECM) for Local Characterization of AZ31 Surface during Corrosion in a Buffered Media. *Corros. Sci.* **2014**, *86*, 93–100.

(25) Matysiak, E.; Botz, A. J. R.; Clausmeyer, J.; Wagner, B.; Schuhmann, W.; Stojek, Z.; Nowicka, A. M. Assembling Paramagnetic Ceruloplasmin at Electrode Surfaces Covered with Ferromagnetic Nanoparticles. Scanning Electrochemical Microscopy in the Presence of a Magnetic Field. *Langmuir* **2015**, *31* (29), 8176–8183.

(26) Eckhard, K.; Chen, X.; Turcu, F.; Schuhmann, W. Redox Competition Mode of Scanning Electrochemical Microscopy (RC-SECM) for Visualisation of Local Catalytic Activity. *Phys. Chem. Chem. Phys.* **2006**, *8* (45), 5359–5365.

(27) Santana, J. J.; González-Guzmán, J.; Fernández-Mérida, L.; González, S.; Souto, R. M. Visualization of Local Degradation Processes in Coated Metals by Means of Scanning Electrochemical Microscopy in the Redox Competition Mode. *Electrochim. Acta* **2010**, *55* (15), 4488–4494.

(28) Bard, A. J.; Mirkin, M. V. *Scanning Electrochemical Microscopy, Second Edition*; 2012.

(29) Liu, L.; Toledano, R.; Danieli, T.; Zhang, J. Q.; Hu, J. M.; Mandler, D. Electrochemically Patterning Sol-Gel Structures on Conducting and Insulating Surfaces. *Chem. Commun.* **2011**, *47* (24), 6909–6911.

(30) Liu, L.; Mandler, D. Patterning Carbon Nanotubes with Silane by Scanning Electrochemical Microscopy. *Electrochem. commun.* **2014**, *48*, 56–60.

(31) Kranz, C.; Gaub, H. E.; Schuhmann, W. Polypyrrole Towers Grown with the Scanning Electrochemical Microscope. *Adv. Mater.* **1996**, *8* (8), 634–637.

(32) Denuault, G.; Frank, M. H. T.; Peter, L. M. Scanning Electrochemical

Microscopy: Potentiometric Probing of Ion Fluxes. *Faraday Discuss.* **1992**, *94*, 23–35.

(33) Serrapede, M.; Denuault, G.; Sosna, M.; Pesce, G. L.; Ball, R. J. Scanning Electrochemical Microscopy: Using the Potentiometric Mode of SECM to Study the Mixed Potential Arising from Two Independent Redox Processes. *Anal. Chem.* **2013**, *85* (17), 8341–8346.

(34) Ludwig, M.; Kranz, C.; Schuhmann, W.; Gaub, H. E. Topography Feedback Mechanism for the Scanning Electrochemical Microscope Based on Hydrodynamic Forces between Tip and Sample. *Rev. Sci. Instrum.* **1995**, *66* (4), 2857–2860.

(35) Etienne, M.; Schulte, A.; Mann, S.; Jordan, G.; Dietzel, I. D.; Schuhmann, W. Constant-Distance Mode Scanning Potentiometry. 1. Visualization of Calcium Carbonate Dissolution in Aqueous Solution. *Anal. Chem.* **2004**, *76* (13), 3682–3688.

(36) Etienne, M.; Lhenry, S.; Cornut, R.; Lefrou, C. Optimization of the Shearforce Signal for Scanning Electrochemical Microscopy and Application for Kinetic Analysis. *Electrochim. Acta* **2013**, *88*, 877–884.

(37) Etienne, M.; Dossot, M.; Grausem, J.; Herzog, G. Combined Raman Microspectrometer and Shearforce Regulated SECM for Corrosion and Self-Healing Analysis. *Anal. Chem.* **2014**, *86* (22), 11203–11210.

(38) Adam, C.; Kanoufi, F.; Sojic, N.; Etienne, M. Shearforce Positioning of Nanoprobe Electrode Arrays for Scanning Electrochemical Microscopy Experiments. *Electrochim. Acta* **2015**, *179*, 45–56.

(39) Etienne, M.; Layoussifi, B.; Giornelli, T.; Jacquet, D. SECM-Based Automate Equipped with a Shearforce Detection for the Characterization of Large and Complex Samples. *Electrochem. commun.* **2012**, *15* (1), 70–73.

(40) Nebel, M.; Erichsen, T.; Schuhmann, W. Constant-Distance Mode SECM as a Tool to Visualize Local Electrocatalytic Activity of Oxygen Reduction Catalysts. *Beilstein J. Nanotechnol.* **2014**, *5* (1), 141–151.

(41) Botz, A. J. R.; Nebel, M.; Rincón, R. A.; Ventosa, E.; Schuhmann, W. Onset

Potential Determination at Gas-Evolving Catalysts by Means of Constant-Distance Mode Positioning of Nanoelectrodes. *Electrochim. Acta* **2015**, *179*, 38–44.

(42) Eifert, A.; Mizaikoff, B.; Kranz, C. Advanced Fabrication Process for Combined Atomic Force-Scanning Electrochemical Microscopy (AFM-SECM) Probes. *Micron* **2015**, *68*, 27–35.

(43) Kottke, P. A.; Fedorov, A. G. Advective and Transient Effects in Combined AFM/SECM Operation. *J. Electroanal. Chem.* **2005**, *583* (2), 221–231.

(44) Knittel, P.; Zhang, H.; Kranz, C.; Wallace, G. G.; Higgins, M. J. Probing the PEDOT:PSS/Cell Interface with Conductive Colloidal Probe AFM-SECM. *Nanoscale* **2016**, *8* (8), 4475–4481.

(45) Kranz, C. Recent Advancements in Nanoelectrodes and Nanopipettes Used in Combined Scanning Electrochemical Microscopy Techniques. *Analyst* **2013**, *139* (2), 336–352.

(46) Macpherson, J. V.; Unwin, P. R. Combined Scanning Electrochemical-Atomic Force Microscopy. *Anal. Chem.* **2000**, *72* (2), 276–285.

(47) Macpherson, J. V.; Unwin, P. R. Noncontact Electrochemical Imaging with Combined Scanning Electrochemical Atomic Force Microscopy. *Anal. Chem.* **2001**, *73* (3), 550–557.

(48) Izquierdo, J.; Eifert, A.; Kranz, C.; Souto, R. M. In Situ Investigation of Copper Corrosion in Acidic Chloride Solution Using Atomic Force—Scanning Electrochemical Microscopy. *Electrochim. Acta* **2017**, *247*, 588–599.

(49) Chennit, K.; Trasobares, J.; Anne, A.; Cambril, E.; Chovin, A.; Clément, N.; Demaille, C. Electrochemical Imaging of Dense Molecular Nanoarrays. *Anal. Chem.* **2017**, *89* (20), 11061–11069.

(50) Kueng, A.; Kranz, C.; Lugstein, A.; Bertagnolli, E.; Mizaikoff, B. Integrated AFM-SECM in Tapping Mode: Simultaneous Topographical and Electrochemical Imaging of Enzyme Activity. *Angew. Chemie Int. Ed.* **2003**, *42* (28), 3238–3240.

(51) Frederix, P. L. T. M.; Bosshart, P. D.; Akiyama, T.; Chami, M.; Gullo, M. R.;

Blackstock, J. J.; Dooleweerdt, K.; De Rooij, N. F.; Staufer, U.; Engel, A. Conductive Supports for Combined AFM-SECM on Biological Membranes. *Nanotechnology* **2008**, *19* (38), 1–10.

(52) Tavert-Roudet, G.; Anne, A.; Barra, A.; Chovin, A.; Demaille, C.; Michon, T. The Potyvirus Particle Recruits the Plant Translation Initiation Factor Eif4e by Means of the Vpg Covalently Linked to the Viral RNA. *Mol. Plant-Microbe Interact.* **2017**, *30* (9), 754–762.

(53) Frey, C. M.; Eifert, A.; Schütz, H.; Barth, H.; Mizaikoff, B.; Kranz, C. Macroscopic and Microscopic Electrochemical Investigation of Clostridium Botulinum C2IIa Embedded in Supported Lipid Membranes. *Electrochim. Acta* **2016**, *209*, 341–349.

(54) Bentley, C. L.; Edmondson, J.; Meloni, G. N.; Perry, D.; Shkirskiy, V.; Unwin, P. R. Nanoscale Electrochemical Mapping. *Anal. Chem.* **2019**, *91* (1), 84–108.

(55) O’Connell, M. A.; Wain, A. J. Combined Electrochemical-Topographical Imaging: A Critical Review. *Anal. Methods* **2015**, *7* (17), 6983–6999.

(56) Dauphin-Ducharme, P.; Mauzeroll, J. Surface Analytical Methods Applied to Magnesium Corrosion. *Anal. Chem.* **2015**, *87* (15), 7499–7509.

(57) Niu, L.; Yin, Y.; Guo, W.; Lu, M.; Qin, R.; Chen, S. Application of Scanning Electrochemical Microscope in the Study of Corrosion of Metals. *J. Mater. Sci.* **2009**, *44* (17), 4511–4521.

(58) González-García, Y.; Santana, J. J.; González-Guzmán, J.; Izquierdo, J.; González, S.; Souto, R. M. Scanning Electrochemical Microscopy for the Investigation of Localized Degradation Processes in Coated Metals. *Prog. Org. Coatings* **2010**, *69* (2), 110–117.

(59) Souto, R. M.; González-García, Y.; González, S. Evaluation of the Corrosion Performance of Coil-Coated Steel Sheet as Studied by Scanning Electrochemical Microscopy. *Corros. Sci.* **2008**, *50* (6), 1637–1643.

(60) Souto, R. M.; González-Garciía, Y.; González, S. In Situ Monitoring of Electroactive Species by Using the Scanning Electrochemical Microscope. Application to the Investigation of Degradation Processes at Defective Coated

Metals. *Corros. Sci.* **2005**, *47* (12), 3312–3323.

(61) Zhang, Q.; Liu, P.; Zhu, Z.; Ye, Z.; Zhang, J.; Cao, F.; Li, X. Quantitative Analysis of the Polarization Behavior of Iron in an Aerated Acidic Solution Using SECM. *Electrochem. commun.* **2018**, *93*, 143–147.

(62) Jamali, S. S.; Moulton, S. E.; Tallman, D. E.; Zhao, Y.; Weber, J.; Wallace, G. G. Self-Healing Characteristic of Praseodymium Conversion Coating on AZNd Mg Alloy Studied by Scanning Electrochemical Microscopy. *Electrochem. commun.* **2017**, *76*, 6–9.

(63) Zhang, Q.; Ye, Z.; Zhu, Z.; Liu, X.; Zhang, J.; Cao, F. Separation and Kinetic Study of Iron Corrosion in Acidic Solution via a Modified Tip Generation/Substrate Collection Mode by SECM. *Corros. Sci.* **2018**, *139*, 403–409.

(64) Nazarov, V. A.; Taryba, M. G.; Zdrachek, E. A.; Andronchyk, K. A.; Egorov, V. V.; Lamaka, S. V. Sodium- and Chloride-Selective Microelectrodes Optimized for Corrosion Studies. *J. Electroanal. Chem.* **2013**, *706*, 13–24.

(65) Engstrom, R. C.; Pharr, C. M. Scanning Electrochemical Microscopy. *Analytical Chemistry*. 1989, pp 1099 A-1104 A.

(66) Asserghine, A.; Filotás, D.; Németh, B.; Nagy, L.; Nagy, G. Potentiometric Scanning Electrochemical Microscopy for Monitoring the PH Distribution during the Self-Healing of Passive Titanium Dioxide Layer on Titanium Dental Root Implant Exposed to Physiological Buffered (PBS) Medium. *Electrochem. commun.* **2018**, *95*, 1–4.

(67) Kiss, A.; Filotás, D.; Souto, R. M.; Nagy, G. The Effect of Electric Field on Potentiometric Scanning Electrochemical Microscopic Imaging. *Electrochem. commun.* **2017**, *77*, 138–141.

(68) Ramírez-Cano, J. A.; Veleva, L.; Souto, R. M.; Fernández-Pérez, B. M. SECM Study of the PH Distribution over Cu Samples Treated with 2-Mercaptobenzothiazole in NaCl Solution. *Electrochem. commun.* **2017**, *78*, 60–63.

(69) Filotás, D.; Fernández-Pérez, B. M.; Izquierdo, J.; Nagy, L.; Nagy, G.; Souto, R.

M. Combined Amperometric/Potentiometric Probes for Improved Chemical Imaging of Corroding Surfaces Using Scanning Electrochemical Microscopy. *Electrochim. Acta* **2016**, *221*, 48–55.

(70) Bastos, A. C.; Quevedo, M. C.; Karavai, O. V.; Ferreira, M. G. S. Review—On the Application of the Scanning Vibrating Electrode Technique (SVET) to Corrosion Research. *J. Electrochem. Soc.* **2017**, *164* (14), C973–C990.

(71) Tang, X.; Ran, C.; Orazem, M. E.; You, C.; Li, Y. Electrochimica Acta Local Electrochemical Characteristics of Pure Iron under a Saline Droplet II : Local Corrosion Kinetics. *Electrochim. Acta* **2020**, *354*, 136631.

(72) Botz, A.; Clausmeyer, J.; Öhl, D.; Tarnev, T.; Franzen, D.; Turek, T.; Schuhmann, W. Local Activities of Hydroxide and Water Determine the Operation of Silver-Based Oxygen Depolarized Cathodes. *Angew. Chemie Int. Ed.* **2018**, *57* (38), 12285–12289.

(73) Barforoush, J. M.; Jantz, D. T.; Seuferling, T. E.; Song, K. R.; Cummings, L. C.; Leonard, K. C. Microwave-Assisted Synthesis of a Nanoamorphous ($Ni_{0.8}$,$Fe_{0.2}$) Oxide Oxygen-Evolving Electrocatalyst Containing Only “Fast” Sites. *J. Mater. Chem. A* **2017**, *5* (23), 11661–11670.

(74) Dobrzeniecka, A.; Zeradjanin, A. R.; Masa, J.; Blicharska, M.; Wintrich, D.; Kulesza, P. J.; Schuhmann, W. Evaluation of Kinetic Constants on Porous, Non-Noble Catalyst Layers for Oxygen Reduction - A Comparative Study between SECM and Hydrodynamic Methods. *Catal. Today* **2016**, *262*, 74–81.

(75) Kim, J.; Renault, C.; Nioradze, N.; Arroyo-Currás, N.; Leonard, K. C.; Bard, A. J. Electrocatalytic Activity of Individual Pt Nanoparticles Studied by Nanoscale Scanning Electrochemical Microscopy. *J. Am. Chem. Soc.* **2016**, *138* (27), 8560–8568.

(76) Yuan, D.; Zhang, L.; Lai, J.; Xie, L.; Mao, B.; Zhan, D. SECM Evaluations of the Crystal-Facet-Correlated Photocatalytic Activity of Hematites for Water Splitting. *Electrochem. commun.* **2016**, *73*, 29–32.

(77) Chen, X.; Botz, A. J. R.; Masa, J.; Schuhmann, W. Characterisation of Bifunctional Electrocatalysts for Oxygen Reduction and Evolution by Means of

SECM. *J. Solid State Electrochem.* **2016**, *20* (4), 1019–1027.

(78) Liu, D.; Yu, Q.; Liu, S.; Qian, K.; Wang, S.; Sun, W.; Yang, X. Q.; Kang, F.; Li, B. Evolution of Solid Electrolyte Interface on TiO_2 Electrodes in an Aqueous Li-Ion Battery Studied Using Scanning Electrochemical Microscopy. *J. Phys. Chem. C* **2019**, *123* (20), 12797–12806.

(79) Yan, R.; Ghilane, J.; Phuah, K. C.; Pham Truong, T. N.; Adams, S.; Randriamahazaka, H.; Wang, Q. Determining Li^+-Coupled Redox Targeting Reaction Kinetics of Battery Materials with Scanning Electrochemical Microscopy. *J. Phys. Chem. Lett.* **2018**, *9* (3), 491–496.

(80) Ventosa, E.; Madej, E.; Zampardi, G.; Mei, B.; Weide, P.; Antoni, H.; La Mantia, F.; Muhler, M.; Schuhmann, W. Solid Electrolyte Interphase (SEI) at TiO_2 Electrodes in Li-Ion Batteries: Defining Apparent and Effective SEI Based on Evidence from X-Ay Photoemission Spectroscopy and Scanning Electrochemical Microscopy. *ACS Appl. Mater. Interfaces* **2017**, *9* (3), 3123–3130.

(81) Ventosa, E.; Wilde, P.; Zinn, A. H.; Trautmann, M.; Ludwig, A.; Schuhmann, W. Understanding Surface Reactivity of Si Electrodes in Li-Ion Batteries by: In Operando Scanning Electrochemical Microscopy. *Chem. Commun.* **2016**, *52* (41), 6825–6828.

(82) Martin, C. J.; Bozic-Weber, B.; Constable, E. C.; Glatzel, T.; Housecroft, C. E.; Wright, I. A. Development of Scanning Electrochemical Microscopy (SECM) Techniques for the Optimization of Dye Sensitized Solar Cells. *Electrochim. Acta* **2014**, *119*, 86–91.

(83) Schmidt, I.; Plettenberg, I.; Kimmich, D.; Ellis, H.; Witt, J.; Dosche, C.; Wittstock, G. Spatially Resolved Analysis of Screen Printed Photoanodes of Dye-Sensitized Solar Cells by Scanning Electrochemical Microscopy. *Electrochim. Acta* **2016**, *222*, 735–746.

(84) Bozic, B.; Figgemeier, E. Scanning Electrochemical Microscopy under Illumination: An Elegant Tool to Directly Determine the Mobility of Charge Carriers within Dye-Sensitized Nanostructured Semiconductors. *Chem.*

Commun. **2006**, No. 21, 2268–2270.

(85) Nicholson, P. G.; Zhou, S.; Hinds, G.; Wain, A. J.; Turnbull, A. Electrocatalytic Activity Mapping of Model Fuel Cell Catalyst Films Using Scanning Electrochemical Microscopy. *Electrochim. Acta* **2009**, *54* (19), 4525–4533.

(86) Fernández, J. L.; Bard, A. J. Scanning Electrochemical Microscopy. 47. Imaging Electrocatalytic Activity for Oxygen Reduction in an Acidic Medium by the Tip Generation - Substrate Collection Mode. *Anal. Chem.* **2003**, *75* (13), 2967–2974.

(87) Minguzzi, A.; Alpuche-Aviles, M. A.; López, J. R.; Rondinini, S.; Bard, A. J. Screening of Oxygen Evolution Electrocatalysts by Scanning Electrochemical Microscopy Using a Shielded Tip Approach. *Anal. Chem.* **2008**, *80* (11), 4055–4064.

(88) O'Connell, M. A.; Lewis, J. R.; Wain, A. J. Electrochemical Imaging of Hydrogen Peroxide Generation at Individual Gold Nanoparticles. *Chem. Commun.* **2015**, *51* (51), 10314–10317.

(89) Ahn, H. S.; Bard, A. J. Surface Interrogation of CoPi Water Oxidation Catalyst by Scanning Electrochemical Microscopy. *J. Am. Chem. Soc.* **2015**, *137* (2), 612–615.

(90) Li, F.; Ciani, I.; Bertoncello, P.; Unwin, P. R.; Zhao, J.; Bradbury, C. R.; Fermin, D. J. Scanning Electrochemical Microscopy of Redox-Mediated Hydrogen Evolution Catalyzed by Two-Dimensional Assemblies of Palladium Nanoparticles. *J. Phys. Chem. C* **2008**, *112* (26), 9686–9694.

(91) Dobrzeniecka, A.; Zeradjanin, A.; Masa, J.; Puschhof, A.; Stroka, J.; Kulesza, P. J.; Schuhmann, W. Application of SECM in Tracing of Hydrogen Peroxide at Multicomponent Non-Noble Electrocatalyst Films for the Oxygen Reduction Reaction. *Catal. Today* **2013**, *202* (1), 55–62.

(92) Huang, L.; Li, Z.; Lou, Y.; Cao, F.; Zhang, D.; Li, X. Recent Advances in Scanning Electrochemical Microscopy for Biological Applications. *Materials (Basel).* **2018**, *11* (8).

(93) Roberts, W. S.; Lonsdale, D. J.; Griffiths, J.; Higson, S. P. J. Advances in the Application of Scanning Electrochemical Microscopy to Bioanalytical Systems.

Biosens. Bioelectron. **2007**, *23* (3), 301–318.

(94) Pierce, D. T.; Unwin, P. R.; Bard, A. J. Scanning Electrochemical Microscopy. 17. Studies of Enzyme-Mediator Kinetics for Membrane- and Surface-Immobilized Glucose Oxidase. *Anal. Chem.* **1992**, *64* (17), 1795–1804.

(95) Shiku, H.; Takeda, T.; Yamada, H.; Matsue, T.; Uchida, I. Microfabrication and Characterization of Diaphorase-Patterned Surfaces by Scanning Electrochemical Microscopy. *Anal. Chem.* **1995**, *67* (2), 312–317.

(96) Yamada, H.; Fukumoto, H.; Yokoyama, T.; Koike, T. Immobilized Diaphorase Surfaces Observed by Scanning Electrochemical Microscope with Shear Force Based Tip-Substrate Positioning. *Anal. Chem.* **2005**, *77* (6), 1785–1790.

(97) Shiku, H.; Hara, Y.; Matsue, T.; Uchida, I.; Yamauchi, T. Dual Immunoassay of Human Chorionic Gonadotropin and Human Placental Lactogen at a Miocrofabricated Substrate by Scanning Electrochemical Microscopy. *J. Electroanal. Chem.* **1997**, *438* (1–2), 187–190.

(98) Lei, R.; Stratmann, L.; Schäfer, D.; Erichsen, T.; Neugebauer, S.; Li, N.; Schuhmann, W. Imaging Biocatalytic Activity of Enzyme-Polymer Spots by Means of Combined Scanning Electrochemical Microscopy/Electrogenerated Chemiluminescence. *Anal. Chem.* **2009**, *81* (12), 5070–5074.

(99) Zhao, C.; Wittstock, G. Scanning Electrochemical Microscopy of Quinoprotein Glucose Dehydrogenase. *Anal. Chem.* **2004**, *76* (11), 3145–3154.

(100) Gunawan, C. A.; Nam, E. V.; Marquis, C. P.; Gooding, J. J.; Thordarson, P.; Zhao, C. Scanning Electrochemical Microscopy of Cytochrome c Peroxidase through the Orientation-Controlled Immobilisation of Cytochrome C. *ChemElectroChem* **2016**, *3* (7), 1150–1156.

(101) Li, L.; Bu, C.; Zhang, Y.; Du, J.; Lu, X.; Liu, X. Composite System Based on Biomolecules-Functionalized Multiwalled Carbon Nanotube and Ionic Liquid: Electrochemistry and Electrocatalysis of Tryptophane. *Electrochim. Acta* **2011**, *58* (1), 105–111.

(102) Alizadeh, V.; Mousavi, M. F.; Mehrgardi, M. A.; Kazemi, S. H.; Sharghi, H. Electron Transfer Kinetics of Cytochrome c Immobilized on a Phenolic

Terminated Thiol Self Assembled Monolayer Determined by Scanning Electrochemical Microscopy. *Electrochim. Acta* **2011**, *56* (17), 6224–6229.

(103) Alizadeh, V.; Mehrgardi, M. A.; Fazlollah Mousavi, M. Electrochemical Investigation of Cytochrome c Immobilized onto Self-Assembled Monolayer of Captopril. *Electroanalysis* **2013**, *25* (7), 1689–1696.

(104) Song, W.; Yan, Z.; Hu, K. Electrochemical Immunoassay for CD10 Antigen Using Scanning Electrochemical Microscopy. *Biosens. Bioelectron.* **2012**, *38* (1), 425–429.

(105) Kasai, S.; Yokota, A.; Zhou, H.; Nishizawa, M.; Niwa, K.; Onouchi, T.; Matsue, T. Immunoassay of the MRSA-Related Toxic Protein, Leukocidin, with Scanning Electrochemical Microscopy. *Anal. Chem.* **2000**, *72* (23), 5761–5765.

(106) Abdelhamid, M. E.; Piantavigna, S.; Bond, A. M.; Graham, B.; Spiccia, L.; Martin, L. L.; O'Mullane, A. P. An SECM Study on the Influence of Cationic, Membrane-Active Peptides on a Gold-Supported Self-Assembled Monolayer. *Electrochem. commun.* **2015**, *51*, 11–14.

(107) Piantavigna, S.; Abdelhamid, M. E.; Zhao, C.; Qu, X.; McCubbin, G. A.; Graham, B.; Spiccia, L.; O'Mullane, A. P.; Martin, L. L. Mechanistic Details of the Membrane Perforation and Passive Translocation of TAT Peptides. *Chempluschem* **2015**, *80* (1), 83–90.

(108) She, Z.; Topping, K.; Shamsi, M. H.; Wang, N.; Chan, N. W. C.; Kraatz, H. B. Investigation of the Utility of Complementary Electrochemical Detection Techniques to Examine the in Vitro Affinity of Bacterial Flagellins for a Toll-like Receptor 5 Biosensor. *Anal. Chem.* **2015**, *87* (8), 4218–4224.

(109) Yasukawa, T.; Hirano, Y.; Motochi, N.; Shiku, H.; Matsue, T. Enzyme Immunosensing of Pepsinogens 1 and 2 by Scanning Electrochemical Microscopy. *Biosens. Bioelectron.* **2007**, *22* (12), 3099–3104.

(110) Ning, X.; Xiong, Q.; Zhang, F.; He, P. Simultaneous Detection of Tumor Markers in Lung Cancer Using Scanning Electrochemical Microscopy. *J. Electroanal. Chem.* **2018**, *812*, 101–106.

(111) Yamashita, K.; Takagi, M.; Uchida, K.; Kondo, H.; Takenaka, S. Visualization

of DNA Microarrays by Scanning Electrochemical Microscopy (SECM). *Analyst* **2001**, *126* (8), 1210–1211.

(112) Shamsi, M. H.; Kraatz, H. B. Probing Nucleobase Mismatch Variations by Electrochemical Techniques: Exploring the Effects of Position and Nature of the Single-Nucleotide Mismatch. *Analyst* **2010**, *135* (9), 2280–2285.

(113) Zhao, X.; Lam, S.; Jass, J.; Ding, Z. Scanning Electrochemical Microscopy of Single Human Urinary Bladder Cells Using Reactive Oxygen Species as Probe of Inflammatory Response. *Electrochem. commun.* **2010**, *12* (6), 773–776.

(114) Kikuchi, H.; Prasad, A.; Matsuoka, R.; Aoyagi, S.; Matsue, T.; Kasai, S. Scanning Electrochemical Microscopy Imaging during Respiratory Burst in Human Cell. *Front. Physiol.* **2016**, *7*, 1–6.

(115) Ktari, N.; Poncet, P.; Sénéchal, H.; Malaquin, L.; Kanoufi, F.; Combellas, C. Patterning of Polystyrene by Scanning Electrochemical Microscopy. Biological Applications to Cell Adhesion. *Langmuir* **2010**, *26* (22), 17348–17356.

(116) Bergner, S.; Palatzky, P.; Wegener, J.; Matysik, F. M. High-Resolution Imaging of Nanostructured Si/SiO_2 Substrates and Cell Monolayers Using Scanning Electrochemical Microscopy. *Electroanalysis* **2011**, *23* (1), 196–200.

(117) Shiku, H.; Shiraishi, T.; Aoyagi, S.; Utsumi, Y.; Matsudaira, M.; Abe, H.; Hoshi, H.; Kasai, S.; Ohya, H.; Matsue, T. Respiration Activity of Single Bovine Embryos Entrapped in a Cone-Shaped Microwell Monitored by Scanning Electrochemical Microscopy. *Anal. Chim. Acta* **2004**, *522* (1), 51–58.

(118) Chen, C.-C.; Zhou, Y.; Baker, L. A. Scanning Ion Conductance Microscopy. *Annu. Rev. Anal. Chem.* **2012**, *5* (1), 207–228.

(119) P. K. Hansma, B. Drake, O. Marti, S. A. C. Gould, C. B. P. The Scanning Ion-Conductance Microscope. *Science* **1987**, *243*, 641–643.

(120) Li, C.; Johnson, N.; Ostanin, V.; Shevchuk, A.; Ying, L.; Korchev, Y.; Klenerman, D. High Resolution Imaging Using Scanning Ion Conductance Microscopy with Improved Distance Feedback Control. *Prog. Nat. Sci.* **2008**, *18* (6), 671–677.

(121) Proksch, R.; Lal, R.; Hansma, P. K.; Morse, D.; Stucky, G. Imaging the Internal

and External Pore Structure of Membranes in Fluid: TappingMode Scanning Ion Conductance Microscopy. *Biophys. J.* **1996**, *71* (4), 2155–2157.

(122) Korchev, Y. E.; Raval, M.; Lab, M. J.; Gorelik, J.; Edwards, C. R. W.; Rayment, T.; Klenerman, D. Hybrid Scanning Ion Conductance and Scanning Near-Field Optical Microscopy for the Study of Living Cells. *Biophys. J.* **2000**, *78* (5), 2675–2679.

(123) Takahashi, Y.; Shevchuk, A. I.; Novak, P.; Murakami, Y.; Shiku, H.; Korchev, Y. E.; Matsue, T. Simultaneous Noncontact Topography and Electrochemical Imaging by SECM/SICM Featuring Ion Current Feedback Regulation. *J. Am. Chem. Soc.* **2010**, *132* (29), 10118–10126.

(124) Takahashi, Y.; Shevchuk, A. I.; Novak, P.; Zhang, Y.; Ebejer, N.; MacPherson, J. V.; Unwin, P. R.; Pollard, A. J.; Roy, D.; Clifford, C. A.; Shiku, H.; Matsue, T.; Klenerman, D.; Korchev, Y. E. Multifunctional Nanoprobes for Nanoscale Chemical Imaging and Localized Chemical Delivery at Surfaces and Interfaces. *Angew. Chemie Int. Ed.* **2011**, *50* (41), 9638–9642.

(125) Piper, J. D.; Li, C.; Lo, C. J.; Berry, R.; Korchev, Y.; Ying, L.; Klenerman, D. Characterization and Application of Controllable Local Chemical Changes Produced by Reagent Delivery from a Nanopipet. *J. Am. Chem. Soc.* **2008**, *130* (31), 10386–10393.

(126) Lohrengel, M. M.; Moehring, A.; Pilaski, M. Capillary-Based Droplet Cells: Limits and New Aspects. *Electrochim. Acta* **2001**, *47* (1), 137–141.

(127) Gregoire, J. M.; Xiang, C.; Liu, X.; Marcin, M.; Jin, J. Scanning Droplet Cell for High Throughput Electrochemical and Photoelectrochemical Measurements. *Rev. Sci. Instrum.* **2013**, *84* (2), 1–7.

(128) Williams, C. G.; Edwards, M. A.; Colley, A. L.; Macpherson, J. V.; Unwin, P. R. Scanning Micropipet Contact Method for High-Resolution Imaging of Electrode Surface Redox Activity. *Anal. Chem.* **2009**, *81* (7), 2486–2495.

(129) Ebejer, N.; Schnippering, M.; Colburn, A. W.; Edwards, M. A.; Unwin, P. R. Localized High Resolution Electrochemistry and Multifunctional Imaging: Scanning Electrochemical Cell Microscopy. *Anal. Chem.* **2010**, *82* (22), 9141–

9145.

(130) Li, Y.; Ning, X.; Ma, Q.; Qin, D.; Lu, X. Recent Advances in Electrochemistry by Scanning Electrochemical Microscopy. *TrAC - Trends Anal. Chem.* **2016**, *80*, 242–254.

(131) Unwin, P. R.; Güell, A. G.; Zhang, G. Nanoscale Electrochemistry of Sp2 Carbon Materials: From Graphite and Graphene to Carbon Nanotubes. *Acc. Chem. Res.* **2016**, *49* (9), 2041–2048.

(132) Bentley, C. L.; Kang, M.; Unwin, P. R. Scanning Electrochemical Cell Microscopy: New Perspectives on Electrode Processes in Action. *Curr. Opin. Electrochem.* **2017**, *6* (1), 23–30.

(133) Ebejer, N.; Güell, A. G.; Lai, S. C. S.; McKelvey, K.; Snowden, M. E.; Unwin, P. R. Scanning Electrochemical Cell Microscopy: A Versatile Technique for Nanoscale Electrochemistry and Functional Imaging. *Annu. Rev. Anal. Chem.* **2013**, *6* (1), 329–351.

(134) Chen, C. H.; Jacobse, L.; McKelvey, K.; Lai, S. C. S.; Koper, M. T. M.; Unwin, P. R. Voltammetric Scanning Electrochemical Cell Microscopy: Dynamic Imaging of Hydrazine Electro-Oxidation on Platinum Electrodes. *Anal. Chem.* **2015**, *87* (11), 5782–5789.

(135) Momotenko, D.; Byers, J. C.; McKelvey, K.; Kang, M.; Unwin, P. R. High-Speed Electrochemical Imaging. *ACS Nano* **2015**, *9* (9), 8942–8952.

(136) Patel, A. N.; Collignon, M. G.; OConnell, M. A.; Hung, W. O. Y.; McKelvey, K.; MacPherson, J. V.; Unwin, P. R. A New View of Electrochemistry at Highly Oriented Pyrolytic Graphite. *J. Am. Chem. Soc.* **2012**, *134* (49), 20117–20130.

(137) Zhang, G.; Kirkman, P. M.; Patel, A. N.; Cuharuc, A. S.; McKelvey, K.; Unwin, P. R. Molecular Functionalization of Graphite Surfaces: Basal Plane versus Step Edge Electrochemical Activity. *J. Am. Chem. Soc.* **2014**, *136* (32), 11444–11451.

(138) Güell, A. G.; Cuharuc, A. S.; Kim, Y. R.; Zhang, G.; Tan, S. Y.; Ebejer, N.; Unwin, P. R. Redox-Dependent Spatially Resolved Electrochemistry at Graphene and Graphite Step Edges. *ACS Nano* **2015**, *9* (4), 3558–3571.

(139) Güell, A. G.; Ebejer, N.; Snowden, M. E.; MacPherson, J. V.; Unwin, P. R.

Structural Correlations in Heterogeneous Electron Transfer at Monolayer and Multilayer Graphene Electrodes. *J. Am. Chem. Soc.* **2012**, *134* (17), 7258–7261.

(140) Zhang, G.; Güell, A. G.; Kirkman, P. M.; Lazenby, R. A.; Miller, T. S.; Unwin, P. R. Versatile Polymer-Free Graphene Transfer Method and Applications. *ACS Appl. Mater. Interfaces* **2016**, *8* (12), 8008–8016.

(141) Kumatani, A.; Miura, C.; Kuramochi, H.; Ohto, T.; Wakisaka, M.; Nagata, Y.; Ida, H.; Takahashi, Y.; Hu, K.; Jeong, S.; Fujita, J. ichi; Matsue, T.; Ito, Y. Chemical Dopants on Edge of Holey Graphene Accelerate Electrochemical Hydrogen Evolution Reaction. *Adv. Sci.* **2019**, *6* (10).

(142) Güell, A. G.; Ebejer, N.; Snowden, M. E.; McKelvey, K.; Macpherson, J. V.; Unwin, P. R. Quantitative Nanoscale Visualization of Heterogeneous Electron Transfer Rates in 2D Carbon Nanotube Networks. *Proc. Natl. Acad. Sci. U. S. A.* **2012**, *109* (29), 11487–11492.

(143) Nadappuram, P. B.; McKelvey, K.; Byers, J. C.; Güell, A. G.; Colburn, A. W.; Lazenby, R. A.; Unwin, P. R. Quad-Barrel Multifunctional Electrochemical and Ion Conductance Probe for Voltammetric Analysis and Imaging. *Anal. Chem.* **2015**, *87* (7), 3566–3573.

(144) Byers, J. C.; Güell, A. G.; Unwin, P. R. Nanoscale Electrocatalysis: Visualizing Oxygen Reduction at Pristine, Kinked, and Oxidized Sites on Individual Carbon Nanotubes. *J. Am. Chem. Soc.* **2014**, *136* (32), 11252–11255.

(145) Bentley, C. L.; Kang, M.; Unwin, P. R. Nanoscale Structure Dynamics within Electrocatalytic Materials. *J. Am. Chem. Soc.* **2017**, *139* (46), 16813–16821.

(146) Tarnev, T.; Aiyappa, H. B.; Botz, A.; Erichsen, T.; Ernst, A.; Andronescu, C.; Schuhmann, W. Scanning Electrochemical Cell Microscopy Investigation of Single ZIF-Derived Nanocomposite Particles as Electrocatalysts for Oxygen Evolution in Alkaline Media. *Angew. Chemie Int. Ed.* **2019**, *58* (40), 14265–14269.

(147) Ustarroz, J.; Ornelas, I. M.; Zhang, G.; Perry, D.; Kang, M.; Bentley, C. L.; Walker, M.; Unwin, P. R. Mobility and Poisoning of Mass-Selected Platinum Nanoclusters during the Oxygen Reduction Reaction. *ACS Catal.* **2018**, *8* (8),

6775–6790.

(148) Liu, D. Q.; Tao, B.; Ruan, H. C.; Bentley, C. L.; Unwin, P. R. Metal Support Effects in Electrocatalysis at Hexagonal Boron Nitride. *Chem. Commun.* **2019**, *55* (5), 628–631.

(149) Takahashi, Y.; Kobayashi, Y.; Wang, Z.; Ito, Y.; Ota, M.; Ida, H.; Kumatani, A.; Miyazawa, K.; Fujita, T.; Shiku, H.; Korchev, Y. E.; Miyata, Y.; Fukuma, T.; Chen, M.; Matsue, T. High-Resolution Electrochemical Mapping of the Hydrogen Evolution Reaction on Transition-Metal Dichalcogenide Nanosheets. *Angew. Chemie Int. Ed.* **2020**, *59* (9), 3601–3608.

(150) Yule, L. C.; Daviddi, E.; West, G.; Bentley, C. L.; Unwin, P. R. Surface Microstructural Controls on Electrochemical Hydrogen Absorption at Polycrystalline Palladium. *J. Electroanal. Chem.* **2020**, *872* (1), 114047.

(151) Mariano, R. G.; McKelvey, K.; White, H. S.; Kanan, M. W. Selective Increase in CO2 Electroreduction Activity at Grain-Boundary Surface Terminations. *Science* **2017**, *358*, 1187–1192.

(152) Bentley, C. L.; Andronescu, C.; Smialkowski, M.; Kang, M.; Tarnev, T.; Marler, B.; Unwin, P. R.; Apfel, U. P.; Schuhmann, W. Local Surface Structure and Composition Control the Hydrogen Evolution Reaction on Iron Nickel Sulfides. *Angew. Chemie Int. Ed.* **2018**, *57* (15), 4093–4097.

(153) Bentley, C. L.; Kang, M.; Maddar, F. M.; Li, F.; Walker, M.; Zhang, J.; Unwin, P. R. Electrochemical Maps and Movies of the Hydrogen Evolution Reaction on Natural Crystals of Molybdenite (MoS_2): Basal: Vs. Edge Plane Activity. *Chem. Sci.* **2017**, *8* (9), 6583–6593.

(154) Takahashi, Y.; Kumatani, A.; Munakata, H.; Inomata, H.; Ito, K.; Ino, K.; Shiku, H.; Unwin, P. R.; Korchev, Y. E.; Kanamura, K.; Matsue, T. Nanoscale Visualization of Redox Activity at Lithium-Ion Battery Cathodes. *Nat. Commun.* **2014**, *5*, 1–7.

(155) Ventosa, E.; Schuhmann, W. Scanning Electrochemical Microscopy of Li-Ion Batteries. *Phys. Chem. Chem. Phys.* **2015**, *17* (43), 28441–28450.

(156) Snowden, M. E.; Dayeh, M.; Payne, N. A.; Gervais, S.; Mauzeroll, J.;

Schougaard, S. B. Measurement on Isolated Lithium Iron Phosphate Particles Reveals Heterogeneity in Material Properties Distribution. *J. Power Sources* **2016**, *325*, 682–689.

(157) Sharel, P. E.; Kang, M.; Wilson, P.; Meng, L.; Perry, D.; Basile, A.; Unwin, P. R. High Resolution Visualization of the Redox Activity of Li_2O_2 in Non-Aqueous Media: Conformal Layer: Vs. Toroid Structure. *Chem. Commun.* **2018**, *54* (24), 3053–3056.

(158) Izquierdo, J.; Knittel, P.; Kranz, C. Scanning Electrochemical Microscopy: An Analytical Perspective. *Anal. Bioanal. Chem.* **2018**, *410* (2), 307–324.

(159) Zoski, C. G. Nanoscale Scanning Electrochemical Microscopy: Emerging Advances in Applications and Theory. *Curr. Opin. Electrochem.* **2017**, *1* (1), 46–52.

(160) Wang, X.; Han, L.; Xin, H.; Mirkin, M. V. TEM-Assisted Fabrication of Sub-10 Nm Scanning Electrochemical Microscopy Tips. *Anal. Chem.* **2019**, *91* (24), 15355–15359.

(161) Rodgers, P. J.; Amemiya, S.; Wang, Y.; Mirkin, M. V. Nanopipet Voltammetry of Common Ions across the Liquid-Liquid Interface. Theory and Limitations in Kinetic Analysis of Nanoelectrode Voltammograms. *Anal. Chem.* **2010**, *82* (1), 84–90.

(162) Page, A.; Perry, D.; Unwin, P. R. Multifunctional Scanning Ion Conductance Microscopy. *Proc. R. Soc. A Math. Phys. Eng. Sci.* **2017**, *473* (2200).

(163) Rodolfa, K. T.; Bruckbauer, A.; Zhou, D.; Schevchuk, A. I.; Korchev, Y. E.; Klenerman, D. Nanoscale Pipetting for Controlled Chemistry in Small Arrayed Water Droplets Using a Double-Barrel Pipet. *Nano Lett.* **2006**, *6* (2), 252–257.

(164) Thatenhorst, D.; Rheinlaender, J.; Schäffer, T. E.; Dietzel, I. D.; Happel, P. Effect of Sample Slope on Image Formation in Scanning Ion Conductance Microscopy. *Anal. Chem.* **2014**, *86* (19), 9838–9845.

(165) Cheng, X.; Pan, J.; Zhao, Y.; Liao, M.; Peng, H. Gel Polymer Electrolytes for Electrochemical Energy Storage. *Adv. Energy Mater.* **2018**, *8* (7), 1–16.

(166) Di Noto, V.; Lavina, S.; Giffin, G. A.; Negro, E.; Scrosati, B. Polymer

Electrolytes: Present, Past and Future. *Electrochim. Acta* **2011**, *57* (1), 4–13.

(167) Chaudoy, V.; Tran Van, F.; Deschamps, M.; Ghamouss, F. Ionic Liquids in a Poly Ethylene Oxide Cross-Linked Gel Polymer as an Electrolyte for Electrical Double Layer Capacitor. *J. Power Sources* **2017**, *342*, 872–878.

(168) Wang, J. A.; Lu, Y. T.; Lin, S. C.; Wang, Y. S.; Ma, C. C. M.; Hu, C. C. Designing a Novel Polymer Electrolyte for Improving the Electrode/Electrolyte Interface in Flexible All-Solid-State Electrical Double-Layer Capacitors. *ACS Appl. Mater. Interfaces* **2018**, *10* (21), 17871–17882.

(169) Soonmin, H.; Shanmugam, M.; Mordiya, M.; Markna, J. H. Review on Dye-Sensitized Solar Cells Based on Polymer Electrolytes. *Int. J. Eng. Technol.* **2018**, *7* (4), 3001–3006.

(170) FENTON; E., D. Complexes of Alkali Metal Ions with Poly (Ethylene Oxide). *Polymer (Guildf).* **1973**, *14*, 589.

(171) Kim, J. K.; Scheers, J.; Ahn, J. H.; Johansson, P.; Matic, A.; Jacobsson, P. Nano-Fibrous Polymer Films for Organic Rechargeable Batteries. *J. Mater. Chem. A* **2013**, *1* (7), 2426–2430.

(172) Bae, J.; Li, Y.; Zhang, J.; Zhou, X.; Zhao, F.; Shi, Y.; Goodenough, J. B.; Yu, G. A 3D Nanostructured Hydrogel-Framework-Derived High-Performance Composite Polymer Lithium-Ion Electrolyte. *Angew. Chemie Int. Ed.* **2018**, *57* (8), 2096–2100.

(173) Suga, T.; Ohshiro, H.; Ugita, S.; Oyaizu, K.; Nishide, H. Emerging N-Type Redox-Active Radical Polymer for a Totally Organic Polymer-Based Rechargeable Battery. *Adv. Mater.* **2009**, *21* (16), 1627–1630.

(174) Zhang, H.; Li, C.; Piszcz, M.; Coya, E.; Rojo, T.; Rodriguez-Martinez, L. M.; Armand, M.; Zhou, Z. Single Lithium-Ion Conducting Solid Polymer Electrolytes: Advances and Perspectives. *Chem. Soc. Rev.* **2017**, *46* (3), 797–815.

(175) Zhao, Q.; Whittaker, A. K.; Zhao, X. S. Polymer Electrode Materials for Sodium-Ion Batteries. *Materials (Basel).* **2018**, *11* (12).

(176) Sood, R.; Cavaliere, S.; Jones, D. J.; Rozière, J. Electrospun Nanofibre Composite Polymer Electrolyte Fuel Cell and Electrolysis Membranes. *Nano*

Energy **2016**, *26*, 729–745.

(177) Peng, H.; Li, Q.; Hu, M.; Xiao, L.; Lu, J.; Zhuang, L. Alkaline Polymer Electrolyte Fuel Cells Stably Working at 80 °C. *J. Power Sources* **2018**, *390*, 165–167.

(178) Heck, J. D.; Vaz, W. S.; Koylu, U. O.; Leu, M. C. Decoupling Pressure and Distribution Effects of Flow Fields on Polymer Electrolyte Fuel Cell System Performance. *Sustain. Energy Technol. Assessments* **2019**, *36*, 100551.

(179) Goodwin, Z. A. H.; Kornyshev, A. A. Theory of Polymer-Electrolyte-Composite Electroactuator Sensors with Flat or Volume-Filling Electrodes. *Soft Matter* **2018**, *14* (39), 7996–8005.

(180) Jin, M. L.; Park, S.; Kim, J.-S.; Kwon, S. H.; Zhang, S.; Yoo, M. S.; Jang, S.; Koh, H.-J.; Cho, S.-Y.; Kim, S. Y.; Ahn, C. W.; Cho, K.; Lee, S. G.; Kim, D. H.; Jung, H.-T. Sensors: An Ultrastable Ionic Chemiresistor Skin with an Intrinsically Stretchable Polymer Electrolyte. *Adv. Mater.* **2018**, *30* (20), 1870140.

(181) Yu, H. A.; Lee, J.; Lewis, S. W.; Silvester, D. S. Detection of 2,4,6-Trinitrotoluene Using a Miniaturized, Disposable Electrochemical Sensor with an Ionic Liquid Gel-Polymer Electrolyte Film. *Anal. Chem.* **2017**, *89* (8), 4729–4736.

(182) Huang, Y.; Zhong, M.; Shi, F.; Liu, X.; Tang, Z.; Wang, Y.; Huang, Y.; Hou, H.; Xie, X.; Zhi, C. An Intrinsically Stretchable and Compressible Supercapacitor Containing a Polyacrylamide Hydrogel Electrolyte. *Angew. Chemie Int. Ed.* **2017**, *56* (31), 9141–9145.

(183) Zhong, X.; Tang, J.; Cao, L.; Kong, W.; Sun, Z.; Cheng, H.; Lu, Z.; Pan, H.; Xu, B. Cross-Linking of Polymer and Ionic Liquid as High-Performance Gel Electrolyte for Flexible Solid-State Supercapacitors. *Electrochim. Acta* **2017**, *244*, 112–118.

(184) Eren, E. Improved Performance and Stability of Solid State Electrochromic Devices with Eco-Friendly Chitosan-Based Electrolytes. *Solid State Ionics* **2019**, *334*, 152–159.

(185) Chang, T. H.; Lu, H. C.; Lee, M. H.; Kao, S. Y.; Ho, K. C. Multi-Color Electrochromic Devices Based on Phenyl and Heptyl Viologens Immobilized with UV-Cured Polymer Electrolyte. *Sol. Energy Mater. Sol. Cells* **2018**, *177*, 75–81.

(186) Prasad, S.; Durairaj, D.; AlSalhi, M. S.; Theerthagiri, J.; Arunachalam, P.; Durai, G. Fabrication of Cost-Effective Dye-Sensitized Solar Cells Using Sheet-like CoS_2 Films and Phthaloylchitosan-Based Gel-Polymer Electrolyte. *Energies* **2018**, *11* (2).

(187) Bandara, T. M. W. J.; DeSilva, L. A.; Ratnasekera, J. L.; Hettiarachchi, K. H.; Wijerathna, A. P.; Thakurdesai, M.; Preston, J.; Albinsson, I.; Mellander, B. E. High Efficiency Dye-Sensitized Solar Cell Based on a Novel Gel Polymer Electrolyte Containing RbI and Tetrahexylammonium Iodide (Hex4NI) Salts and Multi-Layered Photoelectrodes of TiO_2 Nanoparticles. *Renew. Sustain. Energy Rev.* **2019**, *103*, 282–290.

(188) Choudhury, N. A.; Sampath, S.; Shukla, A. K. Hydrogel-Polymer Electrolytes for Electrochemical Capacitors: An Overview. *Energy Environ. Sci.* **2009**, *2* (1), 55–67.

(189) Sun, B.; Xu, C.; Mindemark, J.; Gustafsson, T.; Edström, K.; Brandell, D. At the Polymer Electrolyte Interfaces: The Role of the Polymer Host in Interphase Layer Formation in Li-Batteries. *J. Mater. Chem. A* **2015**, *3* (26), 13994–14000.

(190) Chen, W.; Zhu, C.; Guo, L.; Yan, M. Y.; Wu, L.; Zhu, B.; Qi, C.; Liu, S.; Zhang, H.; Peng, Y. A Novel Ionically Crosslinked Gel Polymer Electrolyte as an Ion Transport Layer for High-Performance Electrochromic Devices. *J. Mater. Chem. C* **2019**, *7* (13), 3744–3750.

(191) Armand M, Chabagno JM, D. M. P. Solid Electrolytes. In *Second International Meeting on Solid Electrolytes*; 1978.

(192) Dias, F. B.; Plomp, L.; Veldhuis, J. B. J. Trends in Polymer Electrolytes for Secondary Lithium Batteries. *J. Power Sources* **2000**, *88* (2), 169–191.

(193) Matsumura, S.; Hlil, A. R.; Lepiller, C.; Gaudet, J.; Guay, D.; Shi, Z.; Holdcroft, S.; Hay, A. S. Stability and Utility of Pyridyl Disulfide Functionality in RAFT

and Conventional Radical Polymerizations. *J. Polym. Sci. Part A Polym. Chem.* **2008**, *46*, 7207–7224.

(194) Stephan, A. M. Review on Gel Polymer Electrolytes for Lithium Batteries. *Eur. Polym. J.* **2006**, *42* (1), 21–42.

(195) Hamaya, T.; Inoue, S.; Qiao, J.; Okada, T. Novel Proton-Conducting Polymer Electrolyte Membranes Based on PVA/PAMPS/PEG400 Blend. *J. Power Sources* **2006**, *156* (2), 311–314.

(196) Yang, J. M.; Fan, C. S.; Wang, N. C.; Chang, Y. H. Evaluation of Membrane Preparation Method on the Performance of Alkaline Polymer Electrolyte: Comparison between Poly(Vinyl Alcohol)/Chitosan Blended Membrane and Poly(Vinyl Alcohol)/Chitosan Electrospun Nanofiber Composite Membranes. *Electrochim. Acta* **2018**, *266*, 332–340.

(197) Nair, J. R.; Gerbaldi, C.; Meligrana, G.; Bongiovanni, R.; Bodoardo, S.; Penazzi, N.; P.Reale; Gentili, V. UV-Cured Methacrylic Membranes as Novel Gel-Polymer Electrolyte for Li-Ion Batteries. *J. Power Sources* **2008**, *178* (2), 751–757.

(198) Vijayakumar, V.; Anothumakkool, B.; Torris, A. T.; Nair, S. B.; Badiger, M. V.; Kurungot, S. An All-Solid-State-Supercapacitor Possessing a Non-Aqueous Gel Polymer Electrolyte Prepared Using a UV-Assisted: In Situ Polymerization Strategy. *J. Mater. Chem. A* **2017**, *5* (18), 8461–8476.

(199) Bella, F.; Ozzello, E. D.; Bianco, S.; Bongiovanni, R. Photo-Polymerization of Acrylic/Methacrylic Gel-Polymer Electrolyte Membranes for Dye-Sensitized Solar Cells. *Chem. Eng. J.* **2013**, *225*, 873–879.

(200) Rhodes, C. P.; Long, J. W.; Doescher, M. S.; Dening, B. M.; Rolison, D. R. Charge Insertion into Hybrid Nanoarchitectures: Mesoporous Manganese Oxide Coated with Ultrathin Poly(Phenylene Oxide). *J. Non. Cryst. Solids* **2004**, *350*, 73–79.

(201) Rhodes, C. P.; Long, J. W.; Doescher, M. S.; Fontanella, J. J.; Rolison, D. R. Nanoscale Polymer Electrolytes: Ultrathin Electrodeposited Poly(Phenylene Oxide) with Solid-State Ionic Conductivity. *J. Phys. Chem. B* **2004**, *108* (35),

13079–13087.

(202) Rhodes, C. P.; Long, J. W.; Rolison, D. R. Direct Electrodeposition of Nanoscale Solid Polymer Electrolytes via Electropolymerization of Sulfonated Phenols. *Electrochem. Solid-State Lett.* **2005**, *8* (11), 579–584.

(203) Kyeremateng, N. A.; Dumur, F.; Knauth, P.; Pecquenard, B.; Djenizian, T. Electropolymerization of Copolymer Electrolyte into Titania Nanotube Electrodes for High-Performance 3D Microbatteries. *Electrochem. commun.* **2011**, *13* (8), 894–897.

(204) Plylahan, N.; Kyeremateng, N. A.; Eyraud, M.; Dumur, F.; Martinez, H.; Santinacci, L.; Knauth, P.; Djenizian, T. Highly Conformal Electrodeposition of Copolymer Electrolytes into Titania Nanotubes for 3D Li-Ion Batteries. *Nanoscale Res. Lett.* **2012**, *7*, 2–7.

(205) Kyeremateng, N. A.; Dumur, F.; Knauth, P.; Pecquenard, B.; Djenizian, T. Electrodeposited Copolymer Electrolyte into Nanostructured Titania Electrodes for 3D Li-Ion Microbatteries. *Comptes Rendus Chim.* **2013**, *16* (1), 80–88.

(206) Salian, G. D.; Lebouin, C.; Galeyeva, A.; Kurbatov, A. P.; Djenizian, T. Electrodeposition of Polymer Electrolyte into Porous $LiNi_{0.5}Mn_{1.5}O_4$ for High Performance All-Solid-State Microbatteries. *Front. Chem.* **2019**, *7*, 1–8.

(207) Salian, G. D.; Lebouin, C.; Demoulin, A.; Lepihin, M. S.; Maria, S.; Galeyeva, A. K.; Kurbatov, A. P.; Djenizian, T. Electrodeposition of Polymer Electrolyte in Nanostructured Electrodes for Enhanced Electrochemical Performance of Thin-Film Li-Ion Microbatteries. *J. Power Sources* **2017**, *340*, 242–246.

(208) Jiang, M.; Zhu, J.; Chen, C.; Lu, Y.; Ge, Y.; Zhang, X. Poly(Vinyl Alcohol) Borate Gel Polymer Electrolytes Prepared by Electrodeposition and Their Application in Electrochemical Supercapacitors. *ACS Appl. Mater. Interfaces* **2016**, *8* (5), 3473–3481.

(209) Hu, D.; Peng, C.; Chen, G. Z. Electrodeposition of Nonconducting Polymers: Roles of Carbon Nanotubes in the Process and Products. *ACS Nano* **2010**, *4* (7), 4274–4282.

(210) Shan, C.; Yang, H.; Han, D.; Zhang, Q.; Ivaska, A.; Niu, L.

Graphene/AuNPs/Chitosan Nanocomposites Film for Glucose Biosensing. *Biosens. Bioelectron.* **2010**, *25* (5), 1070–1074.

(211) Luo, X. L.; Xu, J. J.; Du, Y.; Chen, H. Y. A Glucose Biosensor Based on Chitosan-Glucose Oxidase-Gold Nanoparticles Biocomposite Formed by One-Step Electrodeposition. *Anal. Biochem.* **2004**, *334* (2), 284–289.

(212) Sakthivel, R.; Palanisamy, S.; Chen, S. M.; Ramaraj, S.; Velusamy, V.; Yi-Fan, P.; Hall, J. M.; Ramaraj, S. K. A Robust Nitrobenzene Electrochemical Sensor Based on Chitin Hydrogel Entrapped Graphite Composite. *J. Taiwan Inst. Chem. Eng.* **2017**, *80*, 663–668.

(213) Gray, K. M.; Liba, B. D.; Wang, Y.; Cheng, Y.; Rubloff, G. W.; Bentley, W. E.; Montembault, A.; Royaud, I.; David, L.; Payne, G. F. Electrodeposition of a Biopolymeric Hydrogel: Potential for One-Step Protein Electroaddressing. *Biomacromolecules* **2012**, *13* (4), 1181–1189.

(214) Zangmeister, R. A.; Park, J. J.; Rubloff, G. W.; Tarlov, M. J. Electrochemical Study of Chitosan Films Deposited from Solution at Reducing Potentials. *Electrochim. Acta* **2006**, *51* (25), 5324–5333.

(215) Zhang, Z.; Cheng, X.; Yao, Y.; Luo, J.; Tang, Q.; Wu, H.; Lin, S.; Han, C.; Wei, Q.; Chen, L. Electrophoretic Deposition of Chitosan/Gelatin Coatings with Controlled Porous Surface Topography to Enhance Initial Osteoblast Adhesive Responses. *J. Mater. Chem. B* **2016**, *4* (47), 7584–7595.

(216) Avcu, E.; Baştan, F. E.; Abdullah, H. Z.; Rehman, M. A. U.; Avcu, Y. Y.; Boccaccini, A. R. Electrophoretic Deposition of Chitosan-Based Composite Coatings for Biomedical Applications: A Review. *Prog. Mater. Sci.* **2019**, *103*, 69–108.

(217) Márquez, A.; Jiménez-Jorquera, C.; Domínguez, C.; Muñoz-Berbel, X. Electrodepositable Alginate Membranes for Enzymatic Sensors: An Amperometric Glucose Biosensor for Whole Blood Analysis. *Biosens. Bioelectron.* **2017**, *97*, 136–142.

(218) Márquez-Maqueda, A.; Ríos-Gallardo, J. M.; Vigués, N.; Pujol, F.; Díaz-González, M.; Mas, J.; Jiménez-Jorquera, C.; Domínguez, C.; Muñoz-Berbel, X.

Enzymatic Biosensors Based on Electrodeposited Alginate Hydrogels. *Procedia Eng.* **2016**, *168*, 622–625.

(219) Vigués, N.; Pujol-Vila, F.; Marquez-Maqueda, A.; Muñoz-Berbel, X.; Mas, J. Electro-Addressable Conductive Alginate Hydrogel for Bacterial Trapping and General Toxicity Determination. *Anal. Chim. Acta* **2018**, *1036*, 115–120.

(220) Ozawa, F.; Ino, K.; Arai, T.; Ramón-Azcón, J.; Takahashi, Y.; Shiku, H.; Matsue, T. Alginate Gel Microwell Arrays Using Electrodeposition for Three-Dimensional Cell Culture. *Lab Chip* **2013**, *13* (15), 3128–3135.

(221) Oyen, M. L. Mechanical Characterisation of Hydrogel Materials. *Int. Mater. Rev.* **2014**, *59* (1), 44–59.

(222) Hambly, B. P.; Sheppard, J. B.; Pendley, B. D.; Lindner, E. Voltammetric Determination of Diffusion Coefficients in Polymer Membranes: Guidelines to Minimize Errors. *Electroanalysis* **2018**, *30* (4), 681–689.

(223) Lin, D. C.; Horkay, F. Nanomechanics of Polymer Gels and Biological Tissues: A Critical Review of Analytical Approaches in the Hertzian Regime and Beyond. *Soft Matter* **2008**, *4* (4), 669–682.

(224) Dimitriadis, E. K.; Horkay, F.; Maresca, J.; Kachar, B.; Chadwick, R. S. Determination of Elastic Moduli of Thin Layers of Soft Material Using the Atomic Force Microscope. *Biophys. J.* **2002**, *82* (5), 2798–2810.

(225) Suriano, R.; Credi, C.; Levi, M.; Turri, S. AFM Nanoscale Indentation in Air of Polymeric and Hybrid Materials with Highly Different Stiffness. *Appl. Surf. Sci.* **2014**, *311*, 558–566.

(226) Nguyen, Q. D.; Chung, K. H. Effect of Tip Shape on Nanomechanical Properties Measurements Using AFM. *Ultramicroscopy* **2019**, *202*, 1–9.

(227) Orazem, Mark E., and B. T. *Electrochemical Impedance Spectroscopy.*; John Wiley & Sons, 2017.

(228) Lisdat, F.; Schäfer, D. The Use of Electrochemical Impedance Spectroscopy for Biosensing. *Anal. Bioanal. Chem.* **2008**, *391* (5), 1555–1567.

(229) Rezaei Niya, S. M.; Hoorfar, M. Study of Proton Exchange Membrane Fuel Cells Using Electrochemical Impedance Spectroscopy Technique - A Review. *J.*

Power Sources **2013**, *240*, 281–293.

(230) Pauliukaite, R.; Ghica, M. E.; Fatibello-Filho, O.; Brett, C. M. A. Electrochemical Impedance Studies of Chitosan-Modified Electrodes for Application in Electrochemical Sensors and Biosensors. *Electrochim. Acta* **2010**, *55* (21), 6239–6247.

(231) Pajkossy, T.; Jurczakowski, R. Electrochemical Impedance Spectroscopy in Interfacial Studies. *Curr. Opin. Electrochem.* **2017**, *1* (1), 53–58.

(232) Randviir, E. P.; Banks, C. E. Electrochemical Impedance Spectroscopy - an Overview. *Anal. Methods* **2013**, *5*, 1098–1115.

(233) Csóka, B.; Nagy, G. Determination of Diffusion Coefficient in Gel and in Aqueous Solutions Using Scanning Electrochemical Microscopy. *J. Biochem. Biophys. Methods* **2004**, *61*, 57–67.

(234) Fan, F. R. F. Electrochemical Studies on Ion Transport in Gels with Scanning Electrochemical Microscopy. *J. Phys. Chem. B* **1998**, *102* (49), 9777–9782.

(235) Denuault, G.; Mirkin, M. V.; Bard, A. J. Direct Determination of Diffusion Coefficients by Chronoamperometry at Microdisk Electrodes. *J. Electroanal. Chem.* **1991**, *308* (1–2), 27–38.

(236) Bard, A. J.; Denuault, G.; Friesner, R. A.; Dornblaser, B. C.; Tuckerman, L. S. Scanning Electrochemical Microscopy: Theory and Application of the Transient (Chronoamperometric) SECM Response. *Anal. Chem.* **1991**, *63* (13), 1282–1288.

(237) Liu, L.; Toledano, R.; Danieli, T.; Zhang, J. Q.; Hu, J. M.; Mandler, D. Electrochemically Patterning Sol-Gel Structures on Conducting and Insulating Surfaces. *Chem. Commun.* **2011**, *47* (24), 6909–6911.

(238) Sarkar, S.; Mandler, D. Scanning Electrochemical Microscopy versus Scanning Ion Conductance Microscopy for Surface Patterning. *ChemElectroChem* **2017**, *4* (11), 2981–2988.

(239) Ornelas, I. M.; Unwin, P. R.; Bentley, C. L. High-Throughput Correlative Electrochemistry-Microscopy at a Transmission Electron Microscopy Grid Electrode. *Anal. Chem.* **2019**, *91* (23), 14854–14859.

(240) Martin, R. D.; Unwin, P. R. Theory and Experiment for the Substrate

Generation/Tip Collection Mode of the Scanning Electrochemical Microscope: Application as an Approach for Measuring the Diffusion Coefficient Ratio of a Redox Couple. *Anal. Chem.* **1998**, *70* (2), 276–284.

(241) Koley, G.; Spencer, M. G. Surface Potential Measurements on GaN and AlGaN/GaN Heterostructures by Scanning Kelvin Probe Microscopy. *J. Appl. Phys.* **2001**, *90* (1), 337–344.

(242) Rojas, G. A.; Wu, Y.; Haugstad, G.; Frisbie, C. D. Measuring the Thickness and Potential Profiles of the Space-Charge Layer at Organic/Organic Interfaces under Illumination and in the Dark by Scanning Kelvin Probe Microscopy. *ACS Appl. Mater. Interfaces* **2016**, *8* (9), 5772–5776.

(243) Bhushan, B.; Goldade, A. V. Measurements and Analysis of Surface Potential Change during Wear of Single-Crystal Silicon (100) at Ultralow Loads Using Kelvin Probe Microscopy. *Appl. Surf. Sci.* **2000**, *157* (4), 373–381.

(244) Nonnenmacher, M.; O'Boyle, M. P.; Wickramasinghe, H. K. Kelvin Probe Force Microscopy. *Appl. Phys. Lett.* **1991**, *58* (25), 2921–2923.

(245) Glatzel, T.; Sadewasser, S.; Lux-Steiner, M. C. Amplitude or Frequency Modulation-Detection in Kelvin Probe Force Microscopy. *Appl. Surf. Sci.* **2003**, *210*, 84–89.

(246) Sadewasser, S.; Leendertz, C.; Streicher, F.; Lux-Steiner, M. C. The Influence of Surface Topography on Kelvin Probe Force Microscopy. *Nanotechnology* **2009**, *20* (50), 505503.

(247) Melitz, W.; Shen, J.; Kummel, A. C.; Lee, S. Kelvin Probe Force Microscopy and Its Application. *Surf. Sci. Rep.* **2011**, *66* (1), 1–27.

(248) Akid, R.; Garma, M. Scanning Vibrating Reference Electrode Technique: A Calibration Study to Evaluate the Optimum Operating Parameters for Maximum Signal Detection of Point Source Activity. *Electrochim. Acta* **2004**, *49* (17–18), 2871–2879.

(249) Xu, H.; Liu, Y.; Chen, W.; Du, R. G.; Lin, C. J. Corrosion Behavior of Reinforcing Steel in Simulated Concrete Pore Solutions: A Scanning Micro-Reference Electrode Study. *Electrochim. Acta* **2009**, *54* (16), 4067–4072.

(250) Kinlen, P. J.; Menon, V.; Ding, Y. A Mechanistic Investigation of Polyaniline Corrosion Protection Using the Scanning Reference Electrode Technique. *J. Electrochem. Soc.* **1999**, *146* (10), 3690–3695.

(251) Clausmeyer, J.; Henig, J.; Schuhmann, W.; Plumeré, N. Scanning Droplet Cell for Chemoselective Patterning through Local Electroactivation of Protected Quinone Monolayers. *ChemPhysChem* **2014**, *15* (1), 151–156.

(252) Jóźwiak, T.; Filipkowska, U.; Szymczyk, P.; Rodziewicz, J.; Mielcarek, A. Effect of Ionic and Covalent Crosslinking Agents on Properties of Chitosan Beads and Sorption Effectiveness of Reactive Black 5 Dye. *React. Funct. Polym.* **2017**, *114*, 58–74.

(253) Etinus, S. E. Ç. PH-Sensitive Chitosan Films for Baker's Yeast Immobilization. Applied Biochemistry and Biotechnology. *Appl. Biochem. Biotechnol.* **2002**, *101* (1), 239–249.

(254) Hu, Y.; Zhao, X.; Vlassak, J. J.; Suo, Z. Using Indentation to Characterize the Poroelasticity of Gels. *Appl. Phys. Lett.* **2010**, *96* (12).

(255) Barnes, E. O.; Fernández-La-Villa, A.; Pozo-Ayuso, D. F.; Castaño-Alvarez, M.; Lewis, G. E. M.; Dale, S. E. C.; Marken, F.; Compton, R. G. Interdigitated Ring Electrodes: Theory and Experiment. *J. Electroanal. Chem.* **2013**, *709*, 57–64.

(256) Liu, L.; Hu, J. M.; Zhang, J. Q.; Cao, C. N. Improving the Formation and Protective Properties of Silane Films by the Combined Use of Electrodeposition and Nanoparticles Incorporation. *Electrochim. Acta* **2006**, *52* (2), 538–545.

(257) Hu, J. M.; Liu, L.; Zhang, J. Q.; Cao, C. N. Electrodeposition of Silane Films on Aluminum Alloys for Corrosion Protection. *Prog. Org. Coatings* **2007**, *58* (4), 265–271.

(258) Liu, L.; Hu, J. M.; Zhang, J. Q.; Cao, C. N. Comment on Electrodeposited Silicate Films: Importance of Supporting Electrolyte. *Anal. Chem.* **2009**, *81* (8), 3199–3200.

(259) Mika Sillanpää, M. S. *Electrochemcial Water Treatment Methods: Fundamentals, Methods and Full Scale Applications*; Butterworth-Heinemann, 2017.

(260) Chang, B.-Y.; Park, S.-M. Electrochemical Impedance Spectroscopy of Composite Adhesive Joints. *Annu. Rev. Anal. Chem. (Palo Alto. Calif).* **2010**, *3* (6), 207–229.

(261) Bard, A. J.; Faulkner, L. R. *Fundamentals and Applications: Electrochemical Methods.*; Wiley: New York, 2001.

(262) Turyan, I.; Khatwani, N.; Sosic, Z.; Jayawickreme, S.; Mandler, D. A Novel Approach for Oxidation Analysis of Therapeutic Proteins. *Anal. Biochem.* **2016**, *494*, 108–113.

(263) Rusinek, C. A.; Bange, A.; Papautsky, I.; Heineman, W. R. Cloud Point Extraction for Electroanalysis: Anodic Stripping Voltammetry of Cadmium. *Anal. Chem.* **2015**, *87* (12), 6133–6140.

(264) Brainina, K. Z.; Malakhova, N. A.; Stojko, N. Y. Stripping Voltammetry in Environmental and Food Analysis. *Fresenius. J. Anal. Chem.* **2000**, *368* (4), 307–325.

(265) Svishchev, I. M.; Carvajal-Ortiz, R. A.; Choudhry, K. I.; Guzonas, D. A. Corrosion Behavior of Stainless Steel 316 in Sub- and Supercritical Aqueous Environments: Effect of LiOH Additions. *Corros. Sci.* **2013**, *72*, 20–25.

(266) Solakidou, M.; Giannakas, A.; Georgiou, Y.; Boukos, N.; Louloudi, M.; Deligiannakis, Y. Efficient Photocatalytic Water-Splitting Performance by Ternary CdS/Pt-N-TiO_2 and CdS/Pt-N,F-TiO_2: Interplay between CdS Photo Corrosion and TiO2-Dopping. *Appl. Catal. B Environ.* **2019**, *254*, 194–205.

(267) Nie, M.; Neodo, S.; Wharton, J. A.; Cranny, A.; Harris, N. R.; Wood, R. J. K.; Stokes, K. R. Electrochemical Detection of Cupric Ions with Boron-Doped Diamond Electrode for Marine Corrosion Monitoring. *Electrochim. Acta* **2016**, *202*, 345–356.

(268) Cranny, A.; Harris, N. R.; Nie, M.; Wharton, J. A.; Wood, R. J. K.; Stokes, K. R. Sensors for Corrosion Detection: Measurement of Copper Ions in 3.5% Sodium Chloride Using Screen-Printed Platinum Electrodes. *IEEE Sens. J.* **2012**, *12* (6), 2091–2099.

(269) López-Delgado, A. A Laboratory Study of the Effect of Acetic Acid Vapor on

Atmospheric Copper Corrosion. *J. Electrochem. Soc.* **1998**, *145* (12), 4140.

(270) Matisson, E.; Bockris, J. O. M. Galvanostatic Studies of the Kinetics of Deposition and Dissolution in the Copper + Copper Sulphate System. *Trans. Faraday Soc.* **1959**, *55*, 1586–1601.

(271) Ller, A. W. C. Mechanism of Copper in Acidic Sulfate Solutions. *Electrochim. Acta* **1993**, *38* (14), 2121–2127.

(272) Cordeiro, G. G. O.; Barcia, O. E.; Mattos, O. R. Copper Electrodissolution Mechanism in a 1M Sulphate Medium. *Electrochim. Acta* **1993**, *38* (2–3), 319–324.

(273) Khodari, M.; Abou-Krisha, M. M.; Assaf, F. H.; El-Cheikh, F. M.; Hussien, A. A. Stripping Voltammetric and Conductance Measurements on Corrosion and Inhibition of Copper in Nitric Acid. *Mater. Chem. Phys.* **2001**, *71* (3), 279–290.

(274) Jönsson, M.; Persson, D.; Thierry, D. Corrosion Product Formation during NaCl Induced Atmospheric Corrosion of Magnesium Alloy AZ91D. *Corros. Sci.* **2007**, *49* (3), 1540–1558.

(275) Živojinović, D. Z.; Rajaković, L. V. Application and Validation of Ion Chromatography for the Analysis of Power Plants Water: Analysis of Corrosive Anions in Conditioned Water-Steam Cycles. *Desalination* **2011**, *275* (1–3), 17–25.

(276) Carlini, R.; Carnasciali, M. M.; Soggia, F.; Campodonico, S.; Zanicchi, G. ICP-AES and MicroRaman Corrosion Behaviour Investigation on Zn4Sb3 and Al, Ag Doped Phases in Sodium Chloride Solution. *J. Alloys Compd.* **2014**, *588*, 361–365.

(277) Kalcioglu, Z. I.; Mahmoodian, R.; Hu, Y.; Suo, Z.; Van Vliet, K. J. From Macro- to Microscale Poroelastic Characterization of Polymeric Hydrogels via Indentation. *Soft Matter* **2012**, *8* (12), 3393–3398.

(278) Vandamme, M.; Ulm, F. J. Viscoelastic Solutions for Conical Indentation. *Int. J. Solids Struct.* **2006**, *43* (10), 3142–3165.

(279) Song, D.; Ma, A. Bin; Jiang, J.; Lin, P.; Yang, D.; Fan, J. Corrosion Behavior of Equal-Channel-Angular-Pressed Pure Magnesium in NaCl Aqueous Solution.

Corros. Sci. **2010**, *52* (2), 481–490.

Appendix I Optimization of the gel probe preparation

In above potentiometric and amperometric measurements, the gel probe was prepared by cathodic electrodeposition of chitosan on the micro-disk electrodes. Before applying the gel probe in the local electrochemical analysis, the optimization of cathodic deposition of chitosan was studied. In addition, the probe fabrication by means of anodic deposition of chitosan also have been explored.

A1.1 Cathodic deposition

At the beginning of the solutions preparation, the concentrated HCl (37%) was used to dissolve chitosan. Due to the evaporation of concentrated HCl, 1M HCl was used instead for increasing the stability of solution. Two solutions were prepared by dissolving 0.8 wt.% chitosan in 1:1 (vol. ratio) glycerol/deionized water. The pH of solutions was around 4.5. For comparing the effect of pH, one solution was adjusted to 5.5 by 1M NaOH. Deposition was achieved in a three-electrode system, with a Pt planar electrode (diameter of 2 mm) as the work electrode, chlorinated Ag wire as the quasi-reference electrode (QRE) and a Pt wire as the counter electrode.

After adjusting the pH, the deposition curves are very smooth and reproducible. Besides, more positive potentials could be used in the deposition. This proves that the hydrogen revolution is decreased obviously by increasing the pH (**Figure A1A**). However, there are still bubbles in gel, which influence the mechanical properties of hydrogel. After adding 0.125 M $NaNO_3$ into solution, the bubbles in chitosan hydrogel were significantly decreased, and the films are smoother and more compacted (**Figure A1B**). This illustrates that nitride reduction could inhibit the water analysis to decline the bubbles in chitosan film.

Microelectrodes are used in SGECM for mapping the topography and electrochemical properties of sample surface. Hence, it’s important to explore the chitosan deposition on microelectrode. **Figure A2A** shows the deposition curves of chitosan on Pt microelectrode without NaNO$_3$. It's shown that the curves are smooth yet the reproducibility is not good. Perhaps due to the absence of nitrite, deposition is only assisted by the electrolysis of water, in which the hydrogen evolution is not easy to control. However, there is no bubble in gel probe and the shapes of gel probes are approximate (**Figure A2B**). This because the diameter of microelectrode is comparable with bubble, which is difficult to stay in microgel. Hence, for the microelectrode, bubbles could be avoided by controlling the size of gel. After adding 0.125M NaNO$_3$, the deposition curves are more reproducible (Fig. 1-2 B). This illustrates that NaNO$_3$ could increase the reproducibility of chitosan deposition on microelectrode.

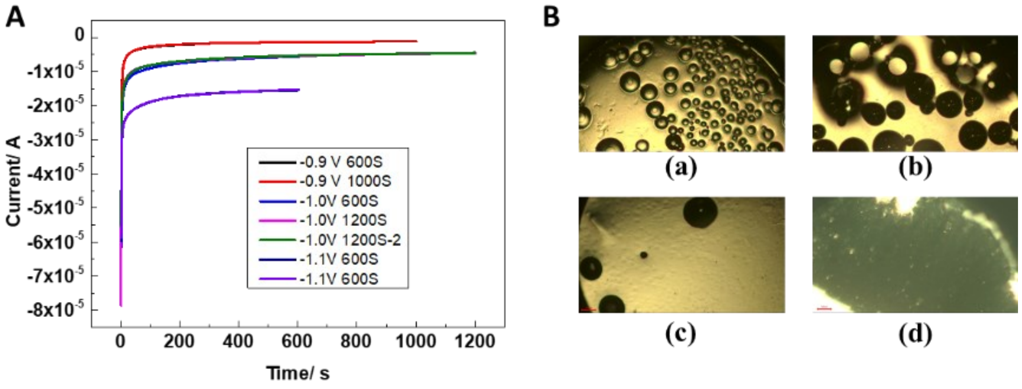

Figure A1 Deposition curves of chitosan on Pt planar electrode (pH 5.5) (A). Images of chitosan film on Pt planar electrode (B), (a) without NaNO$_3$, -0.9 V, 1000s; (b) without NaNO$_3$, -1.0V, 1200s;(c) addition of 0.125M NaNO$_3$, -0.9 V 1200s; (d) addition of 0.125M NaNO$_3$, -1.0 V 1200s.

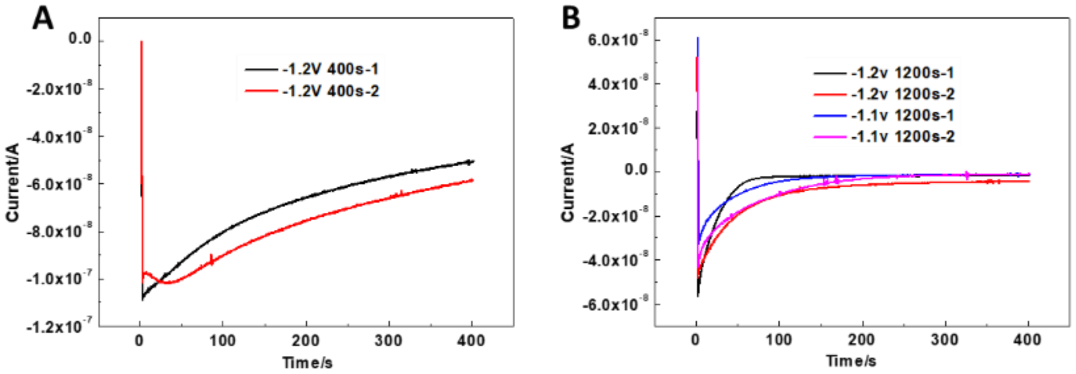

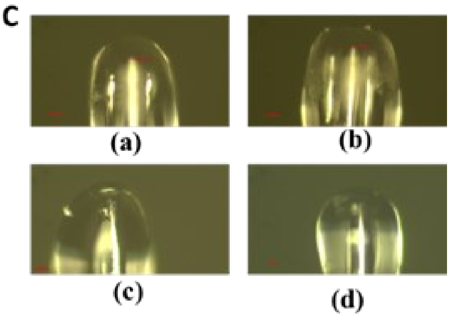

Figure A2 Deposition curves of chitosan on Pt microelectrode without $NaNO_3$ (A). Deposition curves of chitosan on Pt microelectrode with 0.125M $NaNO_3$ (B). Images of chitosan on Pt microelectrode (C). (a, b) without $NaNO_3$, -1.2 V 400s; (c, d) addition of 0.125M $NaNO_3$, -1.2 V 1200s.

A1.2 Anodic deposition

It's notable that the cathodic hydrogel is stable under neutral and basic conditions, yet it is unstable and dissolves under acidic conditions. It's reported that chitosan could be deposited on the copper electrode through the coordinated electrodeposition method, and the obtained hydrogel is smooth, transparent, and homogeneous, as well as it has stability under acidic conditions and enough strength to be readily peeled from the electrode. Here, we tried to deposit chitosan on Ag surface to fabricate ideal hydrogel probe.

Deposition solution was prepared by dissolving the chitosan powder (1.0 % w/v) in acetic acid (0.25% v/v), and adjusting the pH to 5.5. Chitosan was deposited on Ag microelectrode (25 μm) at the potential of 1 V (vs. Ag/AgCl QRE) for 300s. The deposition curve is shown in **FigureA3A** and the image of probe is shown in **FigureA3B(a)**. The probe was immersed into water for 5 minutes (**FigureA3B(b)**), the gel was swelling instead of dissolving in water. This proves the stability of anodic deposited gel. The fresh gel was immersed in 0.125% glutaraldehyde for 5 minutes, it's seen that it remains the same shape (**FigureA3B(c)**), which means the gel was cross-linked by glutaraldehyde. After washing the gel in 0.1M $NaNO_3$ solution (**FigureA3B(d)**), the gel is approach on Pt plate by current feedback in SGECM. The CV was scanned between Ag probe and Pt plate to test the stability of coordinate bond between Ag and chitosan. Form **FigureA3C**, it’s shown that no obvious reduction peak of Ag-chitosan, but there is an oxidation peak at potential of 0.5 V (E_{Ag} vs. E_{Pt}). The reason is still unknown, so more experiments should be designed to study the properties of anodic deposited chitosan.

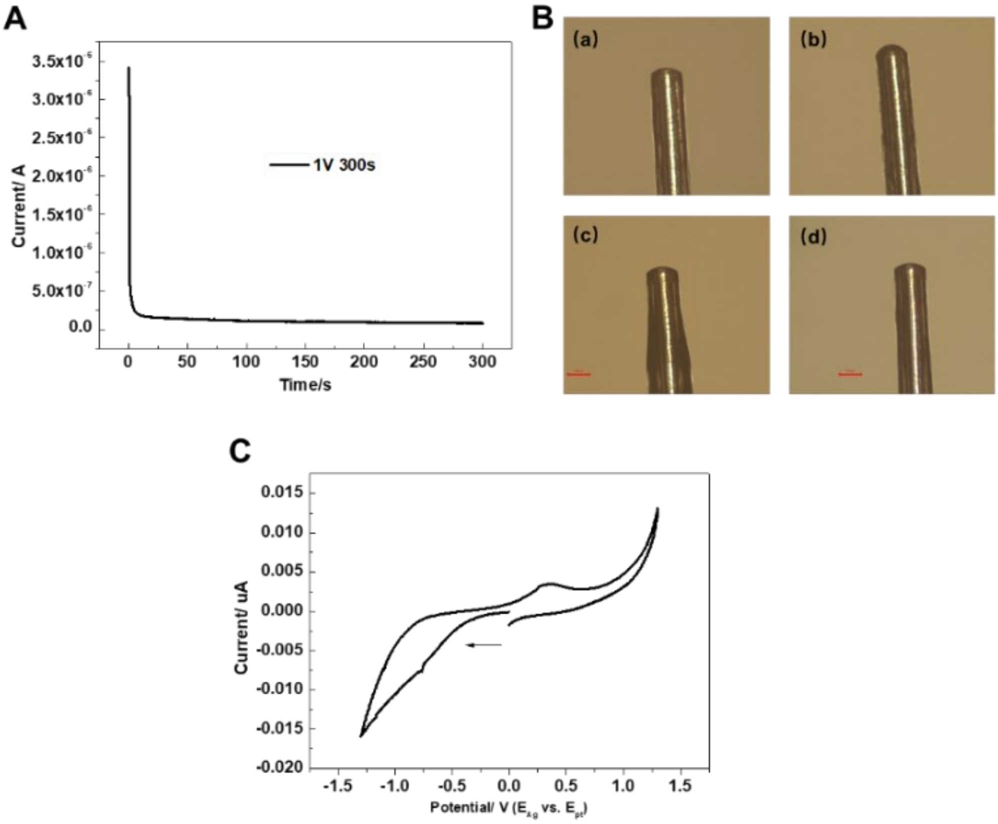

Figure A3 chitosan anodic deposition curve on Ag microelectrode(A). Images of chitosan (B) after deposition (a), after immersing in water (b), after cross-linking by glutaraldehyde (c), after washing in 0.1M $NaNO_3$ solution (d). CV test after approaching Gel Ag probe on Pt plate (C).

A1.3 Conclusion

In this appendix, the optimization of chitosan deposition was studied. For cathodic deposition, pH, nitrate and electrode size are key factors. Results show that hydrogen evolution was decreased by adjusting the pH of chitosan deposition solution to 5.5, deposition curve is smoother and almost reproducible for both macro- and micro-electrodes. There is no bubble in gel deposited on microelectrode. Reproducibility of deposition on microelectrode could be increased by addition of $NaNO_3$. Anodic deposition is a promising way to fabricated the chitosan probe. The chitosan is stable with changing the pH. But the electrochemical stability should to be investigated further.

Appendix II Fabrication of gel probe on the commercialized HEKA micro-disk electrodes

Figure A5A is the HEKA micro-disk electrode with active diameter of 25 µm and R_g of 2. Gel probe have been fabricated by deposition of chitosan on this commercial electrode. The solution was prepared by dissolving 0.8 % w/v chitosan, 0.1 M NaCl in glycerol and deionized water (1:1 in volume). The pH was adjusted to 5.5. Various parameters were applied to deposited the hydrogel. Before a new deposition, the probe was ultrasonicated in 0.1 M H_2SO_4 and alcohol solutions respectively to remove the gel. All the deposition curves are shown in **Figure A4.** It's seen that the current is higher at more negative potential. At –0.9 V, the curves are overlapped very well. This suggests the good reproducibility of the deposition. The images of the gel probe are shown in **Figure A5B - Figure A5H**. The hydrogel fabricated at –0.95 V is thicker than at –0.9 V because of more OH^- ions were generated at more negative potential. Even though the deposition curves at –0.95 V are not so reproducible in **Figure A4**. The images of probe in **Figure A5** are very similar. This also proves the reproducibility of the gel deposition.

The gel probe fabricated at –0.95 V for 350 s was approached to be in contact with the current feedback. The multiple approach curves are given in **Figure A6**. Since the fresh gel attaches the solvent on the surface, the initial approaching not stop at the same location in *z* axes. After few operations, the approach and retract curves are overlapped, showing the stable mechanical properties of the hydrogel.

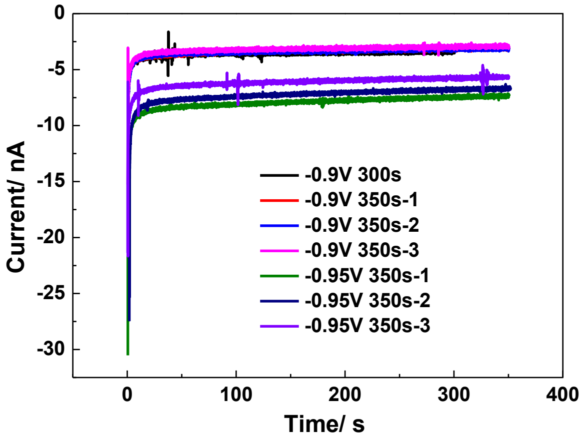

Figure A4 Chitosan deposition curves on the HEKA micro-disk electrode with diameter of 25 µm.

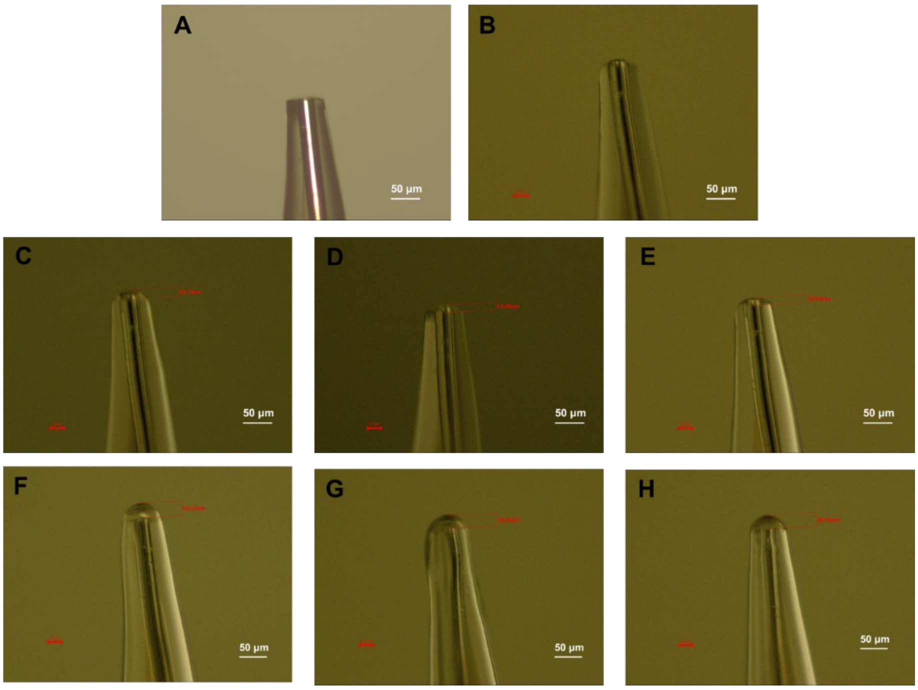

Figure A5 Images of gel probe fabricated by on the HEKA micro-disk electrode with diameter of 25 µm. Bare electrode (A); deposited at –0.9 V for 30 s (B); deposited at –0.9 V for 350 s (C, D, E); deposited at –0.95 V for 350 s (F, G, H).

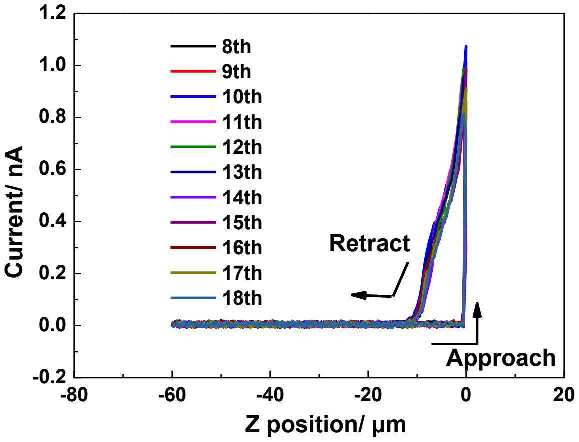

Figure A6 Multiple approach and retract curves of gel probe (diameter 25 µm) upon the Ag plate.

Based on the HEKA micro-disk electrode with diameter of 10 µm, the fabricated gel probe has smaller size and higher resolution. The deposition curves, probe images and the multiple approach and retract curves are also as shown in following figures. Similar with the 25 µm micro-disk electrode, gel probe could be easily fabricated reproducibly. Collaboration with HEKA, our technique shows attractive potential of commercialization.

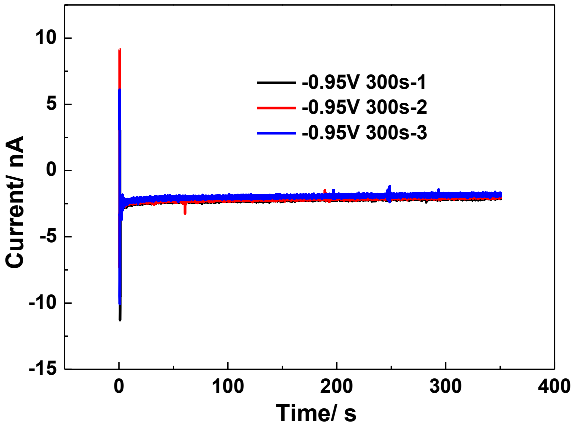

Figure A7 Chitosan deposition curves on the HEKA micro-disk electrode with diameter of 10 µm.

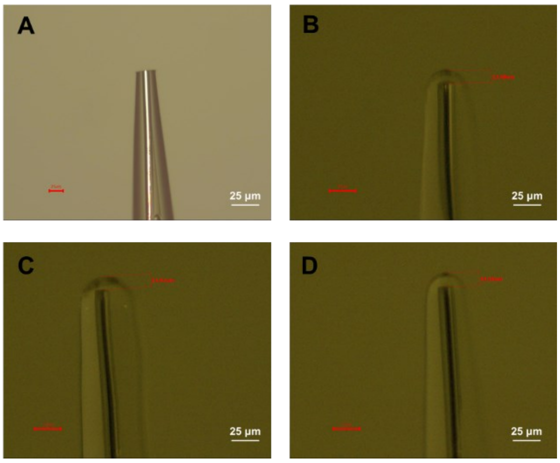

Figure A8 Images of gel probe fabricated by on the HEKA micro-disk electrode with diameter of 10 µm. Bare electrode (A); deposited at –0.95 V for 300 s (B, C, D).

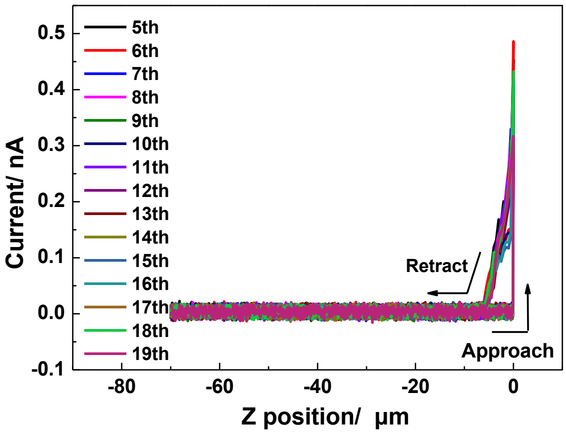

Figure A9 Multiple approach and retract curves of gel probe (diameter 10 µm) upon the Ag plate.

Appendix III Diffusion coefficient of $Ru(NH_3)_6Cl_3$ in gel deposited on planar electrode

The diffusion coefficient of $Ru(NH_3)_6Cl_3$ in chitosan hydrogel deposited on the planar electrode is analyzed by the Randles-Sevcik equation (**Equation 1.10**). It's known that the thickness of diffusion layer is from 10^{-3} to 10^{-2} cm, thus for achieving the semi-infinite diffusion in hydrogel on planar electrode, the thickness of gel is deposited over than 10^{-1}cm. After gel deposition (solution: 0.8 wt.% chitosan, 0.125M $NaNO_3$), chitosan was cross-linked by glutaraldehyde (0.2%) for 2 hour. For diffusion coefficient characterization, the gel was immersed into 0.1mM $Ru(NH_3)_6Cl_3$ solution. Form **Figure A10A**, it's seen that the concentration equilibrium of $Ru(NH_3)_6Cl_3$ in hydrogel and bulk solution is built after 10 minutes. After 20 minutes, CV was tested at scan rate of 0.01V/s, 0.05V/s, 0.1V/s, 0.15V/s, 0.2V/s, 0.25V/s respectively (**Figure A10B**). The reduction peak current is plotted as the function of square root of scan rate and the curve is fitted linearly, the result is given in **Figure A10B**. It's seen that the R-square is 0.99929, which suggests that the fitting matches very well with the data obtained from the experiment and the diffusion coefficient could be calculated by Randles-Sevcik equation correctly. Finally, the diffusion coefficient of $[Ru(NH_3)_6]^{3+}$ in cross-linked chitosan hydrogel is 4.996×10^{-6} cm^2/s.

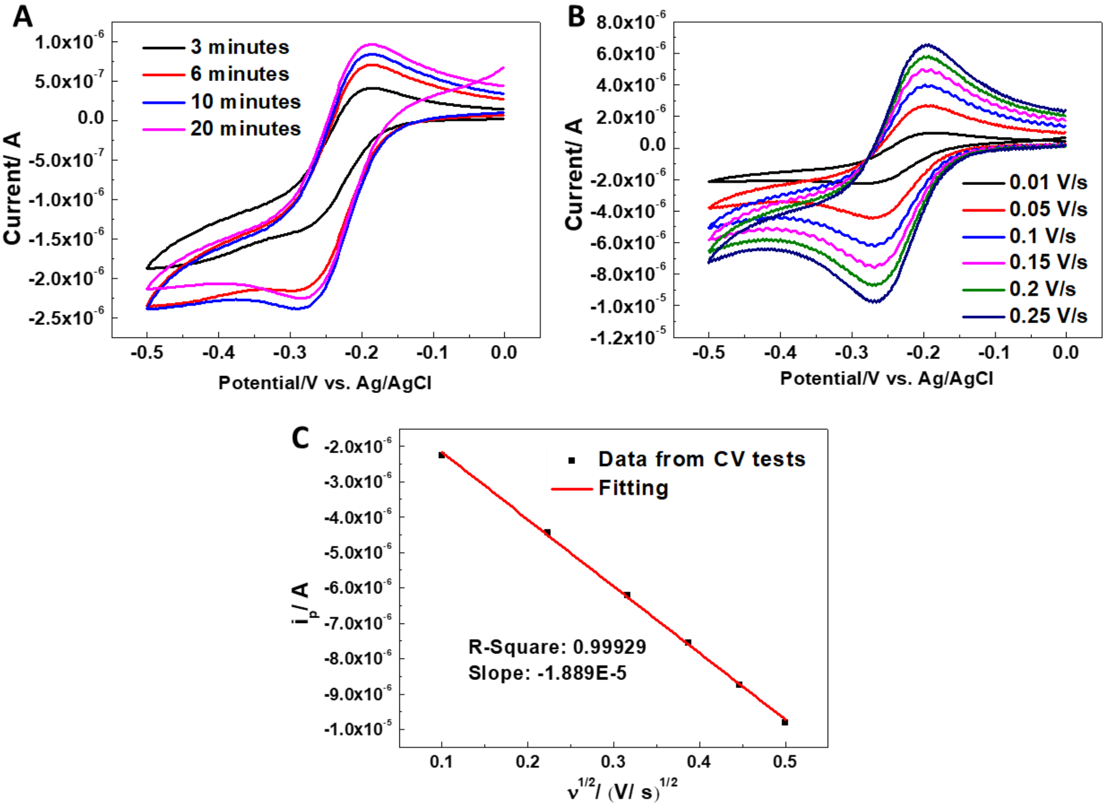

Figure A10 CV test of cross-linked hydrogel on planar electrode in 0.1mM $Ru(NH_3)_6Cl_3$ solution after different immersion time (scan rate:10mV/s)(A), CV test of cross-linked hydrogel in 0.1mM $Ru(NH_3)_6Cl_3$ solution at different scan rate (B), linear fitting of peak current in **Figure A10B** with scan rate (C).

Appendix IV Mathematic model 1 for the potentiometric analysis of Fe^{3+} droplets on Fe plate

Consider that the following two redox reactions occur on the Fe plate:

$Fe^{3+} + e \leftrightarrow Fe^{2+}$ (1)

$Fe^{2+} + 2e \leftrightarrow Fe$ (2)

The first reaction has rate constant k_1^0, and the second reaction has rate constant k_2^0. Following Butler-Volmer Equation, the corresponding current at a given potential can be expressed as:

$$I_1 = FAk_1^0\left\{[Fe^{3+}]_{surf}e^{-\frac{\alpha_1 F}{RT}(E_{Fe}-E_1^0)} - [Fe^{2+}]_{surf}e^{\frac{(1-\alpha_1)F}{RT}(E_{Fe}-E_1^0)}\right\} \quad (3)$$

$$I_2 = 2FAk_2^0\left\{[Fe^{2+}]_{surf}e^{-\frac{2\alpha_2 F}{RT}(E_{Fe}-E_2^0)} - e^{\frac{2(1-\alpha_2)F}{RT}(E_{Fe}-E_2^0)}\right\} \quad (4)$$

As the Fe plate is always at open circuit, $I_1 = -I_2$ should apply all the time, which makes it at a mixed potential that changes over time. Therefore,

$$k_1^0\left\{[Fe^{3+}]_{surf}e^{-\frac{\alpha_1 F}{RT}(E_{Fe}-E_1^0)} - [Fe^{2+}]_{surf}e^{\frac{(1-\alpha_1)F}{RT}(E_{Fe}-E_1^0)}\right\} =$$
$$-2k_2^0\left\{[Fe^{2+}]_{surf}e^{-\frac{2\alpha_2 F}{RT}(E_{Fe}-E_2^0)} - e^{\frac{2(1-\alpha_2)F}{RT}(E_{Fe}-E_2^0)}\right\} \quad (5)$$

In the beginning of the reaction, the concentration of Fe^{2+} should be low and the mixed potential E_{Fe} should be far from E_1^0 and E_2^0 (Assumption 1: $E_1^0 \gg E_{Fe} \gg E_2^0$), which is known as Tafel approximation. Thus,

$$k_1^0[Fe^{3+}]_{surf}e^{-\frac{\alpha_1 F}{RT}(E_{Fe}-E_1^0)} = 2k_2^0 e^{\frac{2(1-\alpha_2)F}{RT}(E_{Fe}-E_2^0)} \quad (6)$$

Consider the small volume of droplet, assume that the distribution of concentration in the droplet is uniform and neglect the effect of mass transport:

Assumption 2: $[Fe^{3+}]_{surf} = [Fe^{3+}]$, and $[Fe^{2+}]_{surf} = [Fe^{2+}]$

Another assumption that is frequently used in electrochemistry:

Assumption 3: $\alpha_1 = \alpha_2 = 0.5$

Then *Eq. 6* can be rewritten as,

$$k_1^0[Fe^{3+}]e^{-\frac{0.5F}{RT}(E_{Fe}-E_1^0)} = 2k_2^0 e^{\frac{F}{RT}(E_{Fe}-E_2^0)} \quad (7)$$

And the potential of Fe plate E_{Fe} can be solved as:

$$E_{Fe} = \frac{1}{3}E_1^0 + \frac{2}{3}E_2^0 + \frac{2RT}{3F} ln\frac{k_1^0[Fe^{3+}]}{2k_2^0} \quad (8)$$

Consider the reaction rate:

$$-\frac{d[Fe^{3+}]}{dt} = \frac{I_1}{FA} = k_1^0[Fe^{3+}]e^{-\frac{0.5F}{RT}(E_{Fe}-E_1^0)} \quad (9)$$

Substituting E_{Fe} by Eq. 8, then,

$$-\frac{d[Fe^{3+}]}{dt} = k_1^0[Fe^{3+}]e^{-\frac{0.5F}{RT}\left(-\frac{2}{3}E_1^0+\frac{2}{3}E_2^0+\frac{2RT}{3F}ln\frac{k_1^0[Fe^{3+}]}{2k_2^0}\right)} = (k_1^0[Fe^{3+}])^{\frac{2}{3}}(2k_2^0)^{\frac{1}{3}}e^{\frac{F}{3RT}(E_1^0-E_2^0)}$$

(10)

With the boundary condition $[Fe^{3+}] = [Fe^{3+}]_0$ at *t* = 0, the concentration of $[Fe^{3+}]$ as a function of time can be solved:

$$[Fe^{3+}]^{\frac{1}{3}} = [Fe^{3+}]_0^{\frac{1}{3}} - \frac{1}{3}(k_1^0)^{\frac{2}{3}}(2k_2^0)^{\frac{1}{3}}e^{\frac{F}{3RT}(E_1^0-E_2^0)}t \quad (11)$$

The concentration of $[Fe^{3+}]$ can also be derived from the potential measured on the integrated probe using Nernst Equation and the stoichiometry:

$$E_{measure} = E_1^0 - \frac{RT}{F} ln\frac{[Fe^{2+}]}{[Fe^{3+}]} \quad (12)$$

$$[Fe^{2+}] = \frac{3}{2}([Fe^{3+}]_0 - [Fe^{3+}]) + [Fe^{2+}]_0 \quad (13)$$

Then,

$$[Fe^{3+}] = \frac{\frac{3}{2}[Fe^{3+}]_0+[Fe^{2+}]_0}{\frac{3}{2}+e^{\frac{F}{RT}(E_1^0-E_{measure})}} \quad (14)$$

E_1^0 refers to the potential measured in 1:1 Fe^{3+}/Fe^{2+} solution. This calibrates the reference electrode.

Check with experimental data whether $\left(\frac{\frac{3}{2}[Fe^{3+}]_0+[Fe^{2+}]_0}{\frac{3}{2}+e^{\frac{F}{RT}(E_1^0-E_{measure})}}\right)^{\frac{1}{3}}$ has a linear relationship with *t*.

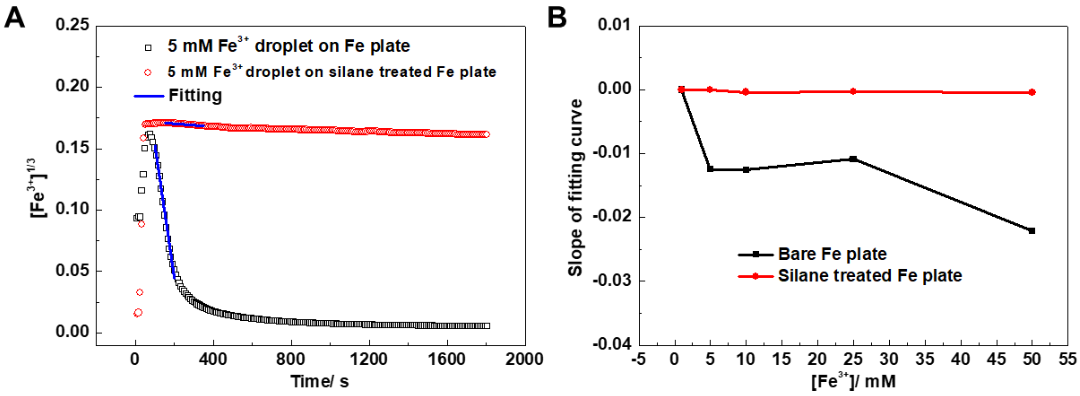

Figure A11 OCP fitting of 5 mM Fe^{3+} droplets on bare and silane treated Fe plates (A), slope of fitting curves of Fe^{3+} droplets with different concentration (1 mM, 5 mM, 10 mM, 25 mM, 50 mM) (B).

By plotting $[\mathbf{Fe^{3+}}]^{\frac{1}{3}}$ *vs. t* as shown in **Figure 11A**, one would expect a linear relationship in the beginning of the measurement. Nevertheless, the experimental results are not that ideal. Considering that the probe takes *ca.* 100 s to stabilize the potential measurement, assumption 1 $(E_1^0 \gg E_{Fe} \gg E_2^0)$ may not be available. Besides, the Assumption 2 ($[Fe^{3+}]_{surf} = [Fe^{3+}]$, and $[Fe^{2+}]_{surf} = [Fe^{2+}]$) is also not the real case, since the probe is not approached to be contact with the sample surface, so the concentration gradient of species in droplet is an important effect in potentiometric measurements.

Appendix V Mathematic model 2 for the potentiometric analysis of Fe^{3+} droplets on Fe plate

Derivation 1:

For the special case: $Fe + 2Fe^{3+} \underset{k_f}{\overset{k_b}{\leftrightarrows}} 3Fe^{2+}$
According to the reaction rate reaction,

$$-\frac{1}{2}\frac{d[\mathrm{Fe}^{3+}]}{dt} = \frac{1}{3}\frac{d[\mathrm{Fe}^{2+}]}{dt} = k_f A[\mathrm{Fe}^{3+}]^a - k_b A[\mathrm{Fe}^{2+}]^b$$

Assume the order of the reaction a and b are 1.

Stoichiometry:

$$[\mathrm{Fe}^{2+}] = \frac{3}{2}([\mathrm{Fe}^{3+}]_0 - [\mathrm{Fe}^{3+}])$$

$$-\frac{1}{2}\frac{d[\mathrm{Fe}^{3+}]}{dt} = k_f A[\mathrm{Fe}^{3+}] - \frac{3}{2}k_b A([\mathrm{Fe}^{3+}]_0 - [\mathrm{Fe}^{3+}])$$

$$\frac{d[\mathrm{Fe}^{3+}]}{dt} + 2k_f A[\mathrm{Fe}^{3+}] = 3k_b A([\mathrm{Fe}^{3+}]_0 - [\mathrm{Fe}^{3+}])$$

$$\frac{d[\mathrm{Fe}^{3+}]}{dt} + (2k_f + 3k_b)A[\mathrm{Fe}^{3+}] = 3k_b A[\mathrm{Fe}^{3+}]_0$$

Solve $[\mathrm{Fe}^{3+}]$ by integration:

$$[\mathrm{Fe}^{3+}] = e^{-A(2k_f+3k_b)t}[3k_b[\mathrm{Fe}^{3+}]_0 \frac{1}{2k_f + 3k_b} e^{A(2k_f+3k_b)t} + c]$$

When $t = 0,\ [\mathrm{Fe}^{3+}] = [\mathrm{Fe}^{3+}]_0$
Using this boundary condition:

$$[\mathrm{Fe}^{3+}]_0 = 3k_b[\mathrm{Fe}^{3+}]_0 \frac{1}{2k_f + 3k_b} + c$$

$$c = \frac{2k_f}{2k_f + 3k_b}[\mathrm{Fe}^{3+}]_0$$

So,

$$[\mathrm{Fe}^{3+}] = \frac{2k_f}{2k_f + 3k_b}[\mathrm{Fe}^{3+}]_0 e^{-A(2k_f+3k_b)t} + \frac{3k_b}{2k_f + 3k_b}[\mathrm{Fe}^{3+}]_0$$

$$\frac{[\mathrm{Fe}^{3+}]}{[\mathrm{Fe}^{3+}]_0} = \frac{2k_f}{2k_f + 3k_b} e^{-A(2k_f+3k_b)t} + \frac{3k_b}{2k_f + 3k_b}$$

From Nernst equation:

$$E = E^{\theta}{}_{Fe^{3+}/Fe^{2+}} - \frac{RT}{F} ln \frac{[Fe^{2+}]}{[Fe^{3+}]}$$

$$E = E^{\theta}{}_{Fe^{3+}/Fe^{2+}} - \frac{RT}{F} \ln \left[\frac{1}{[\mathrm{Fe}^{3+}]} \cdot \frac{3}{2} ([\mathrm{Fe}^{3+}]_0 - [\mathrm{Fe}^{3+}])\right]$$

$$E = E^{\theta}{}_{Fe^{3+}/Fe^{2+}} - \frac{RT}{F} \ln \left[\frac{3}{2}\left(\frac{[\mathrm{Fe}^{3+}]_0}{[\mathrm{Fe}^{3+}]} - 1\right)\right]$$

So,

$$E = E^{\theta}{}_{Fe^{3+}/Fe^{2+}} - \frac{RT}{F} \ln\frac{3}{2} - \frac{RT}{F} \ln \left[\frac{2k_f}{2k_f + 3k_b} e^{-A(2k_f+3k_b)t} + \frac{3k_b}{2k_f + 3k_b} - 1\right]$$

Derivation 2:

For the general case: $Ox + \mathrm{ne} \underset{k_f}{\overset{k_b}{\leftrightharpoons}} Red$
According to the reaction rate reaction,

$$-\frac{d[Ox]}{dt} = k_f A[Ox] - k_b A[Red]$$

Boundary condition 1: When $t = 0,\ [Ox] = [Ox]_0,\ [Red]_0 = 0.$
Stoichiometry:

$$[Red] = [Ox]_0 - [Ox]$$

$$-\frac{d[Ox]}{dt} = k_f A[Ox] - k_b A([Ox]_0 - [Ox])$$

$$-\frac{d[Ox]}{dt} = (k_f + k_b)A[Ox] - k_b A[Ox]_0$$

Solve $[Ox]$, similar with the case above:

$$[Ox] = \frac{k_f}{k_f + k_b}[Ox]_0 e^{-A(k_f+k_b)t} + \frac{k_b}{k_f + k_b}[Ox]_0$$

$$\frac{[Ox]}{[Ox]_0} = \frac{k_f}{k_f + k_b} e^{-(k_f+k_b)t} + \frac{k_b}{k_f + k_b}$$

From Nernst equation:

$$E = E^{\theta}{}_{Ox/Red} - \frac{RT}{F} ln \frac{[Red]}{[Ox]}$$

$$E = E^{\theta}{}_{Ox/Red} - \frac{RT}{F}\ln\,[\frac{[Ox]_0}{[Ox]} - 1]$$

$$E = E^{\theta}{}_{Ox/Red} - \frac{RT}{F}\ln\,[\frac{1}{\frac{k_f}{k_f + k_b}e^{-(k_f+k_b)t} + \frac{k_b}{k_f + k_b}} - 1]$$

Convergence:

$t \to 0, E \to +\infty$

$$t \to \infty, E \to E^{\theta}{}_{Ox/Red} - \frac{RT}{F}\ln\frac{k_f}{k_b}$$

Boundary condition 2: When $t = 0$, $[Ox] = [Ox]_0$, $[Red]_0 \neq 0$.

The stoichiometry changes to:

$[Red] = [Ox]_0 - [Ox] + [Red]_0$

So,

$$-\frac{d[Ox]}{dt} = k_f A[Ox] - k_b A([Ox]_0 - [Ox] + [Red]_0)$$

$$-\frac{d[Ox]}{dt} = \left(k_f + k_b\right)A[Ox] - k_b A([Ox]_0 + [Red]_0)$$

Solve $[Ox]$:

$$[Ox] = \frac{k_f[Ox]_0 - k_b[Red]_0}{k_f + k_b}e^{-A(k_f+k_b)t} + \frac{k_b}{k_f + k_b}([Ox]_0 + [Red]_0)$$

$$\frac{[Ox]}{[Ox]_0 + [Red]_0} = \frac{k_f[Ox]_0 - k_b[Red]_0}{k_f + k_b([Ox]_0 + [Red]_0)}e^{-A(k_f+k_b)t} + \frac{k_b}{k_f + k_b}$$

From Nernst equation:

$$E = E^{\theta}{}_{Ox/Red} - \frac{RT}{F}ln\frac{[Red]}{[Ox]}$$

$$E = E^{\theta}{}_{Ox/Red} - \frac{RT}{F}\ln\,[\frac{[Ox]_0 + [Red]_0}{[Ox]} - 1]$$

$$E = E^{\theta}{}_{Ox/Red} - \frac{RT}{F}\ln\,[\frac{1}{\frac{k_f[Ox]_0 - k_b[Red]_0}{k_f + k_b([Ox]_0 + [Red]_0)}e^{-A(k_f+k_b)t} + \frac{k_b}{k_f + k_b}} - 1]$$

Convergence:

$t \to 0$,

$$E \to E^{\theta}{}_{Ox/Red} - \frac{RT}{F}\ln\left[\frac{1}{\frac{k_f[Ox]_0 - k_b[Red]_0}{k_f + k_b([Ox]_0 + [Red]_0)} + \frac{k_b}{k_f + k_b}} - 1\right]$$

$$= E^{\theta}{}_{Ox/Red} - \frac{RT}{F}\ln\frac{[Red]_0}{[Ox]_0}$$

$t \to \infty$,

$$E \rightarrow E^{\theta}{}_{Ox/Red} - \frac{RT}{F}\ln\frac{k_f}{k_b}$$

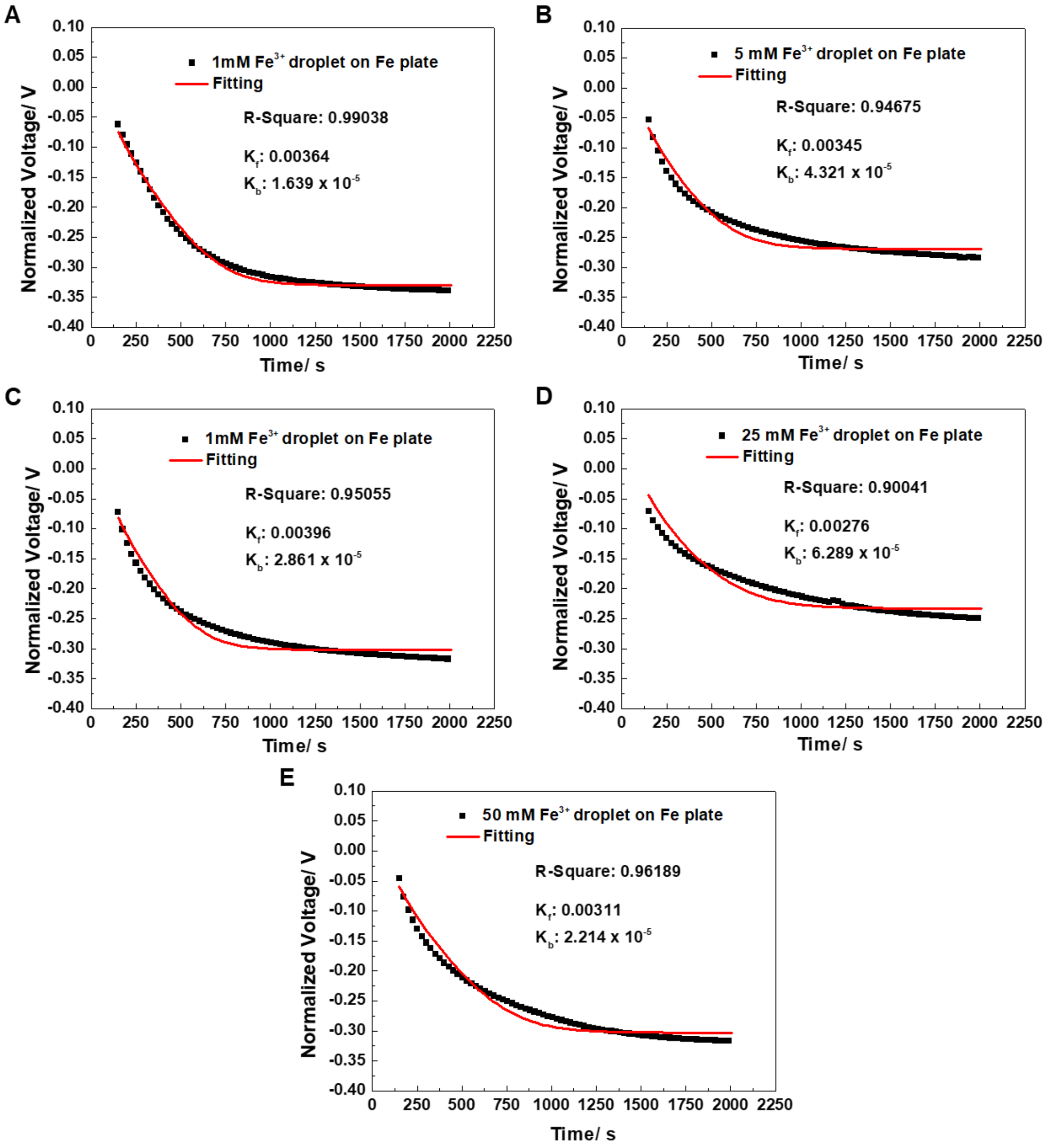

Figure A12 Data fitting of Fe^{3+} droplet on Fe plate (A): 1 mM Fe^{3+}, (B): 5 mM Fe^{3+}, (C): 10 mM Fe^{3+}, (D): 25 mM Fe^{3+}, (E): 50 mM Fe^{3+}.

This model treats the reaction as the simple chemical redox reaction. After combination of rate equation and Nernst equation, the kinetic rate constant K_f could be solved. **Figure A12** is the fitting results of the Fe^{3+} droplet on Fe plate based on the model 2. The R-square is acceptable but the kinetic rate constant K_f is not reasonable. In theory, the change of the K_f at different concentrations should be regular. But here is not this case. And the results obtained on saline treated Fe plate cannot be fitted by the model very well. Considering the corrosion is a heterogenous electrochemical reaction with the electron transfer between metal and the solutions, perhaps the kinetic rate could not be simplified as a single chemical reaction.